(NASA-CR-138750) ANODE POWER IN A QUASI-STEADY MPD THRUSTER Ph.D. Thesis (Princeton Univ.) 144 p HC $10.25 CSCL 20I

N74-28167

Unclas
G3/25 41921

JUL 1974
RECEIVED
NASA STI FACILITY
INPUT BRANCH

PRINCETON UNIVERSITY

DEPARTMENT OF
AEROSPACE AND MECHANICAL SCIENCES

Prepared for
National Aeronautics
and Space Administration
NASA Research Grant NGL 31-001-005

ANODE POWER IN A QUASI-STEADY MPD THRUSTER

A. J. Saber and R. G. Jahn

Report 1128*

Prepared by ______________________
A. J. Saber

Approved by R. G. Jahn
R. G. Jahn
Dean, School of Engineering

*This report is a reproduction in entirety of the Ph.D. dissertation of Mr. Aaron Jaan Saber. It is submitted to the sponsor and to the distribution list in this form both as a presentation of the technical material, and as an indication of the academic program supported by this Grant.

May 1974

School of Engineering and Applied Science
Department of Aerospace and Mechanical Sciences
Guggenheim Aerospace Propulsion Laboratories
PRINCETON UNIVERSITY
Princeton, New Jersey

ABSTRACT

Local anode heat flux in a quasi-steady MPD thruster is measured by thermocouples attached to the inside surface of a shell anode. Over a range of arc currents J from 5.5 to 44 kiloamperes and argon propellant mass flows $\dot{m}$ from 1 to 48 g/sec, with the ratio $J^2/\dot{m}$ held constant, the fraction of arc power deposited in the anode is found to decrease with increasing arc power. Specifically, this anode power fraction decreases from 50% at 200 kW arc power, to 10% at 20 MW. In an effort to account for this functional behavior, the current density, plasma potential, and electron temperature in the plasma adjacent to the anode are measured with probes, and the results are used in a theoretical anode heat flux model. The model asserts that energy exchange between electrons and heavy particles in the plasma near the anode occurs over distances greater than the anode sheath thickness. Consequently, a contribution from interelectrode potential augments anode fall voltage, electron temperature and work function contributions to the anode heat flux. Calculations of anode heat flux using the model agree with the direct measurements, and the decrease in anode power fraction at higher arc powers can be attributed to the smaller mean free paths in the interelectrode plasma.

TABLE OF CONTENTS

Page

CHAPTER 1 - THE ANODE POWER QUESTION

CHAPTER 2 - THE MPD ARCJET APPARATUS

CHAPTER 3 - ANODE HEAT FLUX AND POWER

CHAPTER 4 - ANODE HEAT FLUX MECHANISM

TABLE OF CONTENTS (Cont'd)

LIST OF ILLUSTRATIONS

Page

CHAPTER 1

CHAPTER 2

CHAPTER 3

LIST OF ILLUSTRATIONS (Cont'd)

CHAPTER 4 Page

CHAPTER 5

LIST OF SYMBOLS

A	area
A'	area
$\mathbb{B}$	magnetic induction field
B	magnitude of magnetic induction field
B_θ	azimuthal component of magnetic induction field
c	specific heat of anode material
c_p	specific heat at constant pressure
D	anode width
E_o	threshold energy for inelastic collisional event
E_1	energy where maximum inelastic cross section occurs
$\mathbb{E}$	electric field
E_ρ	radial component of electric field (cylindrical co-ordinates)
E_z	axial component of electric field (cylindrical co-ordinates)
$\hat{e}_\rho$	radial unit vector (cylindrical co-ordinates)
$\hat{e}_\theta$	azimuthal unit vector (cylindrical co-ordinates)
$\hat{e}_z$	axial unit vector (cylindrical co-ordinates)
e	charge on an electron $\left[e = -1.602\ (10^{-19})\ \text{Coulombs}\right]$
$\mathbf{H}(t)$	Heaviside function
h	Planck's constant $\left[h = 6.626(10^{-34})\ \text{Joule-sec}\right]$
h_e	electron enthalpy
h_g	convective heat transfer co-efficient
I	double probe current
I_e	electron current
I_i	ion current

LIST OF SYMBOLS (Cont'd)

$\hat{I}$	double probe saturation current extrapolated to current axis at zero potential
J	arc current
j	current density
j_a	local anode current density
$\hat{j}_a$	dimensionless local anode current density
k	Boltzmann's constant $\left[k = 1.38(10^{-23})\ \text{Joule}/^{o}\text{K}\right]$
k_p	thermal conductivity of plasma
k_t	thermal conductivity of anode material
L	streamline length
ℓ	local anode shell thickness
$\dot{m}$	injected propellant mass flow
m_a	neutral atom mass
m_e	electron mass $\left[9.109(10^{-31})\ \text{kg}\right]$
m_i	ion mass
m_j	j-particle mass
N_u	Nusselt number
n_a	neutral atom number density
n_e	electron number density
n_h	heavy particle number density
n_i	ion number density
P_A	anode power
Pr	Prandtl number
P_T	arc power
Q_e^E	electron energy exchange collision cross section
$Q_{eh}^{(\beta)}$	electron-heavy particle energy exchange collision cross section
$Q_{ea}^{E,ex}$	electron-atom excitation collision cross section
$Q_{ea}^{E,ion}$	electron-atom ionization collision cross section

LIST OF SYMBOLS (Cont'd)

$Q_{ei}^{E,ex}$	electron-ion excitation collision cross section
$Q_{ei}^{E,ion}$	electron-ion ionization collision cross section
$Q_{ei}^{E,p}$	electron-ion elastic energy exchange cross section by multiple momentum exchange collisions
Q_{ei}^{p}	Coulomb electron-ion momentum exchange collision cross section
q	heat flux
q_a	local anode heat flux
q_{conv}	convective anode heat flux
q_{radn}	ratiative anode heat flux
$q_{eh}^{(\beta)}$	maximum inelastic energy exchange cross section of type (β) between an electron and a heavy particle
R	dimensionless heat conduction parameter
R_e	Reynolds number
r	anode orifice radius
$\mathbf{r}$	position co-ordinate vector of electron
$\mathbf{r}_j$	position co-ordinate vector of j-particle
s	current streamline co-ordinate
s^*	dimensionless current streamline co-ordinate
T	discharge duration
T_e	electron temperature
T_i	ion temperature
t	time
t_f	time for all heat flux to the anode to cease
u	plasma streaming velocity magnitude
u'	plasma streaming velocity component normal to probe electrode axis
u_b	Bohm speed
u_e	electron velocity magnitude

LIST OF SYMBOLS (Cont'd)

V	arc voltage
V_a	anode fall voltage
V_c	cathode fall voltage
V_f	Langmuir probe floating potential
V_o	volume
V_p	plasma potential
V_s	potential difference between anode sheath edge and location s along a current streamline
$\mathbf{v}$	velocity
$\mathbf{v}_e$	electron velocity vector
$\mathbf{v}_h$	heavy particle velocity vector
$v_{th,e}$	electron thermal speed
$v_{th,e}$	j-particle thermal speed
x	co-ordinate along linearly rolled-out anode
y	co-ordinate of anode thickness
z	ion charge number
z_c	axis vector in cylindrical co-ordinate system
δ	ratio
ε	radiation
$\varepsilon_{\xi\xi}$	Bremsstrahlung
ε_o	permittivity of free space $[\varepsilon_o = 8.85(10^{-12})\text{Farad/m}]$
ζ_1	radial component of electron velocity vector
ζ_2	meridial component of electron velocity vector
ζ_3	azimuthal component of electron velocity vector

LIST OF SYMBOLS (Cont'd)

Φ	local temperature rise per unit heat flux inside anode shell
θ	temperature
θ_c	azimuth in cylindrical co-ordinate system
$\varkappa$	thermal diffusivity of anode material
Λ	plasma parameter
λ_s^E	electron energy exchange displacement
λ	magnitude of energy exchange displacement
λ^*	dimensionless magnitude of energy exchange displacement
λ_D	Debye length
λ_g	Larmor radius
μ	viscosity
μ_e	electron mobility
ν_{ea}^{β}	collision frequency for electron-neutral energy exchange of type (β)
ν_{ei}^{β}	collision frequency for electron-ion energy exchange of type (β)
ν_{ei}^{P}	collision frequency for electron-ion momentum exchange
ν_{eh}^{P}	collision frequency for electron-j-particle momentum exchange
ρ	density of anode material
ρ_c	radius in cylindrical co-ordinate system
ρ_P	plasma density

LIST OF SYMBOLS (Cont'd)

σ	Stefan-Boltzmann constant $[\sigma = 5.7(10^{-12})\ W/cm^2\text{-}{}^oK^4]$
τ_e^{ε}	energy exchange mean free time
φ	anode material work function
Ω	Hall parameter
ω_g	Larmor frequency

Subscripts

a	neutral particle
e	electron
g	Larmor
h	heavy particle
i	ion
j	any particle
P	plasma
t	anode
z	axial
ρ	radial
θ	azimuthal
0	threshold
1	location of maximum

Superscripts

E	energy
ex	excitation
ion	ionization
p	momentum
(β)	energy exchange event

CHAPTER 1
THE ANODE POWER QUESTION

1.1 Introduction

Electromagnetic thrusters accelerate ionized propellant by the interaction of an electric current driven through it with a magnetic field.(1) This class of electric propulsion promises a combination of high specific impulse (1000-5000 seconds) and thrust density (over 10^4 N/m^2) demanded by many deep space missions(2) that is unattainable with chemical propulsion,(3) electrothermal(4,8,9) or electrostatic thrusters.(5,6,7) In electromagnetic thrusters using current levels below 10^3 amp, an external magnetic field must be supplied to produce significant thrust;(10-13) at higher currents, the self-induced magnetic field is of sufficient magnitude that the external field may be avoided.(14-16) It is with this latter, self-field class of electromagnetic thruster that this study is concerned.

The particular type of electromagnetic thruster examined here is an outgrowth of earlier attempts to extend the operating range of thermal arcjets by increasing their power density. A typical thermal arcjet with a specific impulse of about 1000 seconds and a thrust of about 1 Newton has an arc power of about 30 kW. Attempts to improve specific impulse and thrust by increasing input power caused severe heat loading of the anode.(9)

Although the performance capabilities of the arcjet had been improved by the use of magnetic fields, the electrodes, especially the anode, were still being heated excessively.(16)

However, working with a conventional thermal arcjet with a central cathode and a coaxial anode, Ducati showed that drastically reducing the mass flow caused the establishment of a diffuse axisymmetric discharge.(17) In this mode, the arc current could be increased and the power range in the steady arcs enlarged by an order of magnitude. With arc currents in the kiloampere range, the induced magnetic fields were sufficiently large that external magnets were unnecessary. This thruster, the self-field MPD arc, shows the potential required for many advanced deep space missions.(18,19)

A schematic of such an MPD arc is shown in Fig. 1.1. The current, which flows from anode to cathode, has axial and radial components and produces an azimuthal magnetic field. The arc current passes through the injected propellant stream, ionizes the propellant and interacts with the induced magnetic field to accelerate propellant mass to provide thrust. The interaction of the radial component of arc current with the azimuthal magnetic field produces an axial acceleration ("blowing"), while interaction of the axial component of arc current with the magnetic field compresses the propellant to provide a reaction force on the cathode surface ("pumping"). In addition to these electromagnetic components of thrust, there may be some electrothermal contribution recovered in the expansion of the high-enthalpy propellant heated ohmically in the arc chamber.

The electromagnetic thrust in the MPD arc varies as the square of the arc current.(20,21) This suggests that the arc be operated at the highest possible current levels. However, steady high-current operation is limited by tolerable electrode heat transfer as well as by power supply capabilities. To relieve this difficulty, the arc may be operated in a pulsed "quasi-steady" mode.(22,23) In quasi-steady operation, electrical power is supplied to the thruster in pulses which are long enough that steady processes prevail during the discharge

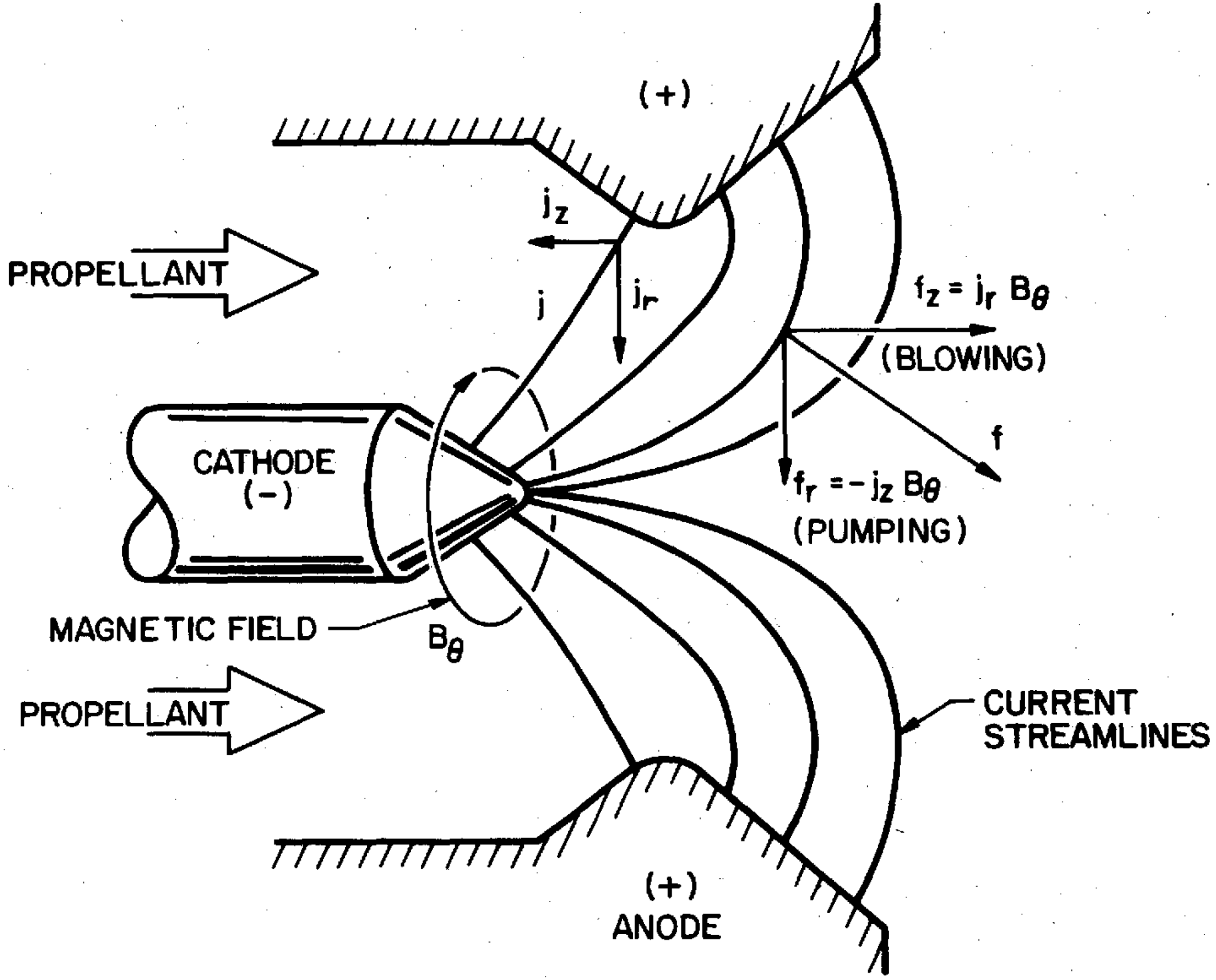

FIGURE I.1

AP25-5033

SELF - FIELD MPD ACCELERATOR

period, but short enough that the average energy deposited in the electrodes is tolerable. The quasi-steady operation also facilitates laboratory study of the MPD accelerator. It allows detailed study throughout the plasma using uncooled diagnostic probes.

The quasi-steady thruster used in this investigation has been extensively studied at Princeton. A discussion of its development is discussed by Jahn and Clark,(22,23) the performance described by Clark,(22) Cory(20) and Bruckner,(24) and the mechanisms involved investigated by Boyle and Jahn.(25) Examination of the cathode region was discussed by Turchi(26) and anode phenomena were first examined by Oberth.(27) The accelerator was designed to study the physics of MPD acceleration, but results apply to the development of the MPD arcjet as an electromagnetic thruster.

1.2 Anode Power

The efficiency of electromagnetic thruster operation at powers below one megawatt is dominated by anode losses, which may exceed 50% of the total arc power.(28-30) Because of this and the electrode heat transfer problem, considerable attention has been paid to the evaluation and understanding of anode power in these devices.

The anode power in steady thrusters is usually assessed from the temperature rise of a known mass flow rate of anode coolant.(31) In a variant of the technique, the anode power of a radiatively cooled 50 kW external field accelerator was estimated to be 20-40% of the arc power from the heat absorbed by the magnet housing coolant.(11) Another investigation used the temperature rise of the coolant of a segmented anode to estimate local anode heat flux in a sub-megawatt MPD arc.(32)

Existing theories of anode heating are based on energy balances over the anode sheath in a plasma free of magnetic field and in thermal equilibrium.(33,34) The results have been verified in high-pressure arcs operating with currents from 1 to 500 Amps and current densities from 1 to 500 A/cm with arc powers to 50 kW.(31,35,36) However, these theories, as well as those dealing with the flow of an initially unionized gas presumed to ionize over the anode,(37,38,39,40,41) do not strictly apply to relatively low pressure discharges. Nevertheless they have been used to infer the anode power in the MPD arc.

In earlier experiments in this laboratory, it was shown, from measurements of local plasma properties, that the anode power fraction in an MPD thruster decreases as arc power is increased.(27) This result, based on indirect measurements, suggests that a fractionally larger portion of the input power is available for the useful production of thrust. Consequently, detailed study of anode heat flux and anode power is warranted.

In the investigation reported here, local anode heat flux and power in the MPD arc are measured directly over an extended range of arc powers up to multi-megawatt levels, and a theory of anode power which is applicable to the MPD arc is introduced. The investigation is carried out on an apparatus described in Chapter 2, and the direct measurement of local anode heat flux is shown in Chapter 3. A study of the anode region of the discharge is presented in Chapter 4 and the mechanisms involved in anode heat flux are detailed. Chapter 4 also includes an explanation for a measured decrease of anode power fraction with increasing arc power observed in Chapter 3. The implications of the work to high current discharge devices, and the MPD arc in particular, are discussed in Chapter 5. The appendices which follow detail several of the arguments and calculations used.

CHAPTER 2
THE MPD ARCJET APPARATUS

2.1 Introduction

An MPD arcjet apparatus, designed and built specifically for this study, is described below. Included are descriptions of its discharge chamber, anode, propellant injection system, power supply, gas-triggered switch and vacuum facility. The operation of the device and its voltage-current-mass flow characteristics are also included.

2.2 The Discharge Chamber

The apparatus is shown schematically in Fig. 2.1. The discharge chamber is a 12.7 cm diameter by 5 cm deep cylindrical cavity formed by a Plexiglas insulating ring 0.64 cm thick. It is backed by a 1 cm thick Plexiglas plate surrounding a central, conical, 2%-thoriated tungsten cathode 2.7 cm high with a 1.9 cm base diameter. Around the cathode, arranged at the corners of a regular hexagon, 2.5 cm from the axis, are six propellant injectors. They are made of nylon, have 4 mm orifices and extend 6 mm from the backplate surface. The coaxial anode is 1 cm wide with a 10.2 cm diameter orifice.

2.3 The Shell Anode

The heart of the MPD arcjet under study is the 1 cm wide aluminum shell anode of 1 mm wall thickness. The anode is masked with mylar insulating tape to expose the same surface area for current conduction (~ 260 cm^2) as the

FIGURE 2.1

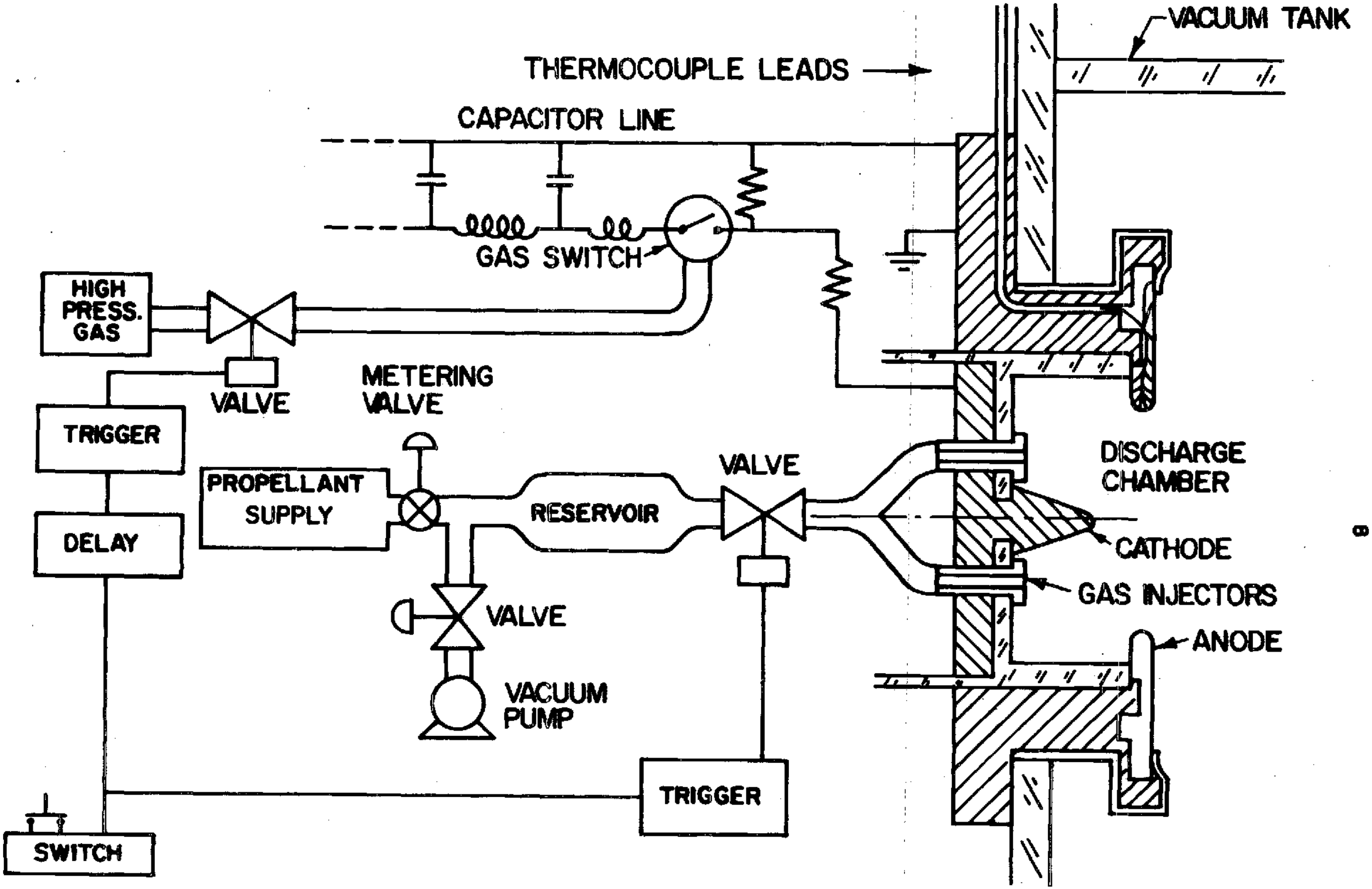

MPD ARCJET APPARATUS (SCHEMATIC)

usual solid anodes employed in this laboratory.(27) The 1 mm anode wall thickness is a compromise between adequate strength and the desire to use a 1-dimensional analysis of heat flow through the shell for the anode heat flux measurements. The anode is set at ground potential by connecting it to a grounded pipe with a #16 ga (1.3 mm diam) insulated copper wire.

2.4 Propellant Metering and Injection

Argon propellant from a gas bottle supply is fed to a 300 ml cylindrical reservoir, 5 cm o.d. x 24 cm overall length. The downstream end of the cylinder is fitted with an electrically actuated valve which leads to the injectors. The upstream end is connected by one side of a "T" to the supply via a metering valve, while the other side of the "T" connects the cylinder, through a valve to a vacuum pump. For operation with plenum pressures above atmospheric upsteam of the valve (for argon mass flows greater than 2 g/sec) adjustment of bottle pressure meters the propellant,and for operation requiring subatmospheric pressures, the cylinder is isolated from the gas supply bottle and its pressure is adjusted by the valve and vacuum pump combination. The reservoir is large enough to maintain essentially constant mass flow of propellant throughout the complete discharge. The valve is opened in about 2 msec using an electronic trigger (Fig. 2.2),(13) (Fig. 2.2),(42) by suddenly overdriving the 12 volt rating of the valve solenoid by a factor of 10. Constant mass flow is established after the valve response risetime of less than 3 msec.(43)

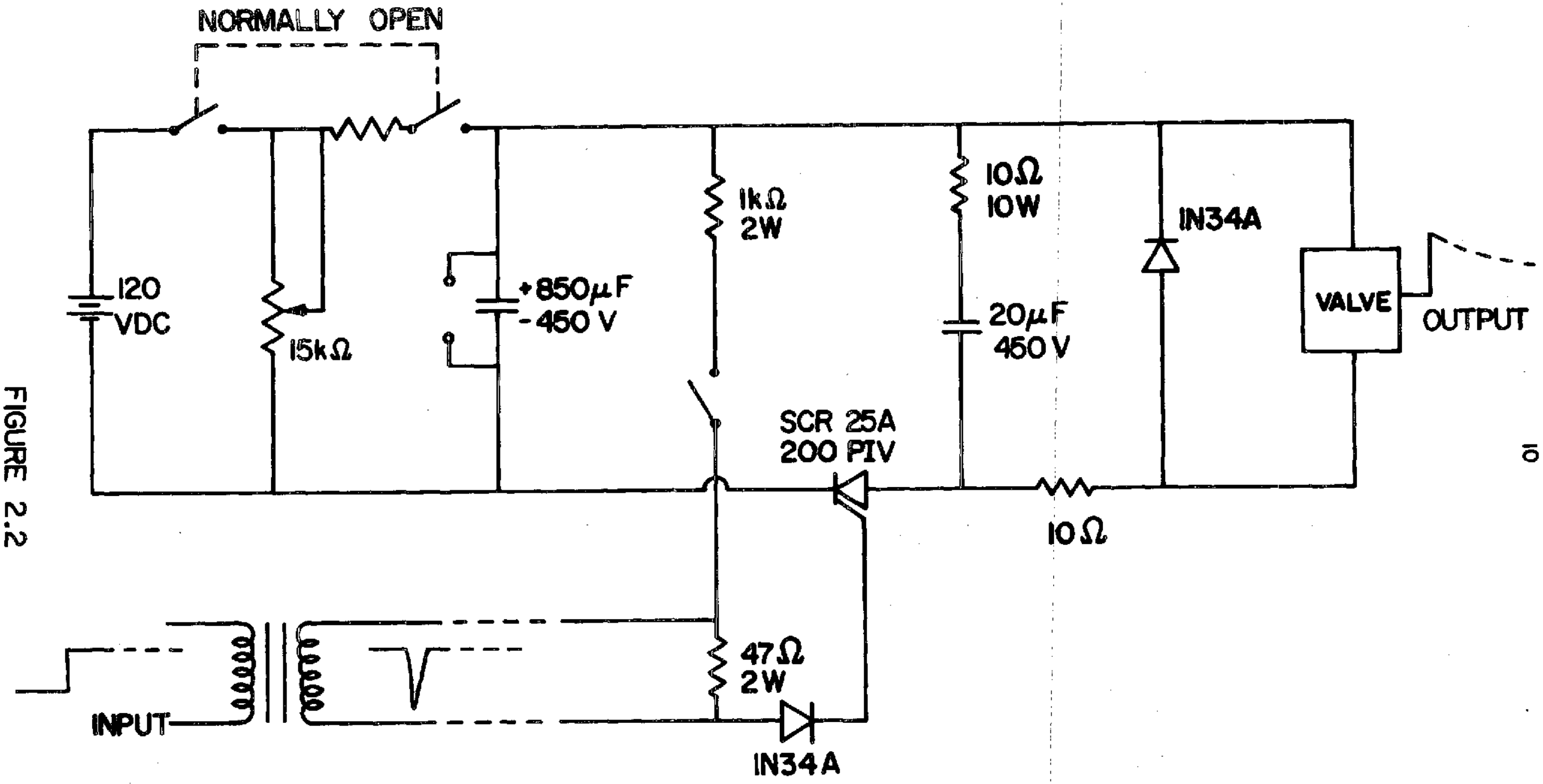

FIGURE 2.2
AP25-5035

VALVE TRIGGER

Mass flow is calibrated against reservoir pressure using a Varian "Millitor" (T.M.) fast ionization gauge mounted on axis 1 cm from the cathode tip, to determine the duration of the constant mass flow and a McLeod gauge to determine the pressure rise in the vacuum tank, for a cold flow (no arc discharge). The experimentally derived proportionality between pressure and mass flow is constant, demonstrating that the flow is choked at a constant area.(100) The accuracy in the calibration is ±5 %, determined by the deviation of the calibration data from a straight line.

The mass flow into the thruster is limited on the low extreme (1 g/sec) by proper seating of the valve and on the upper (50 g/sec) by the gas reservoir pressure which holds the valve shut.

2.5 Power Supply

A rectangular, nonreversing, current pulse is supplied to the discharge chamber by a 160 kilojoule, 3300 μF, capacitor bank with a total stored charge of 24 kA-msec, i.e. Coulombs, when charged to 8 kV.(44) This power supply, an L-C ladder network (Fig. 2.3) consists of 119 series inductors and 120 shunt capacitors (G.E. Capacitor Unit, Cat. No. 14F641). The capacitors are housed in a plywood rack 30 units across by 4 units high. Since each capacitor has its own compartment in the rack, adjacent units are protected in case of failure. One terminal of each capacitor is connected to the inductance line using a 10 cm long fuse of #16 ga (1.3 mm o.d.) tinned copper wire enclosed in a nylon sleeve. The other terminal, and for safety the metal capacitor case, are connected to ground. The inductors, fabricated from 3.8 cm wide x 0.32 cm thick copper strip, have three 10 cm i.d. x 6.4 cm pitch turns between capacitors. The end of each tier is connected to the next by an

FIGURE 2.3
AP25 P419

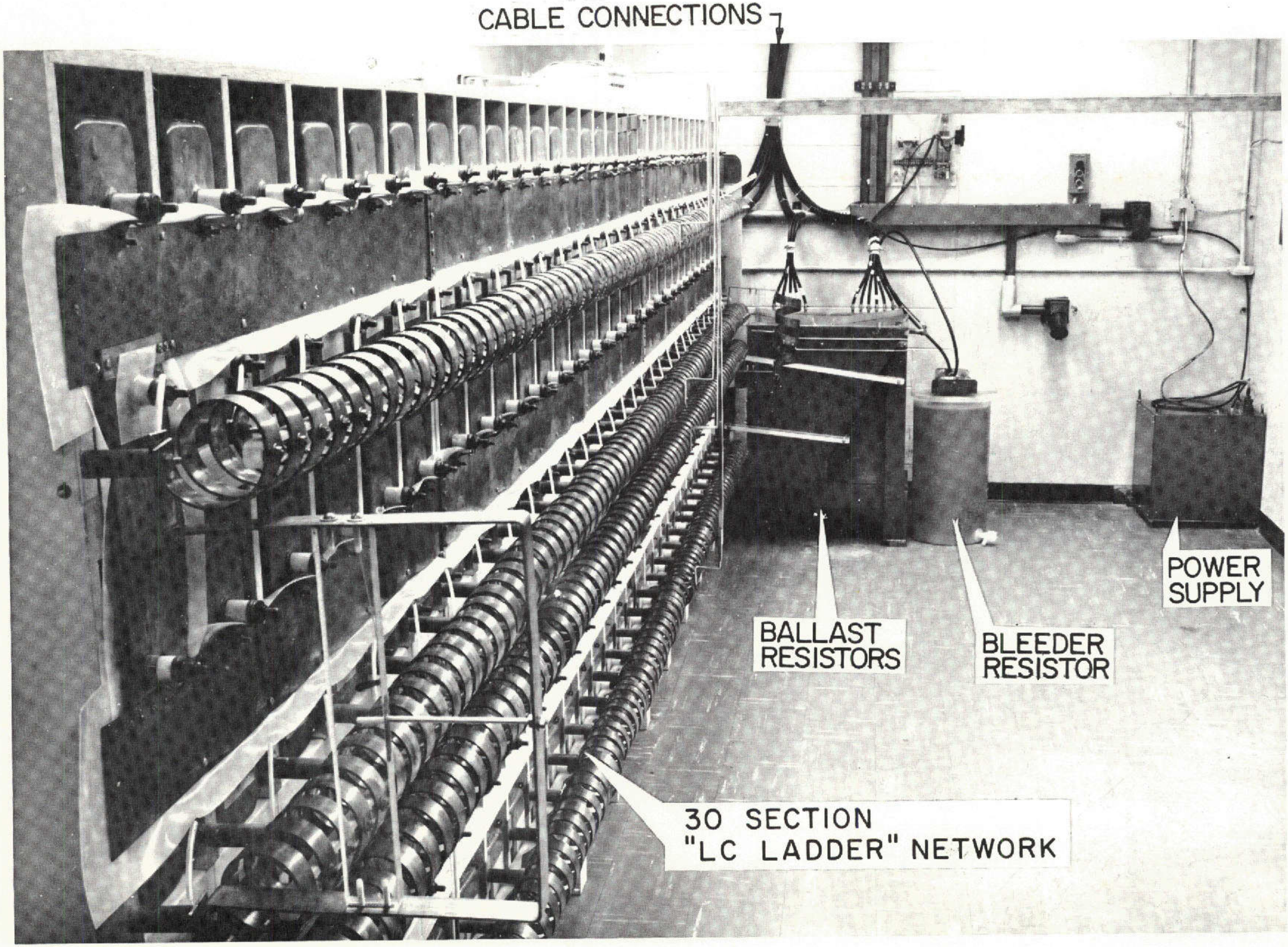

VIEW OF POWER SOURCE

inductor designed to maintain the flatness of the current pulse.

The pulse is made nonreversing by matching the source impedance (ladder-network) to the load impedance (MPD arc) using a ballast resistor for each tier in the form of an electrolytic cell consisting of two copper plates of 2000 cm^2 surface area on each side immersed in a 60 liter vat filled with 0.58 molar cupric sulphate solution.

The tiers can be connected in different arrangements. For example, in series for a 900 μsec pulse (maximum current: 26 kA); a pair of two series-connected tiers in parallel for a 450 μsec pulse (maximum current: 52 kA); or all four tiers in parallel for a 225 μsec pulse (maximum current: 104 kA).

2.6 The Gas-Triggered Switch

The power supply is connected to the accelerator through a gas-triggered switch shown schematically in Fig. 2.4. The switch is formed from two 13.8 cm diameter by 1.9 cm thick stainless steel plates separated by a 12.7 cm i.d. x 5 cm long Plexiglas ring with a 0.64 cm wall. The assembly is housed in a cylindrical aluminum case, which also forms part of the electrical return path to the power supply. The switch is prepared for a pulse by being evacuated to about 10 mtorr absolute pressure via a hole in one plate, through a vacuum dump tank, by a mechanical pump. Nitrogen gas, passed into the switch through an electrically actuated valve and a diffuser mounted in the opposite plate triggers electrical breakdown allowing current to flow.(45)

2.7 Vacuum Facility

The vacuum facility is shown in Fig. 2.5. The accelerator is mounted in the end of a 45 cm diam x 76 cm

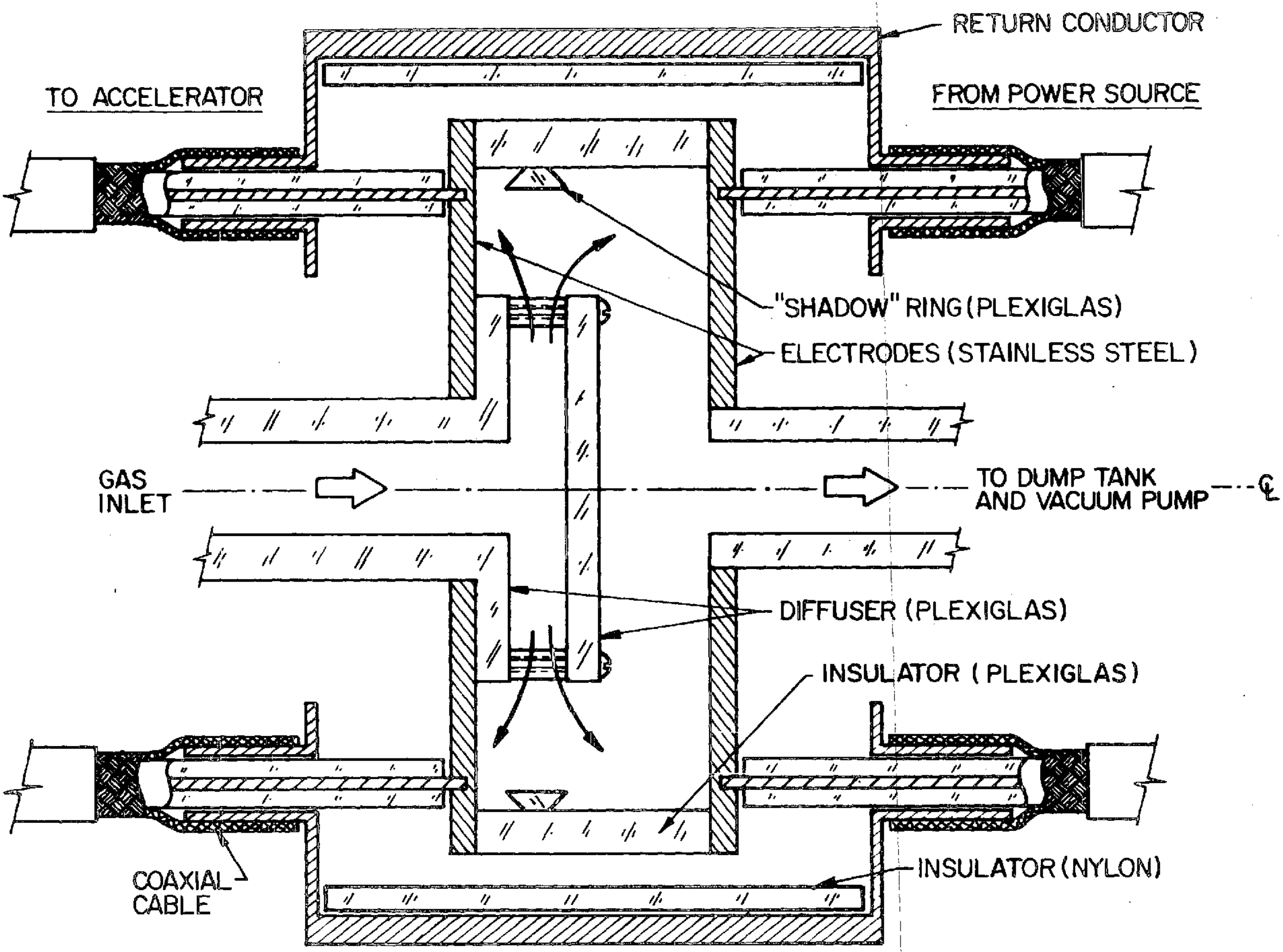

SCHEMATIC OF GAS SWITCH

FIGURE 2.4

AP25 4770

FIGURE 2.5
AP25-5039

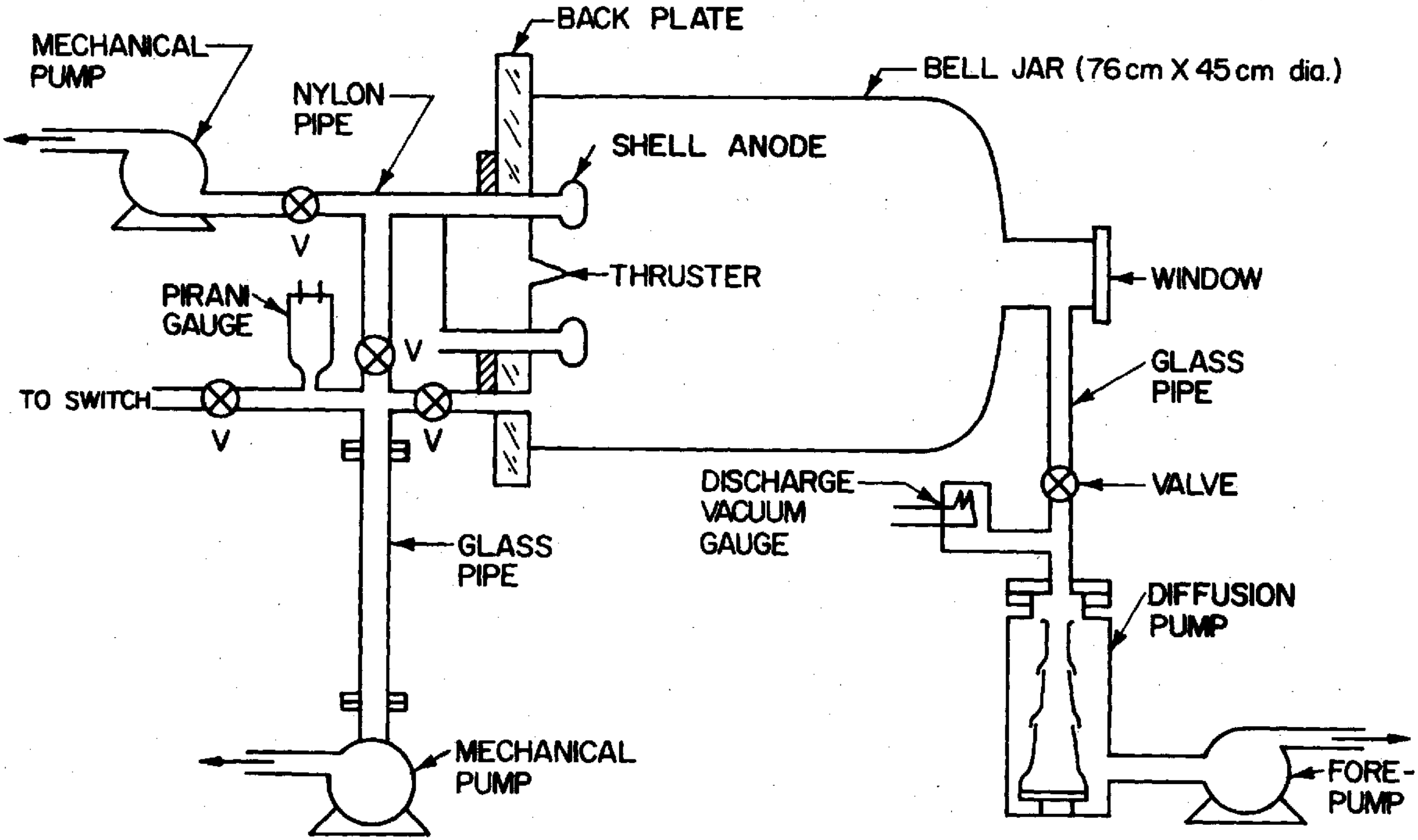

VACUUM FACILITY

diameter access ports, one on the end and the other on the side. The background pressure of about 10^{-2} mtorr is established by using a 5 cm oil diffusion pump with a 425 liter/minute (free air) mechanical forepump. A 2.5 cm thick Plexiglas slab sealing plate with 0.64 cm thick aluminum backing for support is fitted with a manual probe mount and traverse mechanism capable of moving diagnostic probes radially and axially throughout the discharge without opening the system. For safety, the entire assembly is mounted on a table and housed in a Plexiglas case, behind a Plexiglas wall.

2.8 Operation of the MPD Apparatus

To operate the thruster, the capacitor bank configuration is arranged and the power supply connected to the gas switch. The vacuum tank backpressure is established, usually at 10^{-2} mtorr. The capacitors are then charged to the voltage appropriate for the current desired. Closing the firing switch triggers the propellant valve and initiates an electronically delayed pulse which trips the gas switch valve. Precise delay of the discharge is necessary to achieve proper arc operation.(23) If the delay is too long, the large amount of propellant mass injected prior to the discharge increases the backpressure in the vacuum tank and compromises the simulation of a space environment. If the delay is too short, the discharge is initiated before the mass flow is steady, resulting in time-varying discharge processes. After the completion of the discharge cycle, the system is evacuated in preparation for another pulse.

2.9 Current-Voltage-Mass Flow Characteristics

The apparatus is operated with arc currents from 5.5 to 44 kA and injected argon propellant mass flows from 1 to 48 g/sec.

The current is measured using the passively integrated,(46) output of a 340-turn, calibrated Rogowski loop encircling the discharge chamber.(47) The arc voltage is simultaneously monitored with a Tektronix 6013A, 10^3 times attenuating, $10^8 \Omega$ impedance, voltage probe, mounted at a cathode connection. A typical response, for 900 μsec operation at 16 kA arc current and 24 g/sec injected argon mass flow is shown in Fig. 2.6. The current rises in about 10 μsec while the voltage has an initial transient of about 150 μsec after which it holds a steady value of about 80V, until the discharge ceases. The term "quasi-steady" has been applied to this later period during which relatively constant operation ensues.(23)

Terminal voltages of the discharge for various arc currents and argon mass flows are shown in Figs. 2.7 and 2.8, respectively. None of the characteristics is a straight line: between two apparently curved sections there are jumps noticeable in all the characteristics. The terminal voltages agree with those of a like-geometry thruster mounted in a 1 m diam x 2 m long Plexiglas vacuum tank.(22)

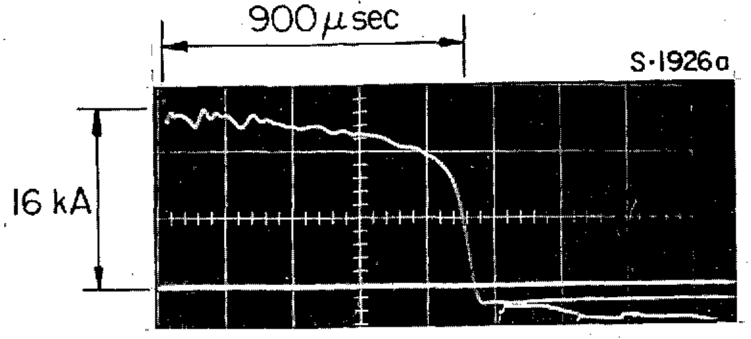

a) ARC CURRENT

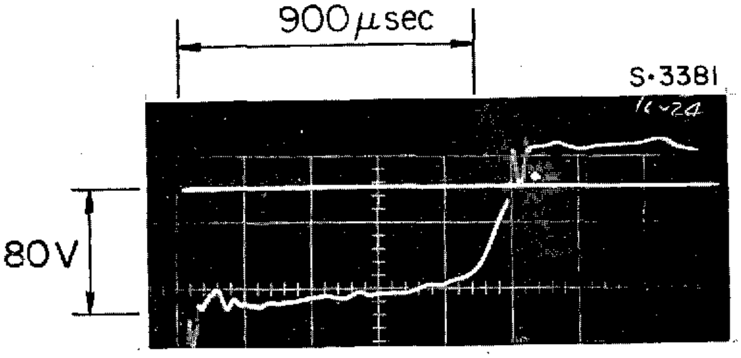

b) ARC VOLTAGE

CURRENT AND VOLTAGE
SIGNATURES
16 kA, 24 g/sec

FIGURE 2.6

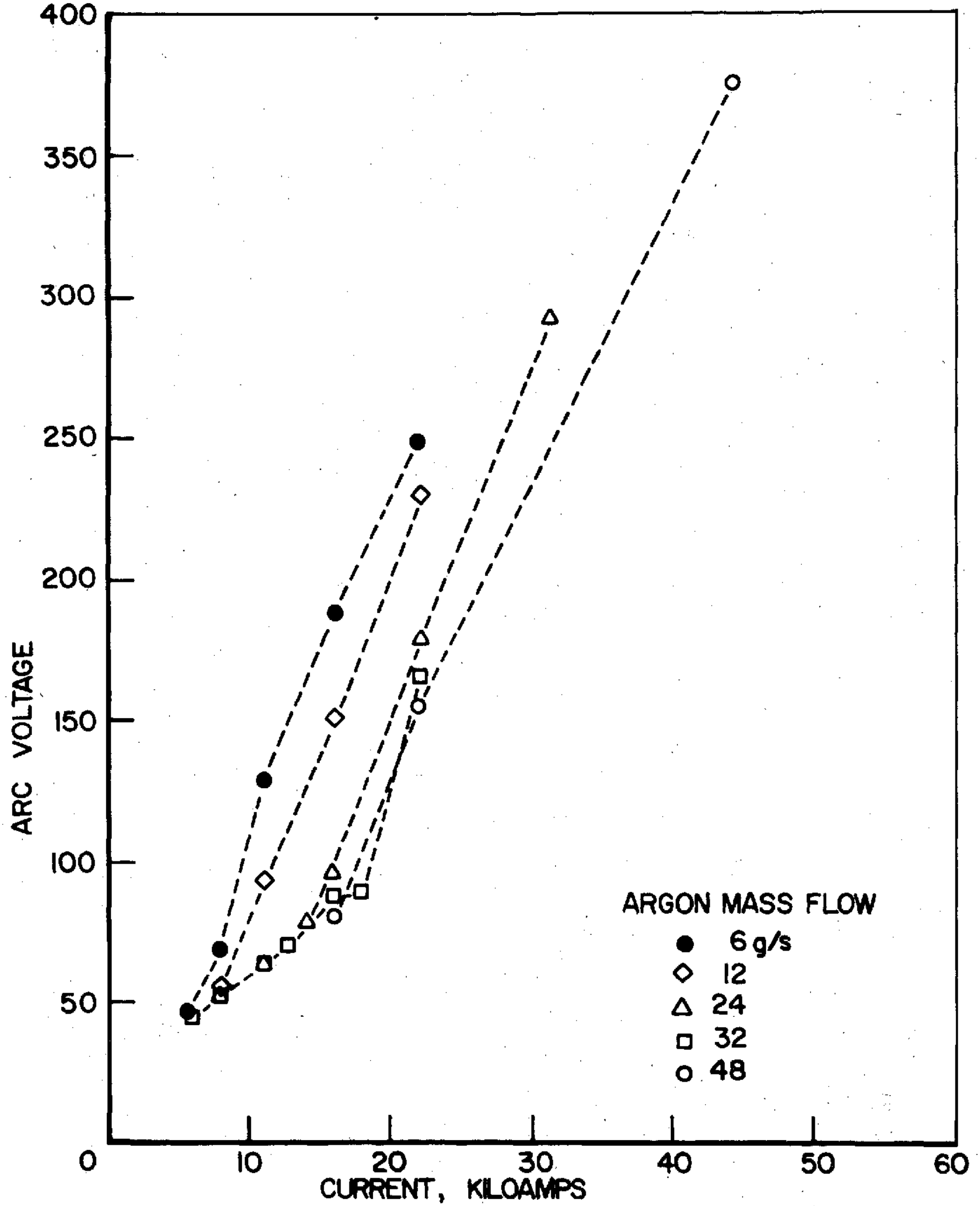

VOLTAGE: CURRENT CHARACTERISTICS

FIGURE 2.7

AP25-5038

FIGURE 2.8

AP25·5037

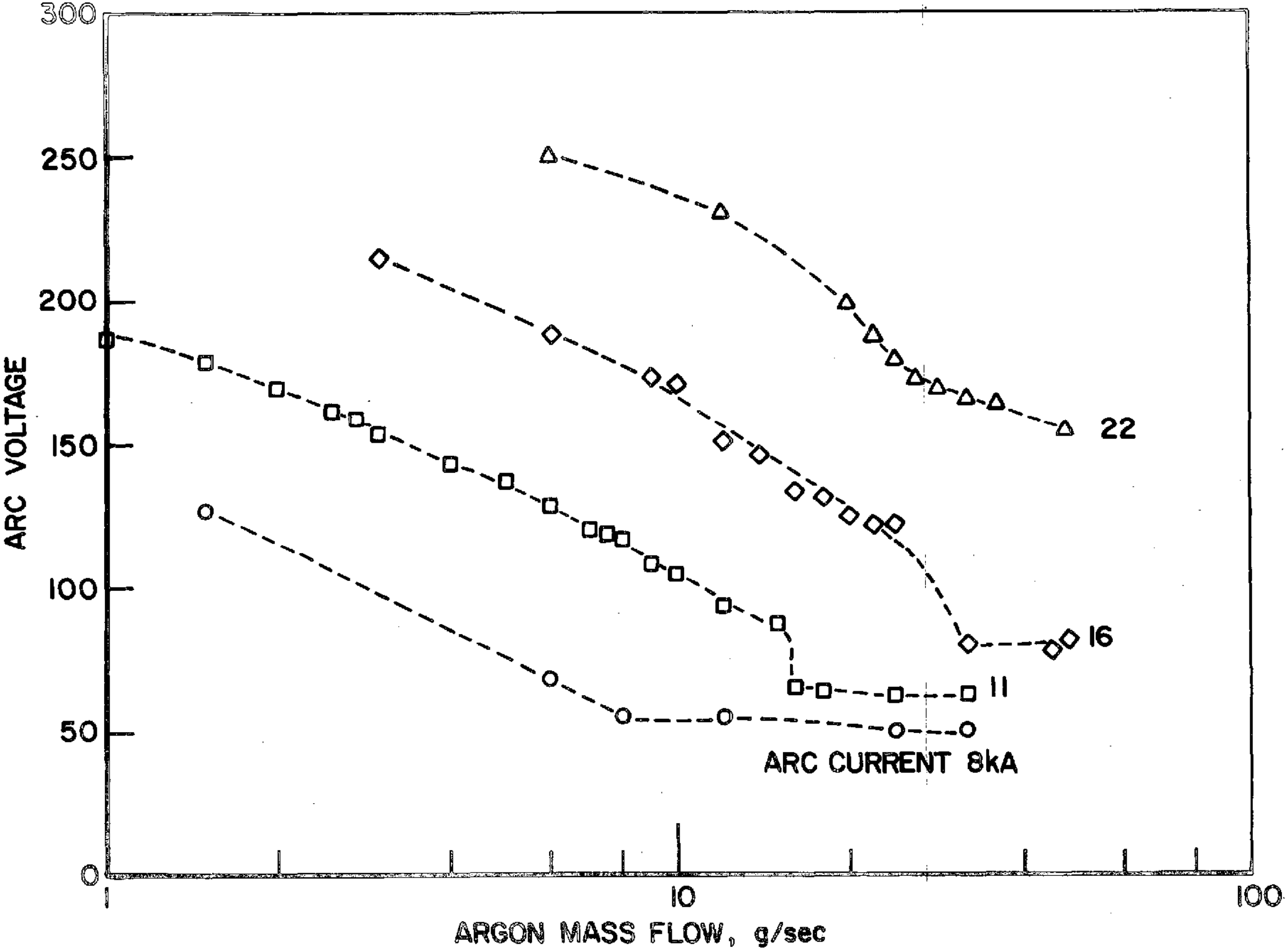

VOLTAGE:MASS FLOW CHARACTERISTICS

CHAPTER 3
ANODE HEAT FLUX AND POWER

3.1 Introduction

The direct measurement of anode heat flux and power are described in this chapter. The calorimetric technique employed uses thermocouples attached to the inside surface of a hollow shell anode in a series of experiments over a range of arc powers from 200kW to 20MW, using arc currents from 5.5 to 44 kA with argon propellant mass flows from 1 to 48 g/sec. The reader is referred to Appendix E for a compendium of all the results.

3.2 Anode Temperature Rise

The MPD thruster anode has a 1 cm wide anode with a 10 cm diam orifice. These dimensions permit use of a shell anode with a 1 mm wall (Fig. 3.1). The anode is internally fitted with twelve #34 ga (0.16 mm diameter) copper-constantan thermocouples.(48) The thermocouples are welded to the inside surface within a 15° arc, usually radially opposite a propellant injector. Two are in the chamber side (A,B), five in the lip region (C,D,E.F.G) and five in the downstream face. These thermocouple junctions, formed by arc welding wire ends directly to the inside surface of the shell, are the "hot" junctions for the measurement.

To measure changes in their potential, every thermocouple inside the anode is supplied with its own reference "cold" junction thermocouple outside the anode. The cold junctions are individually made by welding the tips of thermocouple wires together and then electrically insulating the resulting bead with epoxy. All twelve cold junctions

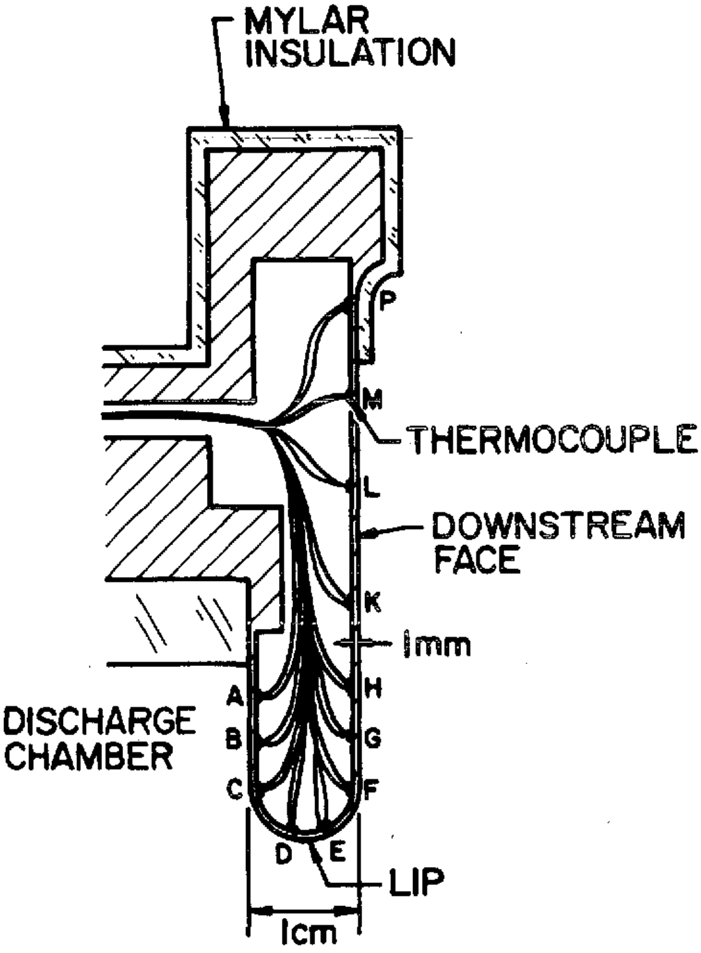

SHELL ANODE

FIGURE 3.1

AP25-5014

are bundled in a Pyrex tube sealed at one end and the package is immersed in a half-liter Dewar flask filled with ice water to maintain a constant temperature.

Each thermocouple pair produces an output voltage which changes with hot junction temperature. This voltage is monitored using the detection circuit seen in Fig. 3.2. The circuit incorporates a 10 kΩ, 22 turn bias resistor to null ambient output due to room temperature. The circuit differentially amplifies by 1000x the net voltage change, which in some cases is only tens of microvolts. The input impedance of the preamplifier is 1000Ω, compared to the 25Ω output impedance of each thermocouple pair.

The amplified output signals of all 12 thermocouple pairs appear simultaneously on Tektronix 555 Dual-Beam oscilloscopes equipped with multiple beam Type M and 1A4 plug-in pre-amplifiers and are recorded on Polaroid film. The amplifier for each thermocouple pair is calibrated over the frequency range from 10 to 1kHz using a sine wave generator and the entire anode-thermocouple-amplifier-oscilloscope calibration is checked by immersion of the anode in a fixed temperature water bath. The time response of the system is 3 msec. It is measured by placing a cube of water ice on one of the hot junction thermocouples and recording the time required for the output signal to drop from room temperature to a constant level for the temperature of the ice.

Connections between dissimilar conductors anywhere in the circuit produce potential differences changing with temperature. Therefore, the introduction of an error resulting from differentials in ambient temperature between the connections of the hot and cold thermocouples in each pair is precluded as shown in Fig. 3.2. The constantan leads of the hot and cold junctions are welded together and

FIGURE 3.2

AP25.5036

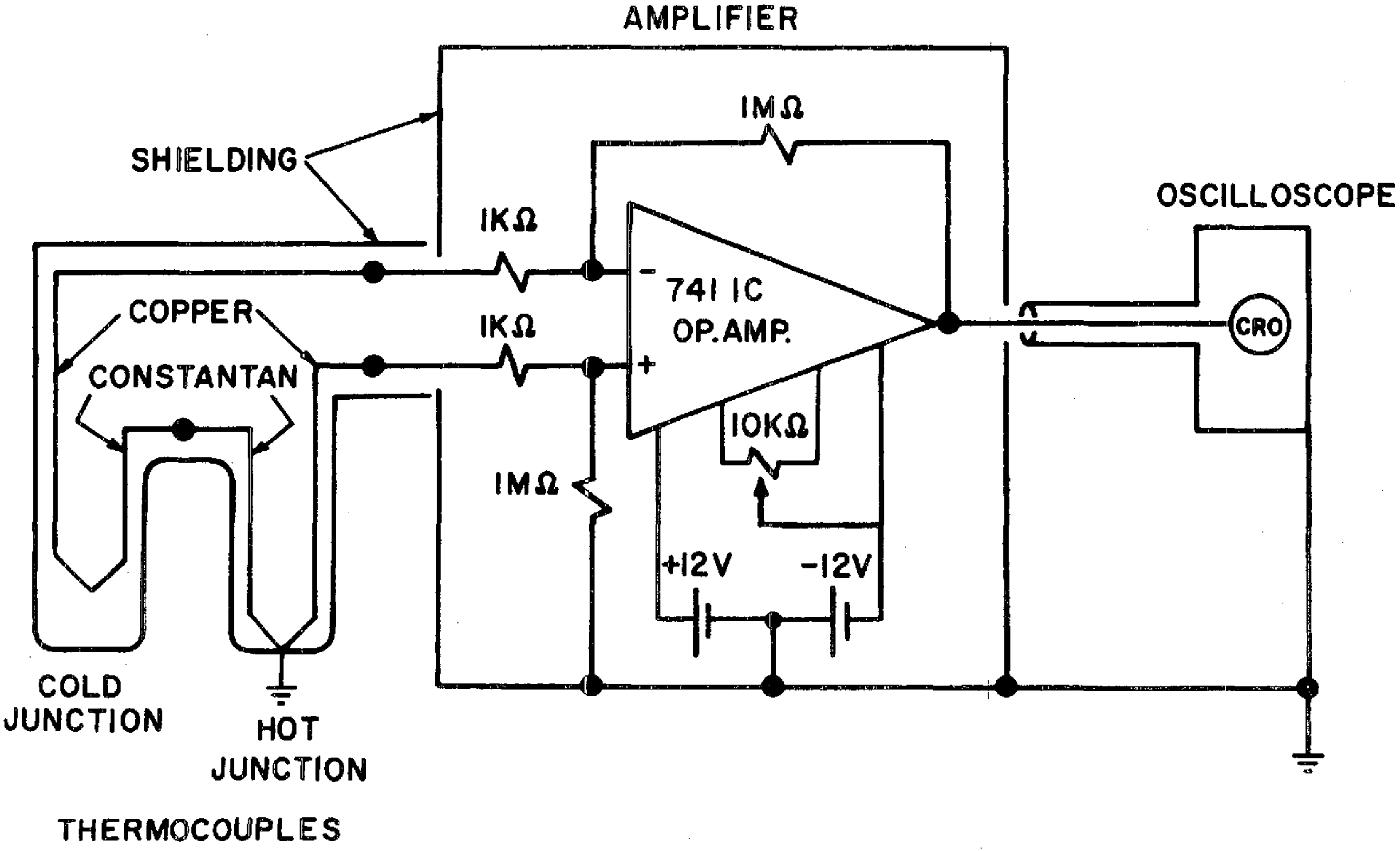

THERMOCOUPLE CIRCUITRY

the copper wires from each thermocouple pair are soldered to the copper input buss of the amplifier.

The MPD discharge pulse generated substantial electromagnetic noise. To eliminate it, inductance of the circuit is minimized by using sub-miniature components in construction and by twisting all leads in pairs; and capacitive coupling to the high voltage discharge breakdown potential is reduced by covering the detection circuit and all of its connections with a copper shield grounded to the anode.

Response of the detection system to a 900 μsec long discharge with 16 kA arc current and 6 g/sec injected argon propellant is illustrated in Fig. 3.3. Thermocouple signals do not begin until the initiation of the discharge, shown on the 5 msec/div time scale. When the discharge starts, electromagnetic noise distorts the baseline and the output of the thermocouple detection circuit. However, the noise subsides during the 10 msec required for the temperature increase of the unheated side of the anode shell to be nearly complete, when the output signal becomes almost constant. Subsequently, the outputs of cooler thermocouples (A,B,C,H,K,L,M) continue to rise, while those of relatively warm thermocouples begin to droop. Data are examined 20 msec after initiation of the discharge, when the noise has subsided and heat conduction along the shell is still negligible (Appendix A). One of the thermocouples, P, is situated under mylar electrical insulation at the periphery of the plasma-exposed region of the anode. A temperature rise at its location is due only to current conduction along the anode and its response is null for the first 10 milliseconds following the discharge. Therefore, any temperature rise due to Ohmic dissipation in the aluminum anode is neglected. The signal at later times is due to heat conduction from the adjacent anode region which is exposed to plasma.

Operation is repeated 3 to 10 times at each current and mass flow condition, the thermocouple output voltage is averaged, and the temperature rise is then calculated

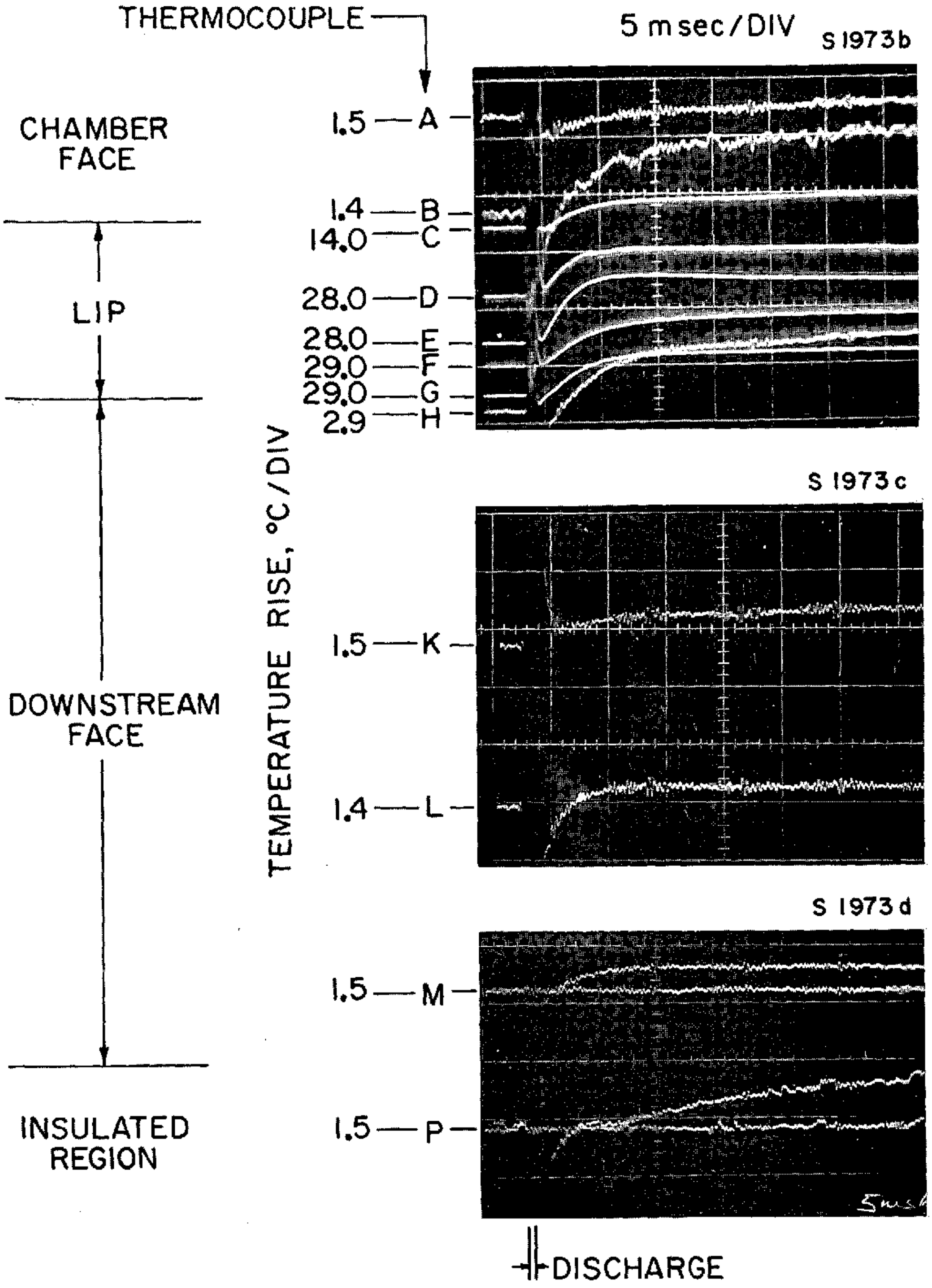

THERMOCOUPLE RESPONSE
16 kA, 6 g/sec

FIGURE 3.3
AP25·486

from the thermocouple calibration. The temperature rise due to a 900 μsec long discharge at 16 kA arc current and 24 g/sec mass flow is shown in Fig. 3.4. The abscissa represents a linearly rolled-out anode: it traces a line of constant azimuth along the conduction surface. The axis runs from the chamber insulator (shown as a cross-hatch), around the lip (with midplane at 0.0 cm) almost to the boundary of the conduction region on the anode face (at about 4.5 cm). The temperature rise peaks at about 20°C at the lip and drops to less than 0.5°C on the downstream face and to 0.1°C on the chamber side. The error bars shown represent one standard deviation of the sample.(49) The temperature profiles measured are all peaked markedly at the lip. The values there are more than an order of magnitude higher than those on the face or inside the discharge chamber.

3.3 Local Anode Heat Flux

The local anode heat flux during the quasi-steady discharge is derived from the measured temperature rise on the inside of the anode shell. Heat supplied to the plasma-exposed side of the anode is presumed to be conducted through the shell wall, increasing the temperature of the inside surface. Once the temperature rise on the inside surface is measured, and the heat flux problem formulated, the local anode heat flux can be derived.

The assumptions underlying the analysis follow.

a) Heat flux to the anode is constant during the discharge and zero at other times. Initiation and termination transients are negligible for quasi-steady discharge pulses larger than 450 μsec. Thus, all heating is steady and confined to the discharge period. Indeed, a more detailed analysis is not warranted since fluctuations in the heat

FIGURE 3.4
AP25.5040

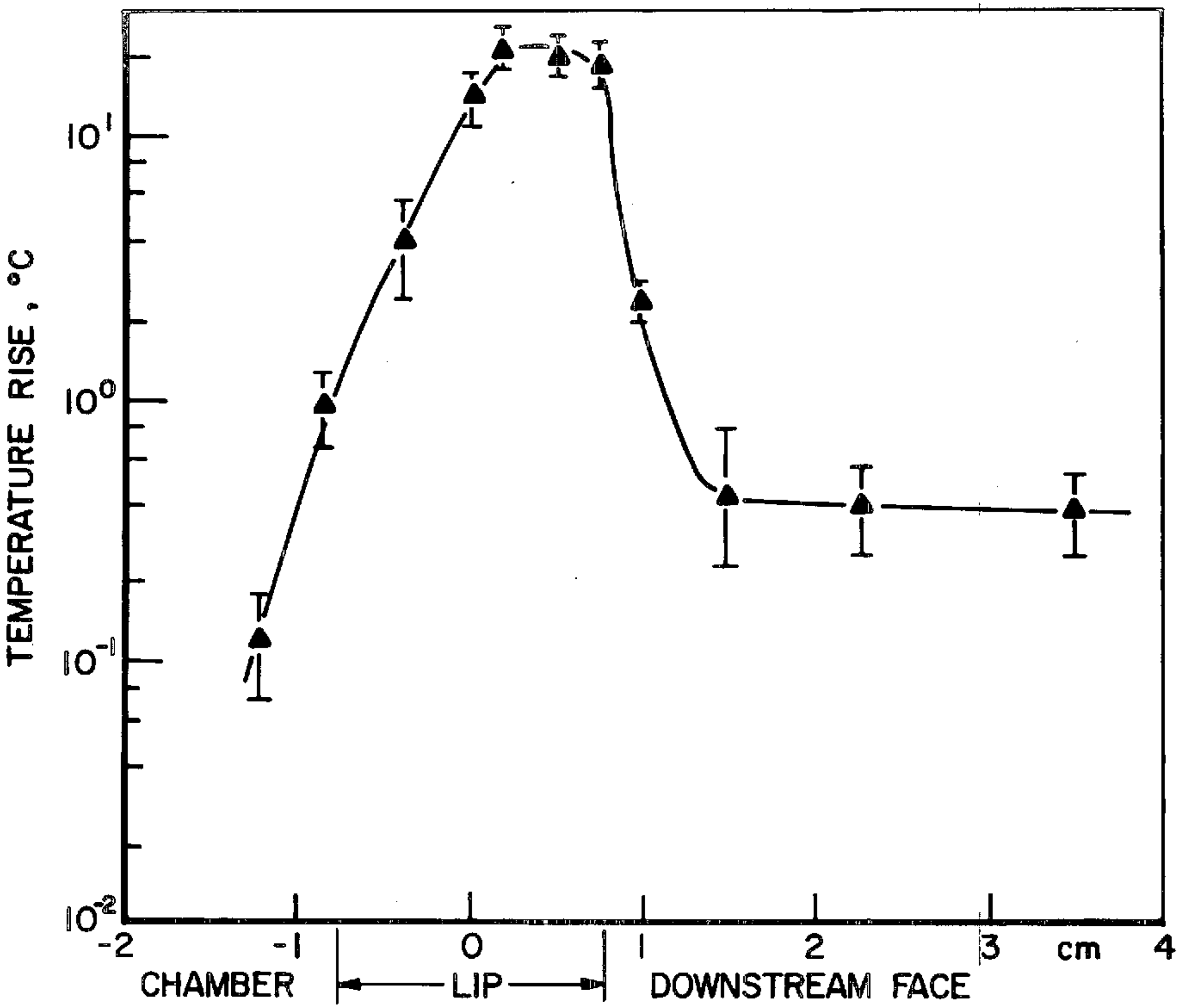

ANODE TEMPERATURE PROFILE
16 kA , 24 g/sec

flux during the discharge are smoothed out in the conduction process through the anode shell.

b) Heat conduction along the shell can be neglected in comparison with conduction through the shell, since temperature gradients along the shell produce negligible heat fluxes compared to those through the shell (Appendix A).

c) The anode is assumed to be locally flat everywhere, since the anode is flat on the face and discharge chamber sides and the radius of curvature of the lip is much greater than the shell thickness.

d. Ohmic heating of the shell due to current conducted along it can be neglected. This is verified by the negligible response of thermocouple P located under the mylar anode masking, immediately following the discharge and by analysis of current conduction through aluminum slabs.

e) The temperature of the anode surface does not become large enough for radiated heat flux to be significant.

f) The anode does not ablate and therefore power to erode the anode is neglected. Local spot attachment of the arc is also neglected.

The heat conduction analysis uses a time-averaged local anode heat flux q_a defined at each thermocouple by

$$q_a = \frac{1}{T}\int_0^{t_f} q_a'(\tau)\,d\tau \qquad (3.1)$$

where $q_a'(\tau)$ is the actual anode heat flux, which may be a function of time; T is the discharge time; and t_f usually equal to the discharge time, is the time at which all heat flux to the anode ceases. This formulation suppresses any time-varying details of the heat flux during the discharge.

If an annular anode section is associated with each thermocouple, then heat conduction through the shell wall can be analyzed as a series of one-dimensional heat flows through those slabs. For each section, the temperature rise on the unheated side of the shell is known, and the heat flux is assumed constant for its duration, therefore the heat flux problem can be solved in reverse: What heat flux produced the temperature rise?

The result can be determined from the following re~~lation (Appendix A):~~

$$\theta(t) = q_a \left[\frac{T}{\rho \ell c} \quad \frac{\ell\, 2}{k_t \pi^2} \left\{ \sum_{n=1}^{\infty} \frac{(-1)^n}{n^2} \left[\exp\left(- \frac{\kappa n^2 \pi^2 \tau}{\ell^2} \right) \right] \Bigg|_{\tau = t}^{\tau = t - T} \right\} \right] \qquad (3.2a)$$

$$= q_a \Phi(t) \quad , \quad t > T \qquad (3.2b)$$

for the temperature rise, $\Theta(t)$ on the unheated side of a uniform slab of thickness ℓ, at time $t > T$ (the pulse duration) due to a heat flux q_a uniform over the surface of the opposite side begun at $t = 0$. For aluminum,(50)

c = specific heat = 0.903 joules/(g-°C)

ρ = density = 2.70 g/cm^3

k_t = thermal conductivity = 2.01 W/cm-°C

κ = $k_t/\rho c$ = thermal diffusivity = 0.823 cm^2/sec

The computed temperature rise per unit heat flux $\Phi(t)$ for the actual anode wall thickness of 1.03 to 1.12 mm and a 900 μsec pulse duration is shown in Fig. 3.5a. The rise begins at zero and increases within 10 msec to about 3°C/(kW-cm^2). This value then remains constant since, by assumption, the slab retains all the heat supplied. The appearance of this analytical result agrees with the experimental example shown in Fig. 3.5b. Therefore, local anode heat flux is computed by dividing the

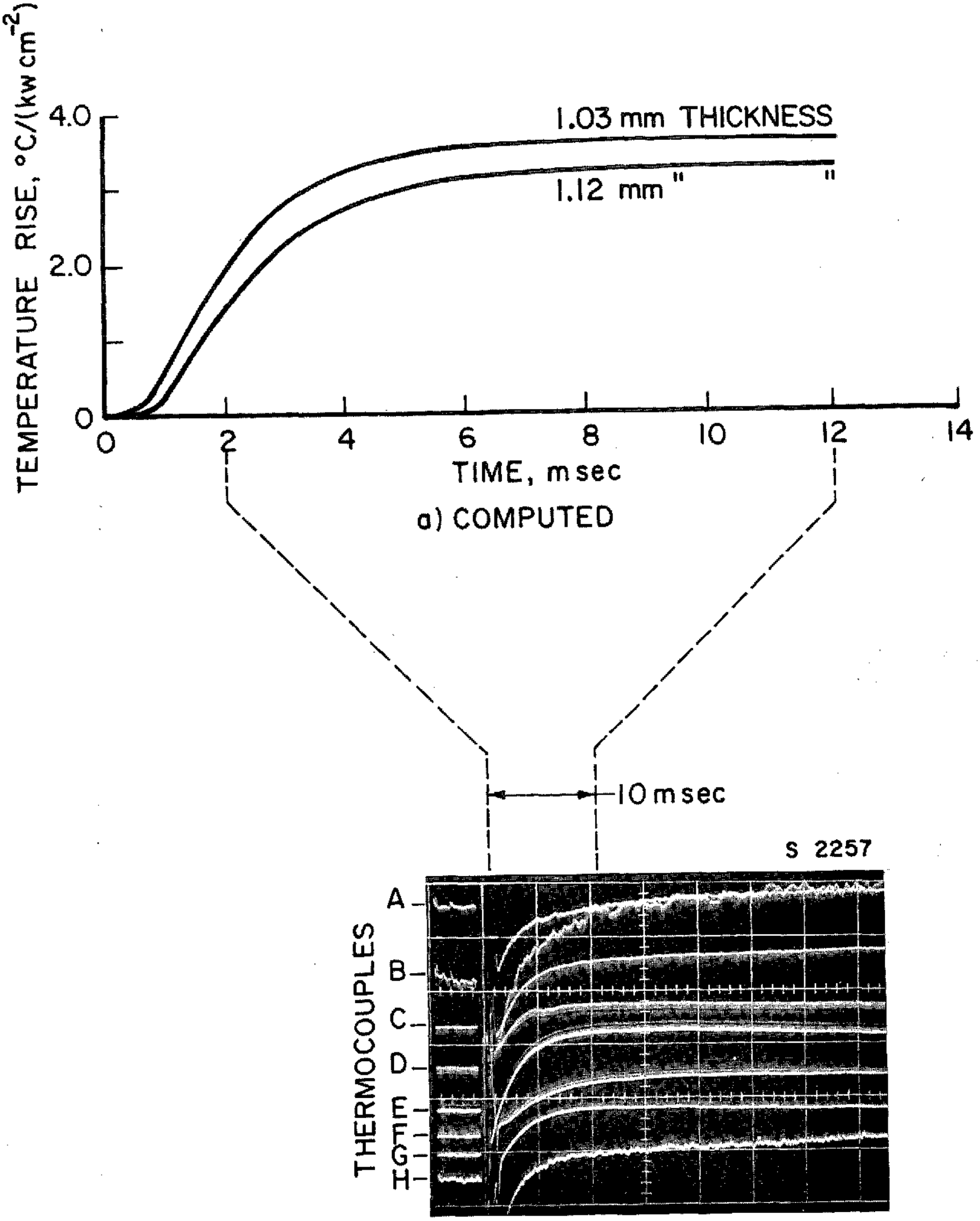

a) COMPUTED

b) RECORDED SIGNAL
16 kA, 6 g/sec

TEMPERATURE RISETIME

FIGURE 3.5
AP25·P·487

experimentally measured temperature rise due to a discharge pulse by $\Phi(t)$ from Eq. (3.2).

The anode heat flux during MPD arc operation with 16 kA total current and 24 g/sec argon propellant mass flow, computed as described above, appears in Fig. 3.6. Due to the small variations in shell thickness along the anode (1.02 to 1.13 mm), there is a slight difference in the shapes of the temperature and heat flux profiles on the surface. However, just as the temperature profile is peaked at the lip, so is the heat flux. The maximum heat flux is 6000 W/cm^2 over the lip region just downstream of the anode midplane. The heat flux drops to about 100 W/cm^2 on the face and 40 W/cm^2 in the discharge chamber.

The magnitude of the local heat flux changes with current and argon mass flow, discharge duration, vacuum tank back-pressure, and in some cases is different at different azimuthal locations relative to propellant injectors.

The effect on anode heat flux of a threefold increase in current from 8 to 22 kA, while mass flow is held constant at 24 g/sec, is illustrated in Fig. 3.7. The change of current is accompanied by over an order of magnitude increase in local anode heat flux. When the current is raised, the heat flux maximum in the lip region changes from 1000 W/cm^2 to nearly 20,000 W/cm^2 and on the face the change is from 20 to nearly 400 W/cm^2. It is interesting to note that, for a mass flow of 24 g/sec, the heat flux on the anode face when arc current is 22 kA is about half the maximum heat flux at 8 kA. In comparison to operation with different currents, if current is constant at 16 kA, while mass flow is changed from 6 to 48 g/sec, changes in the heat flux magnitude are not very great. However, the pattern of the change is a more

FIGURE 3,6

AP25-5032

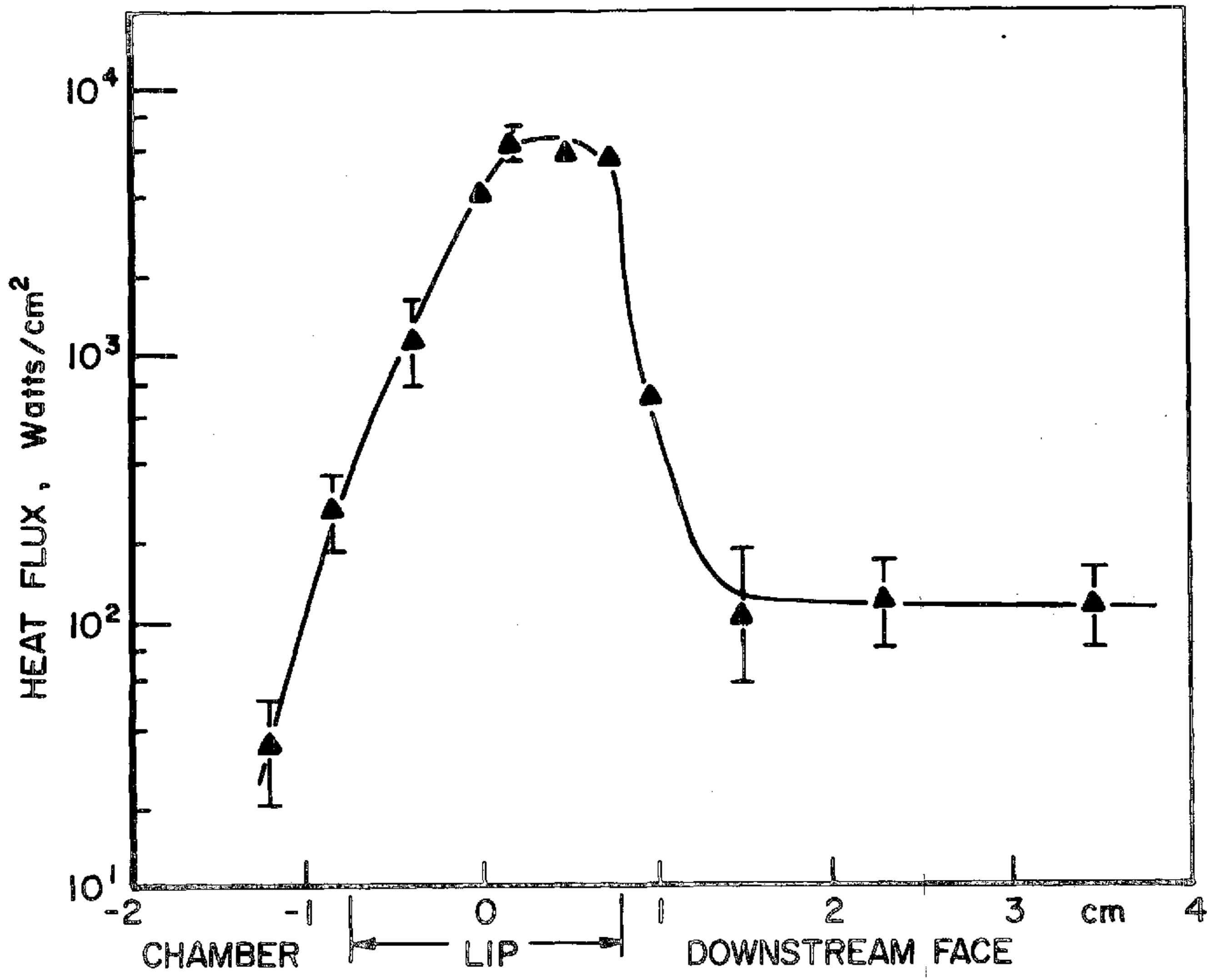

HEAT FLUX TO THE ANODE
16 kA, 24 g/sec

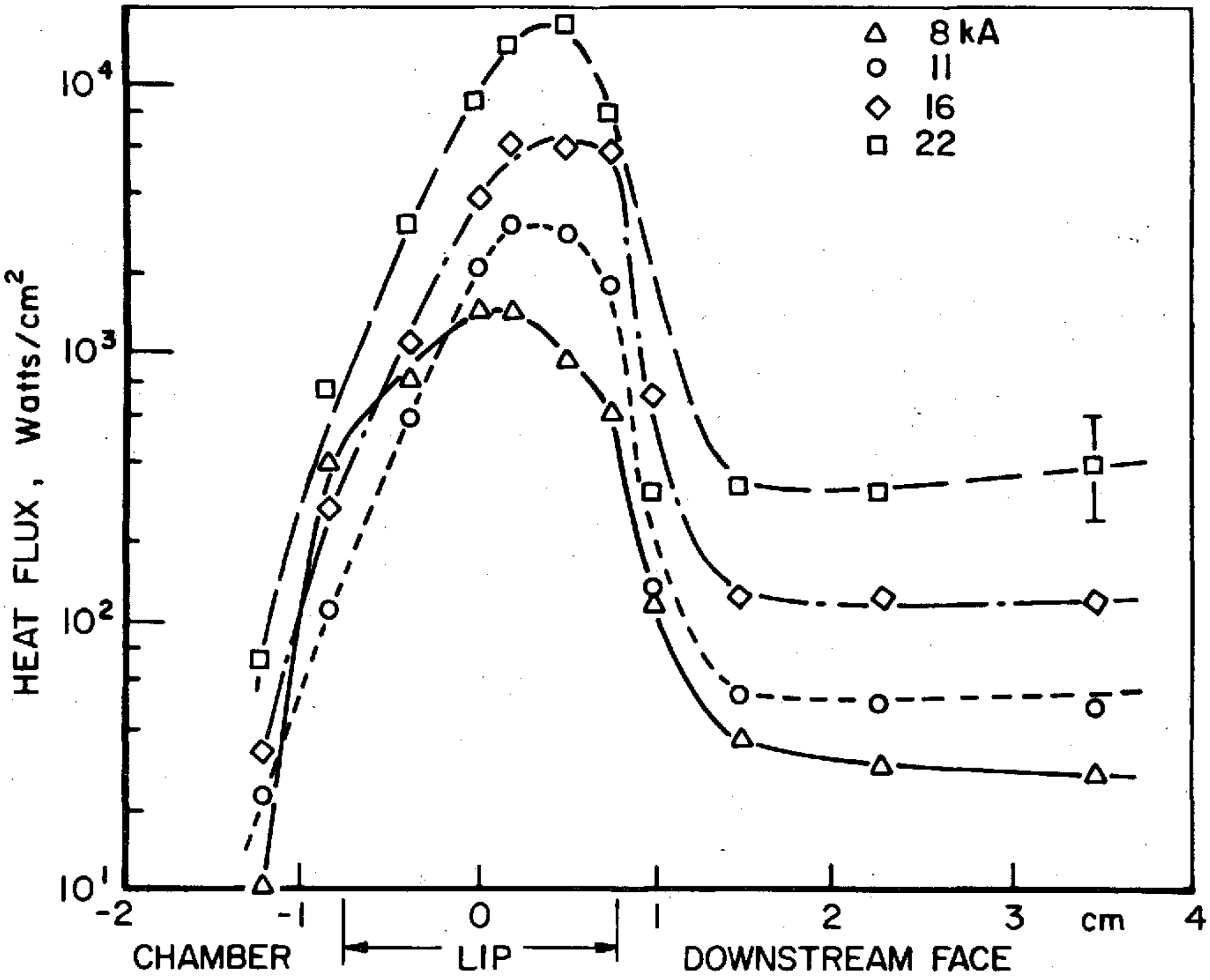

HEAT FLUX TO THE ANODE
24 g/sec

FIGURE 3.7
AP25-5031

complicated. As shown in Fig. 3.8, the heat flux at the lip rises from about 6000 W/cm^2 when the argon mass flow is 6 g/sec to a maximum of nearly 20,000 W/cm^2 at 12 g/sec, and as mass flow is further increased, the heat flux at the lip falls once again. This behavior at the lip is accompanied by a monotonically decreasing heat flux over the discharge chamber side from about 100 to 30 W/cm^2 and over the anode face from 300 to 100 W/cm^2.

These changes in mass flow and current may be accompanied by changes in the character of the arc operation. ~~For example, an increase of current at fixed mass flow~~ may be accompanied by the onset of ablation of insulator and anode material. The result caused by the ablated contaminants is increased number density, an important factor in the explanation of anode power given in Chapter 4.

If the pulse duration is 450 μsec or below, the initial and final transients constitute too large a portion of the discharge period to be neglected. This is seen when the anode heat flux is measured for operation at 16 kA x 6 g/sec for different discharge periods. As seen in Fig. 3.9, the heat flux maximum shifts downstream and the heat flux to the anode face increases when pulse length is increased from 900 to 225 μsec. The change is small, but demonstrates that as discharge time increases the anode heat flux distributes on the anode. Indeed, for some cases where the initial and final transients extend for the full duration of the discharge, the arc is not quasi-steady and increased anode heating upstream is suggested. Transient effects were precluded by studying quasi-steady discharges of over 450 μsec duration.

FIGURE 3.8
AP25-5030

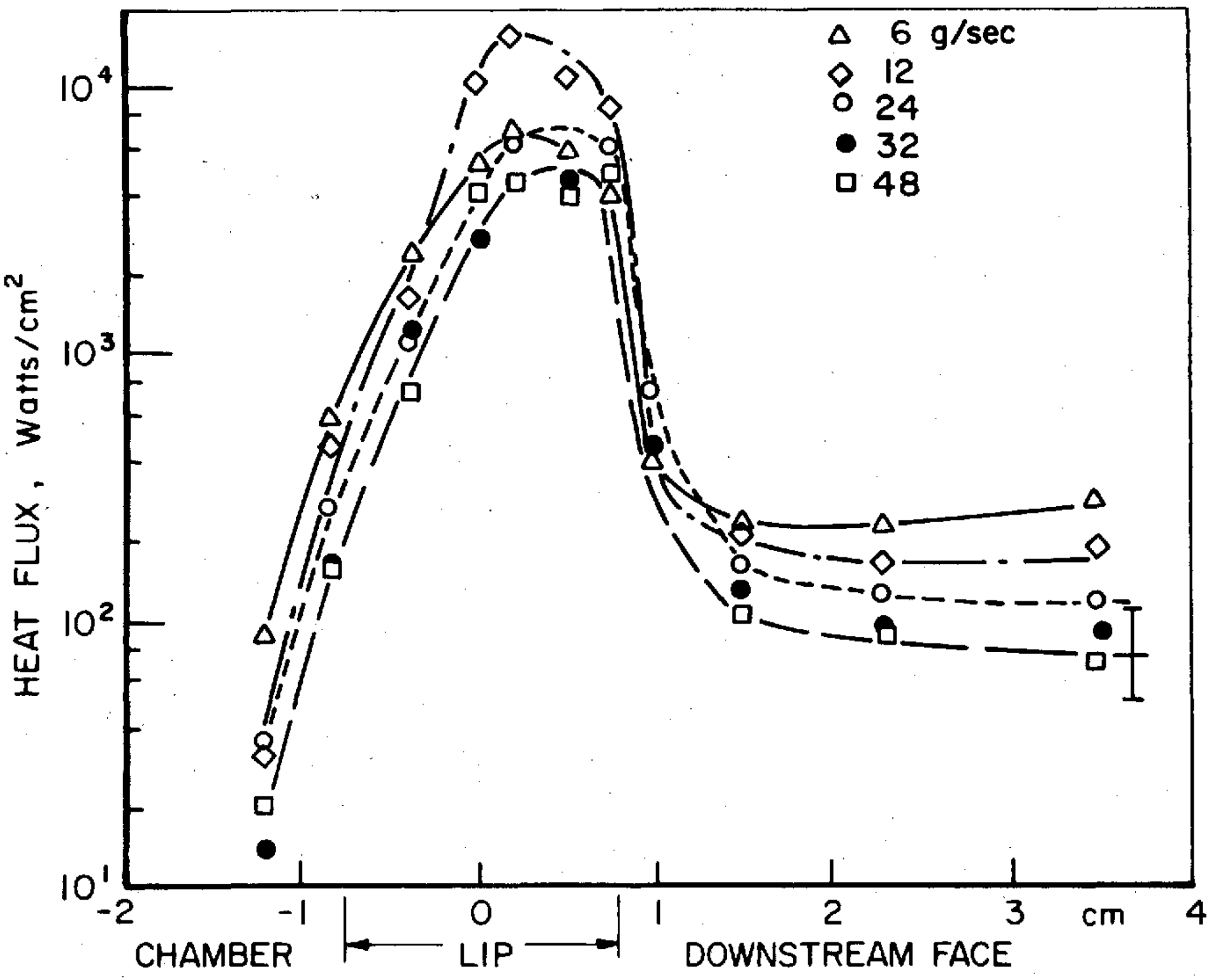

HEAT FLUX TO THE ANODE
16 kA

FIGURE 3.9
AP25-5029

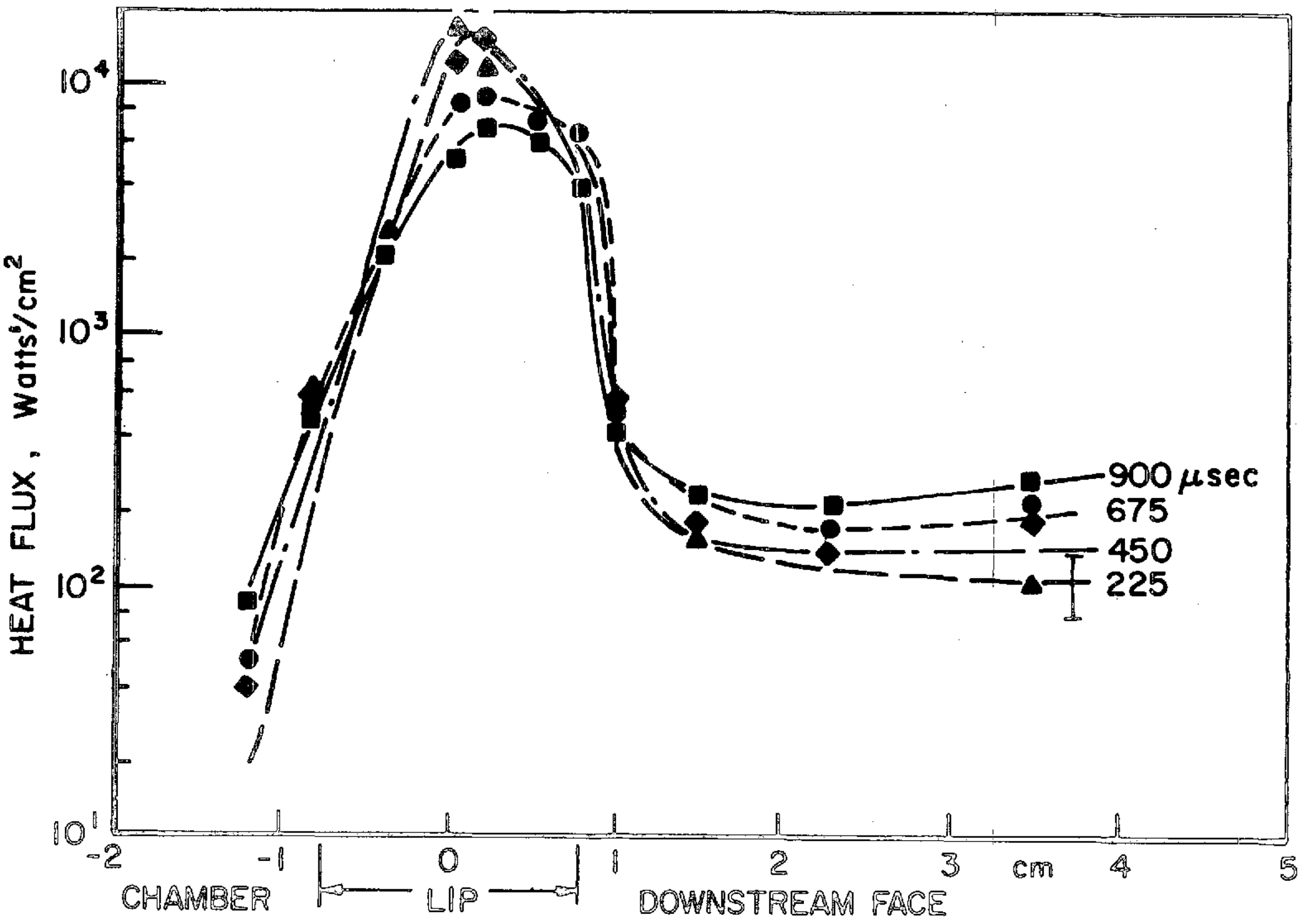

EFFECT OF PULSE DURATION ON ANODE HEAT FLUX
16 kA, 6 g/sec

A changing ambient backpressure can also influence anode heat flux. While other investigations on anode power have used background environments with pressures as high as 1 atmosphere and only as low as 10 torr(31,35), this study has concentrated on anode heat flux for an MPD arcjet exhausting into a 10^{-2} mtorr background pressure. A comparison is outlined for the arc operated at 16 kA arc current and 6 g/sec injected argon mass flow (Fig. 3.10). The backpressure is increased from the usual less than 10^{-2} mtorr to 500 mtorr by prefilling the vacuum tank with argon gas. On the anode face the heat flux decreases only slightly with increasing backpressure, in the discharge chamber it does not change, and the maximum heat flux at the lip decreases by half from 8000 to 4000 W/cm^2 as the backpressure goes up. These changes are not observed at the same current when the mass flow is higher. Hence, one may speculate that the major effect of the higher backpressure is an increased number density in the anode region. The results point out that heat flux measurements must be performed in a vacuum environment closely approximating space conditions if performance is to mirror the results to be expected in space.

Figures 3.6 to 3.10 have presented the heat flux at anode locations along an azimuth opposite gas injectors. However, by rotating the gas injectors 30° around the discharge chamber axis, the heat flux at locations between gas injectors is found. The results are shown in Fig. 3.11, where the heat flux opposite injectors is compared to the heat flux between injectors for a current of 16 kA with 32 g/sec injected mass flow. At the anode midplane (0.0 cm) and upstream into the discharge chamber, the anode heat flux between injectors is higher than opposite injectors. Downstream it is lower than for locations opposite injectors. The azimuthal variation

FIGURE 3.10

AP25·5028

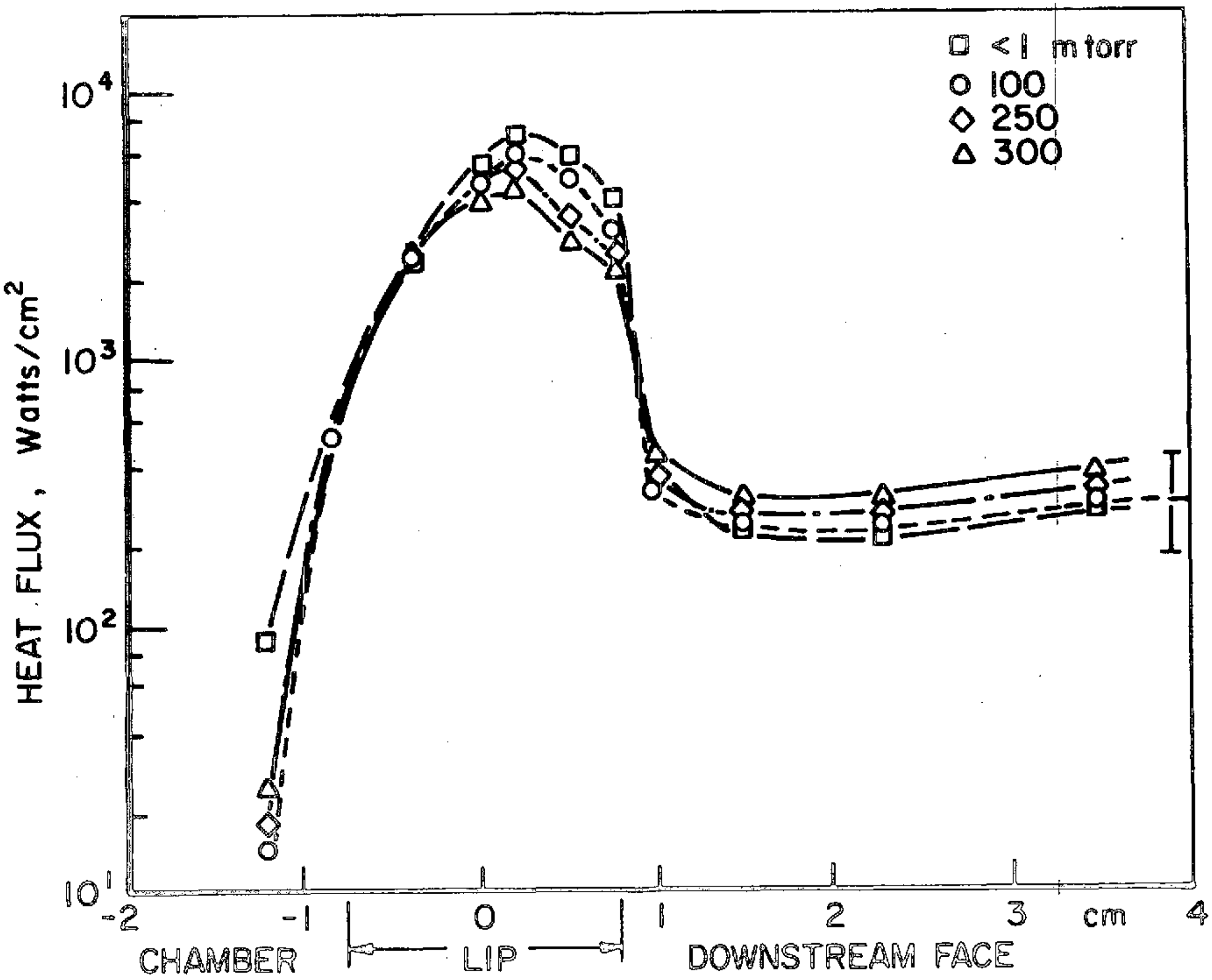

EFFECT OF BACKPRESSURE ON ANODE HEAT FLUX

16 kA , 6 g/sec

FIGURE 3.11
AP25-5027

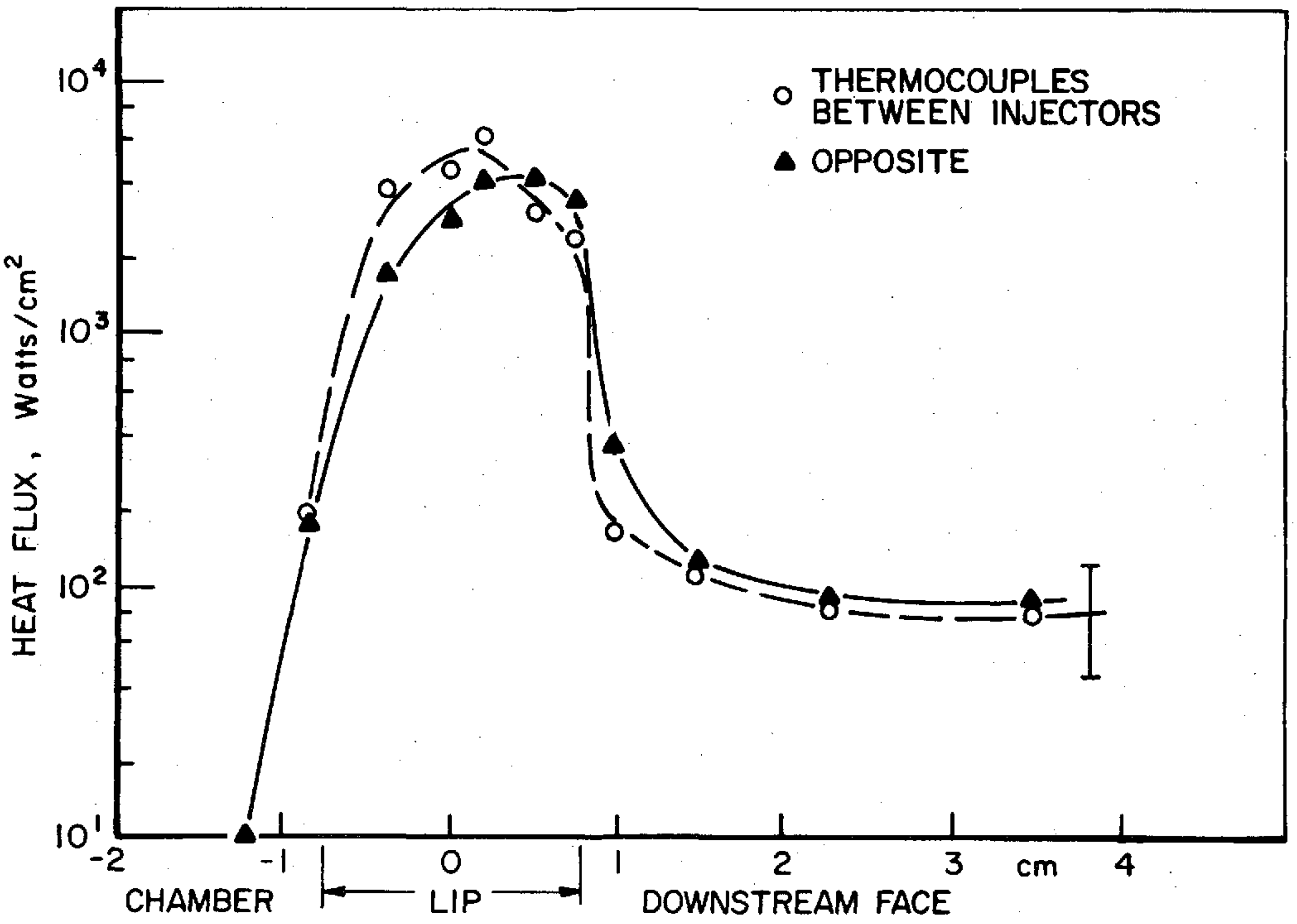

AZIMUTHAL VARIATION OF ANODE HEAT FLUX

16 kA, 6 g/sec

which appears is mild, with the heat flux values differing by less than 10% locally. The variation may be a result of nonuniformities seen in optical studies of the discharge, where the particle number density distribution appears to depend on gas injection geometry(24) and the variation decreases with decreased mass flow at the same 16 kA current. In any case, for the purpose of the measurement of anode power in the MPD arc, once the heat flux is integrated over the entire anode surface, the influence of the azimuthal variation is small, falls within the experimental error bar, and is entirely negligible.

3.4 Anode Power from Direct Measurements

Once the anode heat flux is determined, it is integrated over the entire anode surface to yield the anode power. The local anode heat flux q_a is assumed constant over each annular anode surface area A_m associated with each thermocouple: the area extends from points midway to adjacent thermocouples, except for thermocouples closest to insulating boundaries, whose areas extend to those boundaries. Therefore, the anode power is

$$P_A = \sum_{m=1}^{12} (q_a)_m A_m \qquad (3.3)$$

The calculation is insensitive to the exact selection of an area associated with each thermocouple, a consequence of the existence of large heat flux gradients only where the areas are small, i.e., at the lip. Furthermore, if the data are examined at any time from 15 to 400 msec following the 225 to 900 usec discharges, the value of the anode power does not change. This verifies that selection of 20 msec as a time to examine thermocouple data allows the local heat flux to be calculated, while the integral of the flux over the anode accurately represents anode power.

In the following, anode power is reported as a fraction of total arc power, P_A/P_T, to emphasize the relative importance of this component of the power allocation. For example, for the MPD arc operating with a total current of 16 kA and an injected argon mass flow of 24 g/sec, the anode power of 260 kW represents 20% of the 1.3 MW arc power. This implies that 80% of the power is allocated to other parts of the discharge.

If the current is held constant, anode power fraction peaks with mass flow. Figure 3.12 shows anode power fraction maxima occur as mass flow extends from 1 to 48 g/sec, while the current is fixed at 11, 16 or 22 kA. When current is 16 kA, for example, the anode power fraction for a 3 g/sec argon mass flow is 0.1. The fraction rises to a peak of about 0.24 to 16 g/sec and then drops again to nearly 0.1 as mass flow reaches a 48 g/sec level.

The peaking of anode power fraction occurs for all the currents studied, shifting to higher mass flow as the current level is raised. The search for a correlation factor has led to the consideration of $J^2/\dot{m}$, the ratio of the square of the current to the argon mass flow. This parameter has appeared in various other contexts in MPD arc studies in this and other laboratories. It has served to correlate arc geometries as well as phenomena such as the appearance of fluctuations in arc voltage(51), and the attainment of a maximum exhaust velocity with increasing current for a given propellant mass flow.(52) When the anode power fraction P_A/P_T is related to $J^2/\dot{m}$ (Fig. 3.13), the peaks of anode power fraction for all currents occur at $J^2/\dot{m}$ between 15 and 20 kA^2-sec/g. For values of $J^2/\dot{m}$ below this, arc operation is quasi-steady and relatively free of ablation; if $J^2/\dot{m}$ exceeds 16 kA^2-sec/g, the ablation can no longer be neglected. When $J^2/\dot{m}$ is larger than

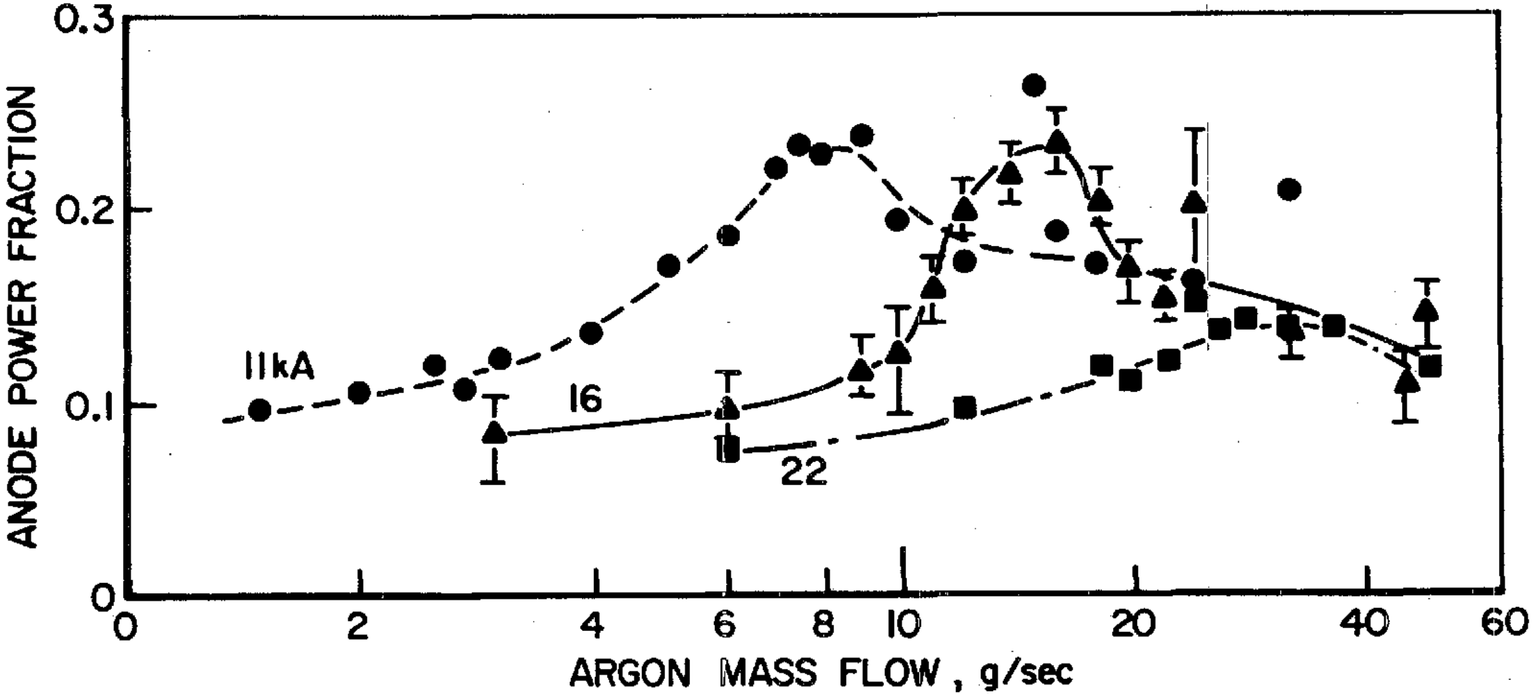

ANODE POWER FRACTION vs
ARGON MASS FLOW

FIGURE 3.12
AP25·5026

FIGURE 3.13
AP25.5025

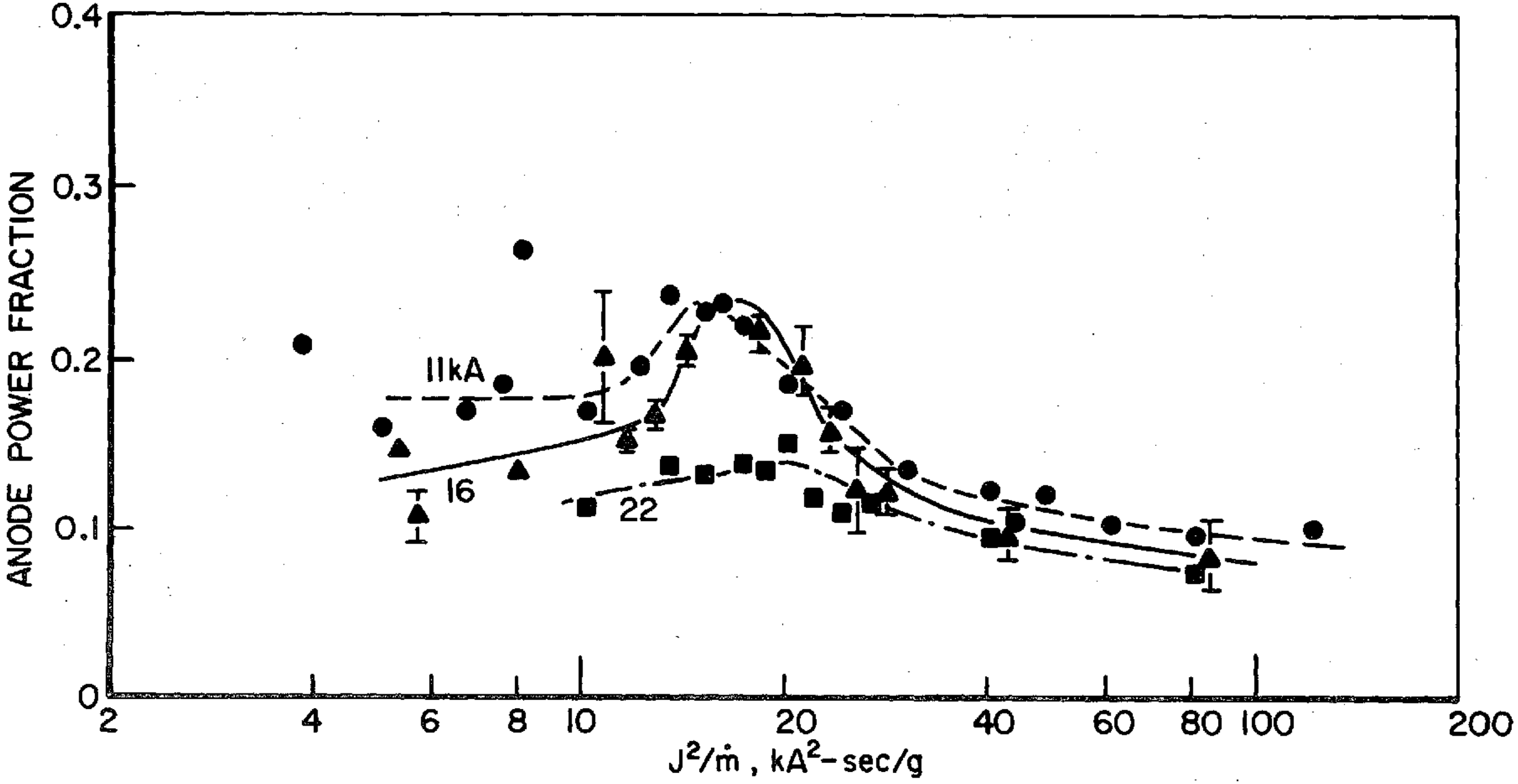

ANODE POWER FRACTION vs $J^2/\dot{m}$

16 kA^2-sec/g the argon mass flow does not represent the actual flow rate of particles through the accelerator. The particle number density increases as impurities appear as a result of the ablation of the Plexiglas insulator.(25) Thus, the appearance of low anode power fraction at high $J^2/\dot{m}$ may be artificial.

Since arc voltage depends on propellant mass flow, the same arc power can be achieved using a variety of arc currents. However, a single operating condition that corresponds to a value of arc power is defined if $J^2/\dot{m}$ is specified. On this basis, the dependence of anode power fraction on arc power can be represented uniquely. This dependence is illustrated in Fig. 3.14, where the anode power fraction P_A/P_T is shown over a range of arc power P_T from 255 kW, the level of the high-power steady arcjet,(9,30) to 16.5 MW, nearly two orders of magnitude. The data displayed cover a range of arc operating conditions from $J^2/\dot{m}$ = 5 and 10 kA^2-sec/g where little or no ablation of chamber insulators occurs, to $J^2/\dot{m}$ = 20, 40 and 80 kA^2-sec/g where the increasing ablation cannot be neglected. Illustrated is a decrease of anode power fraction as arc power increases, even at the highest $J^2/\dot{m}$ conditions. The results show the trend to decreasing anode power fraction whether propellant is supplied independently or, as in vacuum or ablation arcs,(53,54) the propellant is supplied by the ablation of a solid insulating material.

Figure 3.14 is a summary of the directly measured anode power fraction sought in this study. There is an overall drop in anode power fraction from 50% of the arc power at 200 kW to less than 10% as arc power is increased to nearly 20 MW. The important implication is that more power is available to the plasma, some portion of which will appear as thrust power, yielding more efficient thruster operation.

FIGURE 3-14
AP25-4956

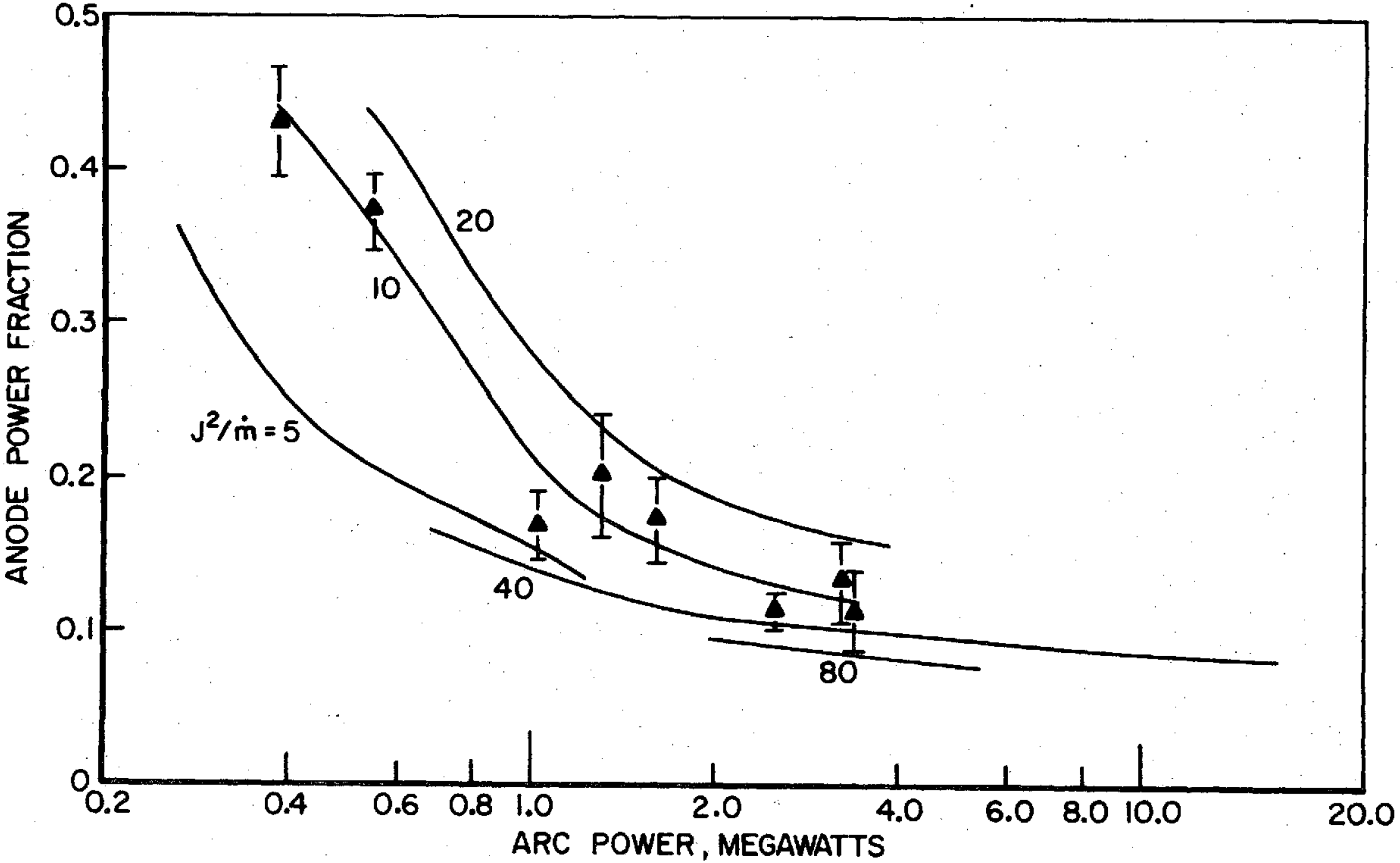

ANODE POWER FRACTION vs
TOTAL POWER

CHAPTER 4
ANODE HEAT FLUX MECHANISM

4.1 Introduction

One model commonly employed to describe anode heat flux in an arc discharge free of magnetic field presumes an electron energy balance over the anode sheath.(33,34,55) In this model, the local anode heat flux, q_a, is related to the flow of electrons of temperature T_e with a current density j_a through the anode fall voltage, V_a, to an absorbing anode of work function φ:

$$q_a = j_a\left(V_a + \frac{5}{2}\frac{kT_e}{e} + \varphi\right) + q_{conv} + q_{radn} \tag{4.1}$$

where k is Boltzmann's constant, e is the charge on an electron and q_{conv} and q_{radn} are the convective and radiative contributions. This model has been successfully applied to atmospheric and high pressure arcs where the anode is immersed in a dense plasma.(31,35) However, application of the model in this form to the MPD discharges under study here is questionable, in view of the much lower number densities and significant magnetic induction field which prevails. The effective energy exchange mean free paths in the MPD discharge, which are influenced by the magnetic field, are much larger than the anode sheath thickness. Consequently, while the electron temperature term is still valid and the work function still applies, the anode fall voltage no longer represents potential energy the electrons gain from the electric field and deliver to the anode as heat.

This chapter describes the determination of the properties of the plasma adjacent to the anode, and a modification of the anode heat flux theory to make it applicable to the MPD thruster. Contributions from each term in the model are then evaluated and the anode power is calculated. The results agree with the measurements reported in Chapter 3. Based on this agreement, the MPD anode heat flux model is used to explain the measured decrease of anode power fraction with increasing arc power.

4.2 Anode Current

The local anode current density is evaluated from experimental maps of the magnetic induction field in the discharge. The magnetic field is measured with a pair of induction coil probes.(56) Each probe has a coil of #38 ga (0.01 mm diam) enamel-insulated copper wire wound on a nylon form. Both coils are 1.5 mm long, but one has 120 turns with 1.5 mm i.d. and 3 mm o.d., while the other has 130 turns with 2 mm i.d. and 4 mm o.d. Their twisted leads are shielded with a copper braid sleeve and housed in a 4 mm o.d. x 10 cm long Pyrex tube holders. To allow the coils to probe the upstream side of the anode, the holders have right-angle bends 2 cm from the coil. The coils are potted in epoxy to protect them from the discharge and the tube ends are sealed with epoxy to preclude out-gassing. The shielded leads from each probe are passed through Tygon tubing to a feed-through at a side port of the vacuum tank and the end of the Tygon tube is vacuum sealed to the Pyrex holder. The coils are terminated with 11 msec passive integrators(46) at the input to Tektronix 555 oscilloscopes with Type 1A7A plug-in pre-amplifiers, which are used to monitor the output.

To calibrate the probes, a known magnetic induction field is created in the discharge chamber by replacing the thruster cathode with an aluminum post, which is connected to the anode by an aluminum plate. From the known geometry of this short circuit, the magnetic field is calculated for various discharge currents. When the probe output voltage is measured over a range of currents and probe locations, the calibration constant is established. The calibration constants for the 120 and 130 turn probes are 1.89 (10^{-5}) and 3.41 (10^{-5}) Webers/$(m^2$-volt), respectively. The uncertainty in the calibration, determined from scatter in the data, is less than 5%. This calibration is verified in the actual MPD discharge. The coil probes are tucked behind the anode near the chamber backplate, beside the insulating ring, so that all current flows downstream of the probe during a quasi-steady discharge. A further check on the calibration, made by locating each probe separately at the same place in the discharge chamber, shows equal magnetic field for the same current. The risetime of the signals from the magnetic probes are compared to the risetime of the Rogowski loop that surrounds the accelerator.(47) The response of 10 μsec which is measured assures that the probe signals accurately represent the changing magnetic field during the discharge.

A triple overlay of signals from the 120 turn probe, in a 16 kA total current discharge with 24 g/sec injected argon mass flow, is shown in Fig. 4.1. The coil is located 2 mm behind the anode, 1 mm radially inward from the lip. The signal rises at initiation of the discharge and is quasi-steady after less than 200 μsec. The quasi-steady period lasts about 650 μsec. At approximately 900 μsec, the discharge extinguishes. A baseline overshoot follows the discharge as a result of "passive integrator droop". In the figure, the integrated output is about 1300 μvolts at 400 μsec, the time when magnetic field data are usually recorded. This output corresponds to a magnetic induction field of about $4.5(10^{-2})$ Webers/m^2. The discharges are probed throughout a region from 2 cm from the anode, to within 2 mm from the anode surface, on a 1.5 mm by 1.5 mm grid.

FIGURE 4·1

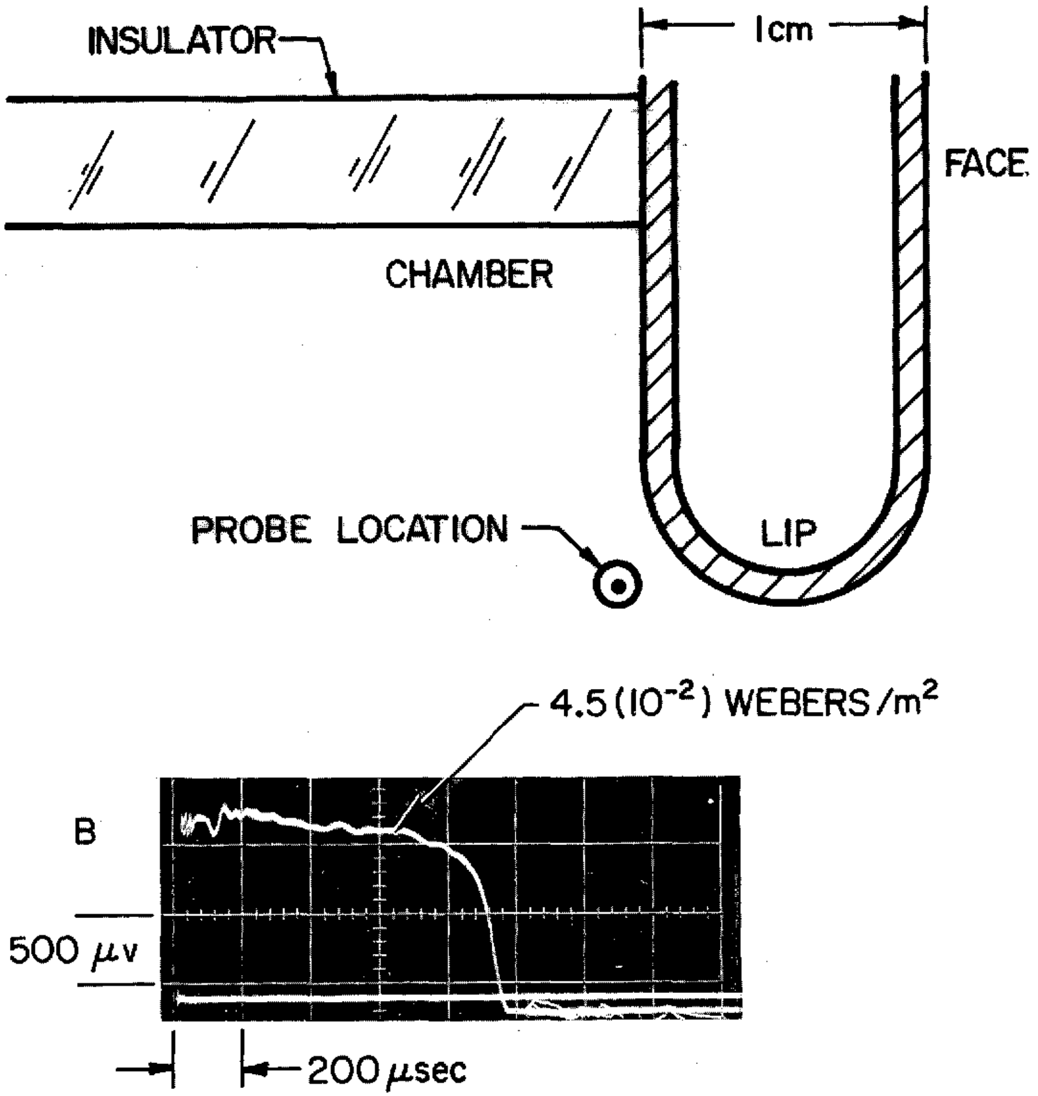

MAGNETIC FIELD PROBE RESPONSE
16 kA, 24 g/sec

For the essentially axisymmetric discharges studied, the magnitude of enclosed current at each probe location is derived from magnetic field data using Ampere's law.(57) Since the grid spacing is relatively fine, the results are linearly interpolated and enclosed current contours, i.e lines of equal current downstream, are drawn. An example for a 16 kA current with 24 g/sec mass flow is shown in Fig. 4.2. The contours, which also represent current streamlines, indicate that current bows downstream, and only 2 kA of the 16 kA total current enters the anode on the downstream face. The dashed lines are extrapolations of the measured current contours to the anode surface (the coil size would not permit probing more closely). The extrapolation may be misleading in the region behind the anode, near the chamber insulating ring, because the Hall parameter (the ratio of electron gyro frequency to Coulomb momentum-exchange collision frequency)(58) based on measurements described below, is greater than unity. The electrons may therefore turn downstream on their way to the anode.

The local anode current density is calculated from the enclosed current contours by dividing the current between contours with the anode area that absorbs it. The distribution of local anode current density for the 16 kA arc current and 24 g/sec argon mass flow is shown in Fig. 4.3. The abscissa represents a linearly rolled-out anode with midplane at 0.0 cm. Like the heat flux distribution, the current density peaks at the lip. It has a maximum there of 300 A/cm^2, dropping to 80 A/cm^2 in the discharge chamber and to 10 A/cm^2 on the anode face. A check on the integral of the derived current densities over the anode agrees with total arc current to within 10%.

When the local anode current density, j_a, is scaled with J/A the arc current divided by the anode conduction area

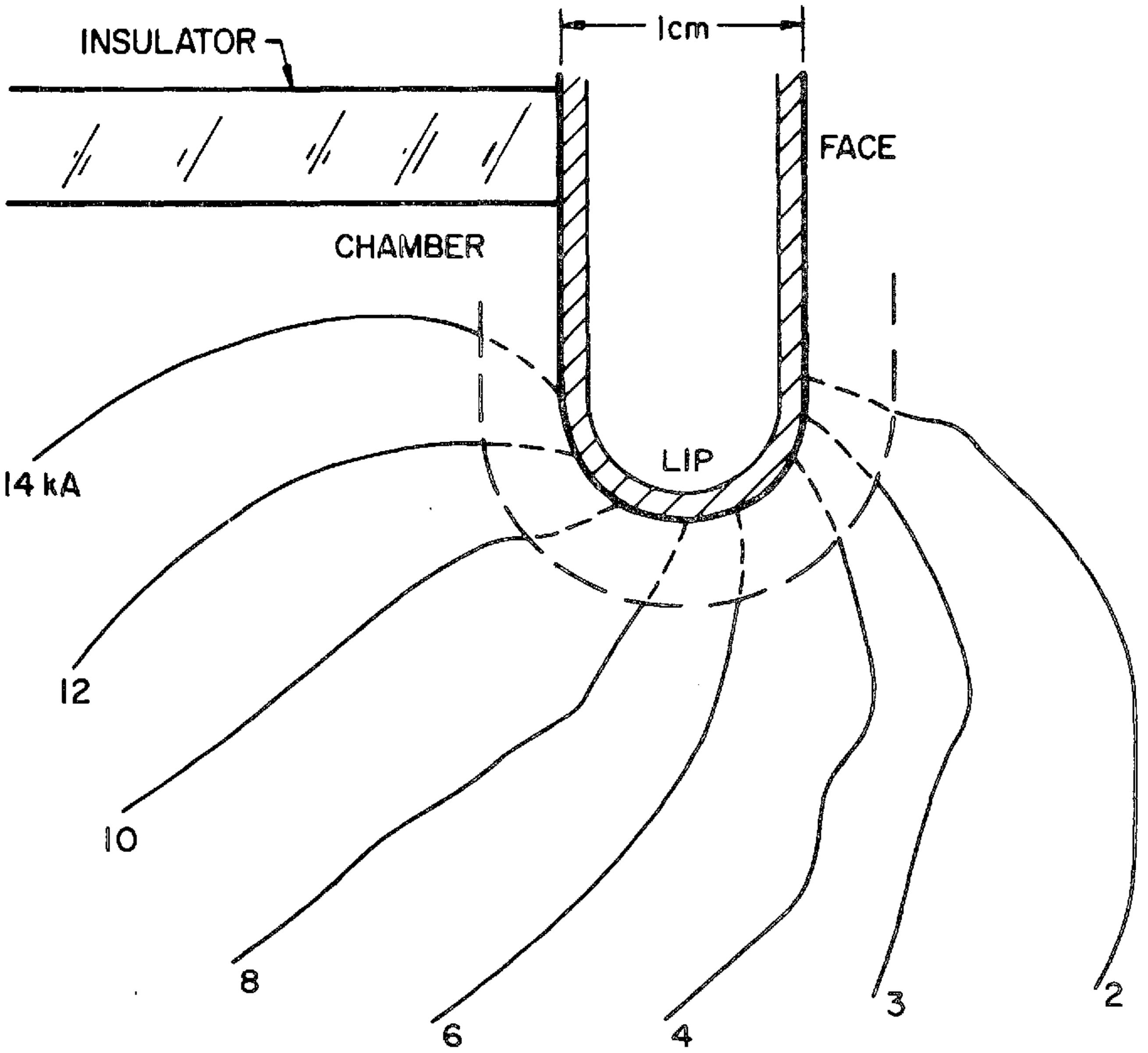

ENCLOSED CURRENT CONTOURS
16 kA , 24 g/sec

FIGURE 4.2
AP25·4957

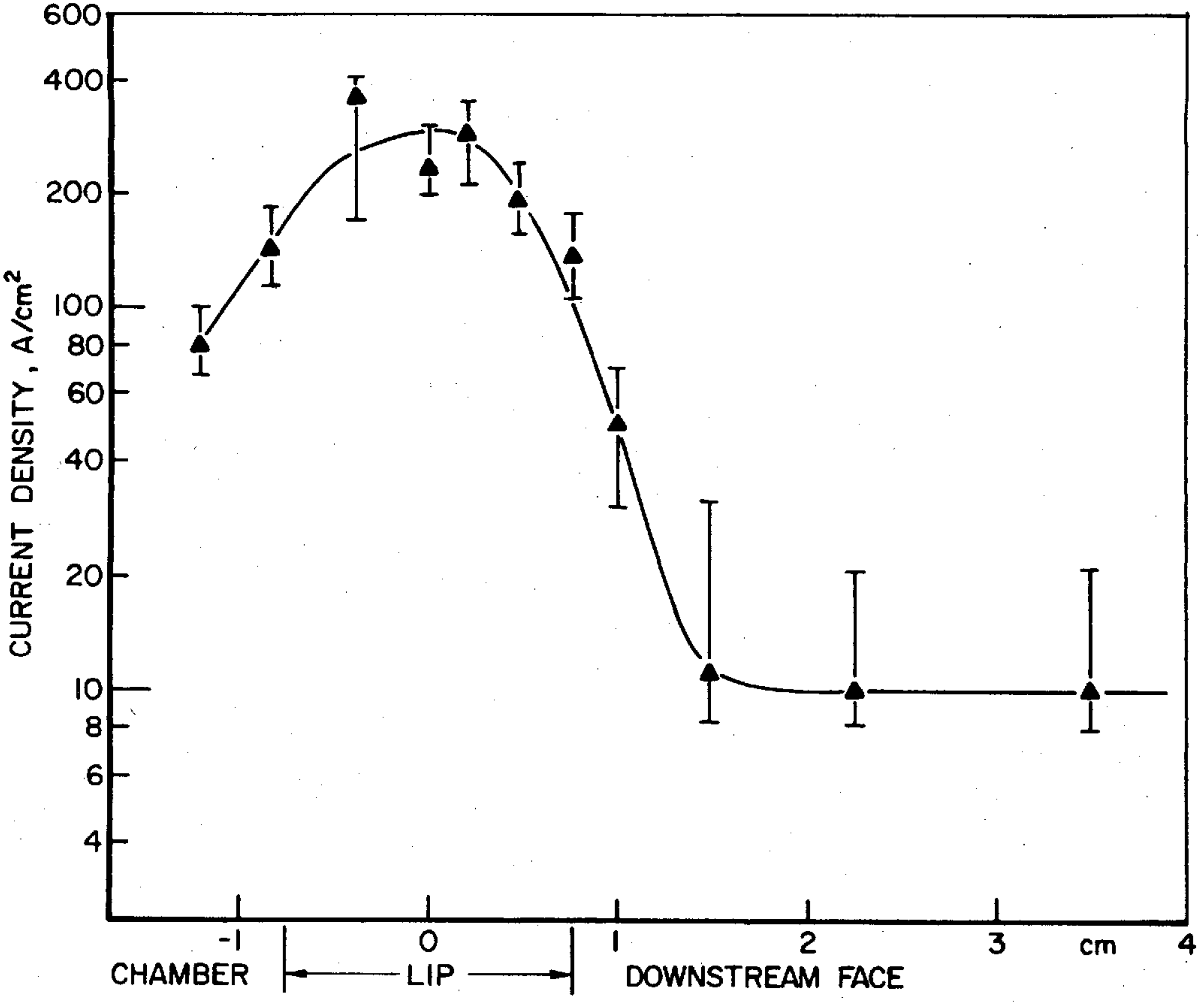

ANODE CURRENT DENSITY
16 kA, 24g/sec

FIGURE 4.3
AP25-4958

($\sim$260 cm^2) viz. $\hat{j}_a = j_a/(J/A)$, the change of current density distribution with arc current and mass flow can be seen. When the mass flow is held at 24 g/sec, the distribution (Fig. 4.4) remains almost unchanged for arc currents from 8 to 22 kA ($J^2/\dot{m}$ from 3 to 20 kA^2-sec/g). On the other hand, when mass flow is changed from 6 to 48 g/sec for 16 kA fixed current (Fig. 4.5), the portion of total current conducted over the anode face increases: For 20 kA^2-sec/g there is a threefold increase and for $J^2/\dot{m}$ 40 kA^2-sec/g, as much as half the current is being carried over the anode face. However, if the ratio $J^2/\dot{m} \cong 10$ kA^2-sec/g, approximately the same portion of current is carried at each anode location. This is shown in Fig. 4.6, where the current distribution is represented over the arc power range from 0.55 to 3.4 MW. For all the operating conditions studied, which fall in the current and mass flow range just described, the local anode current density is peaked at the lip.

4.3 Electron Temperature in the Anode Region

Electron temperature, T_e, is needed to evaluate electron enthalpy$^{(59)}$

$$h = \frac{5}{2}\frac{kT_e}{e} \tag{4.2}$$

as well as for the reduction of floating potential measurements to plasma potential. Both the enthalpy and the plasma potential are required to evaluate the anode heat flux.

The electron temperature is measured with double electrostatic probes. The probe electrodes are 0.7 cm long x 0.007 cm diam tungsten wires, mounted 1 mm apart in ceramic capillaries. The rest of the probe construction is similar to the magnetic probes described above.

FIGURE 4.4
AP25-5024

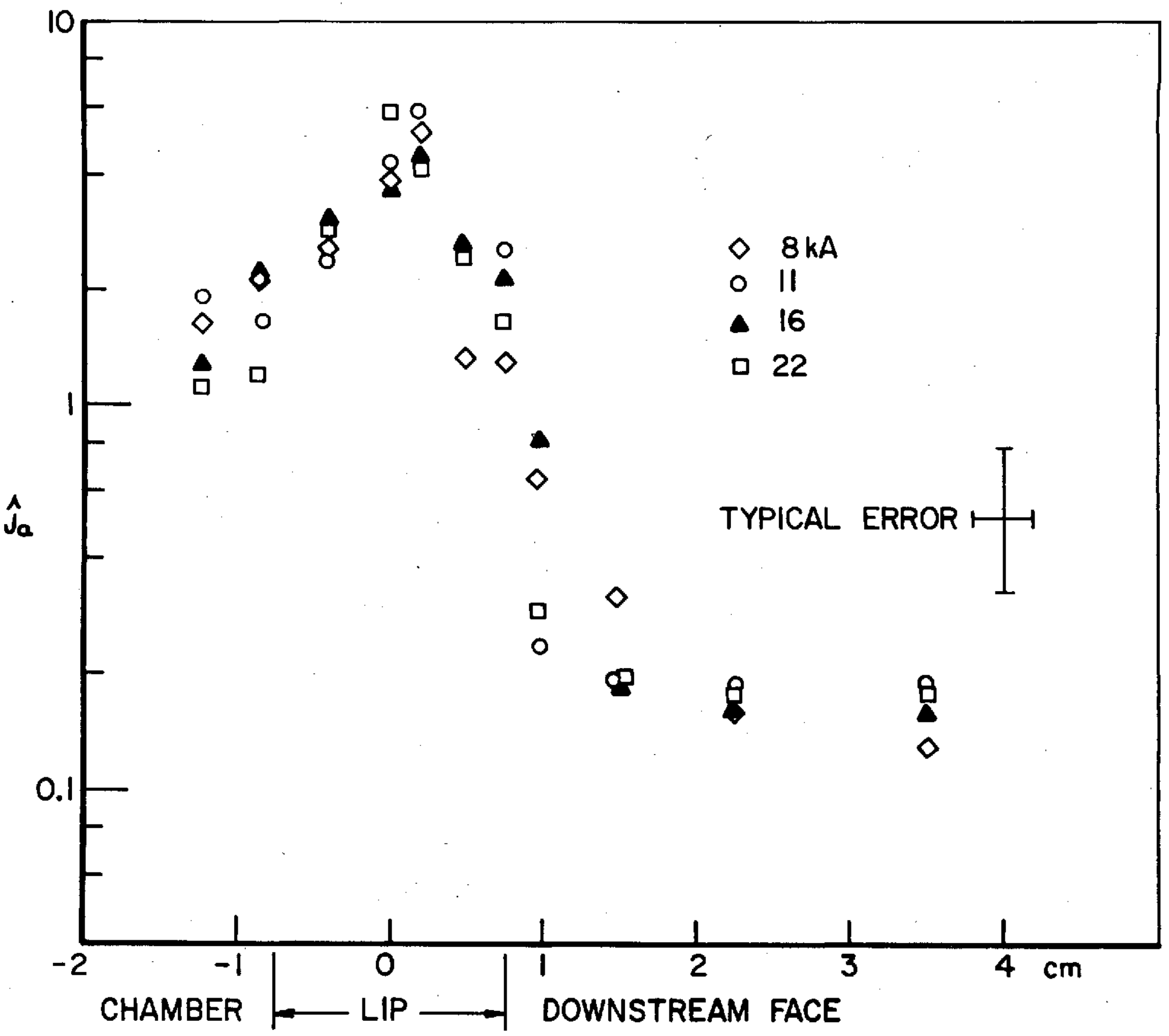

DIMENSIONLESS ANODE CURRENT DENSITY
24 g/sec

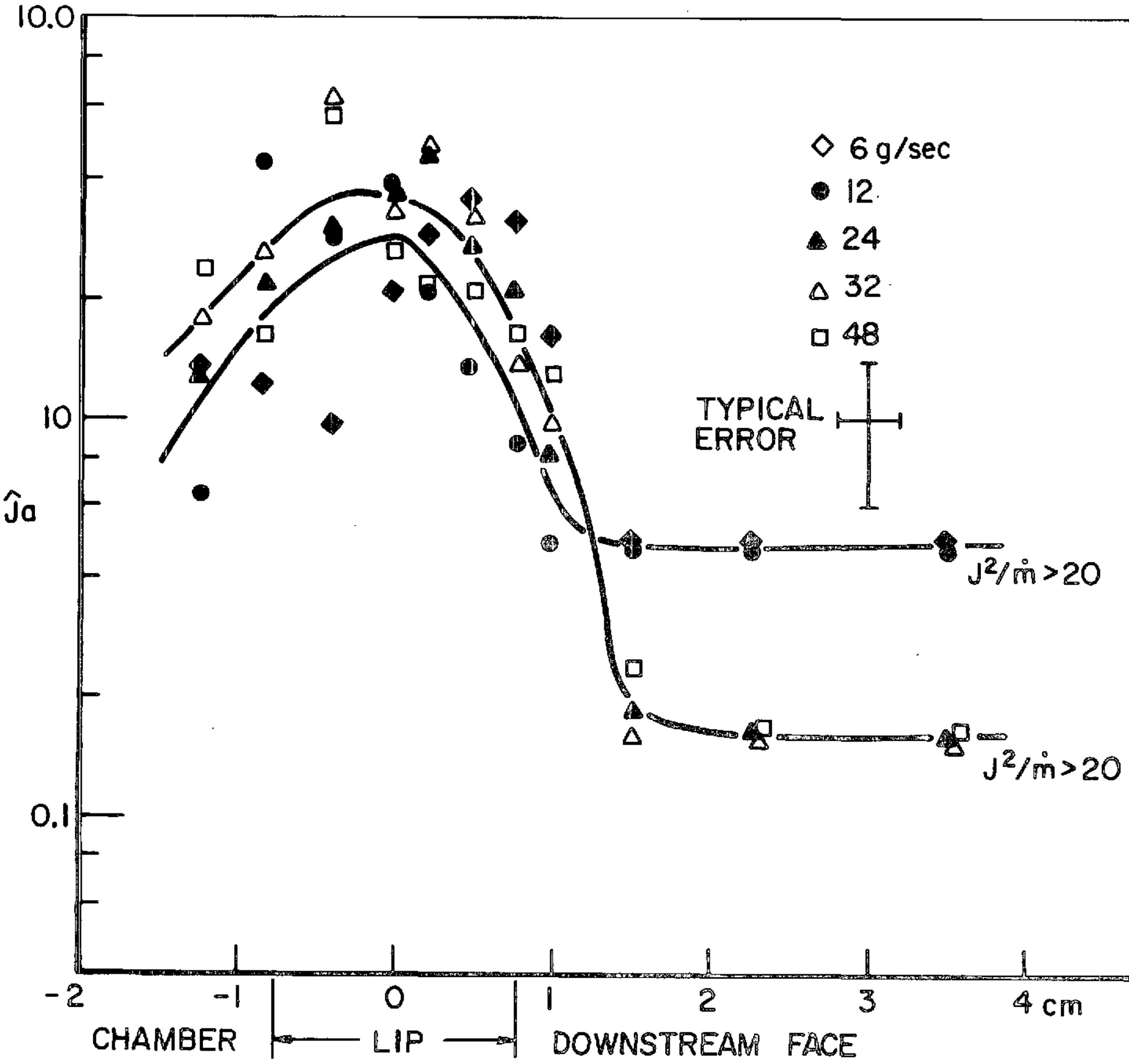

DIMENSIONLESS ANODE CURRENT DENSITY
16 kA

FIGURE 4.5
AP25·5023

FIGURE 4.6
AP25-5013

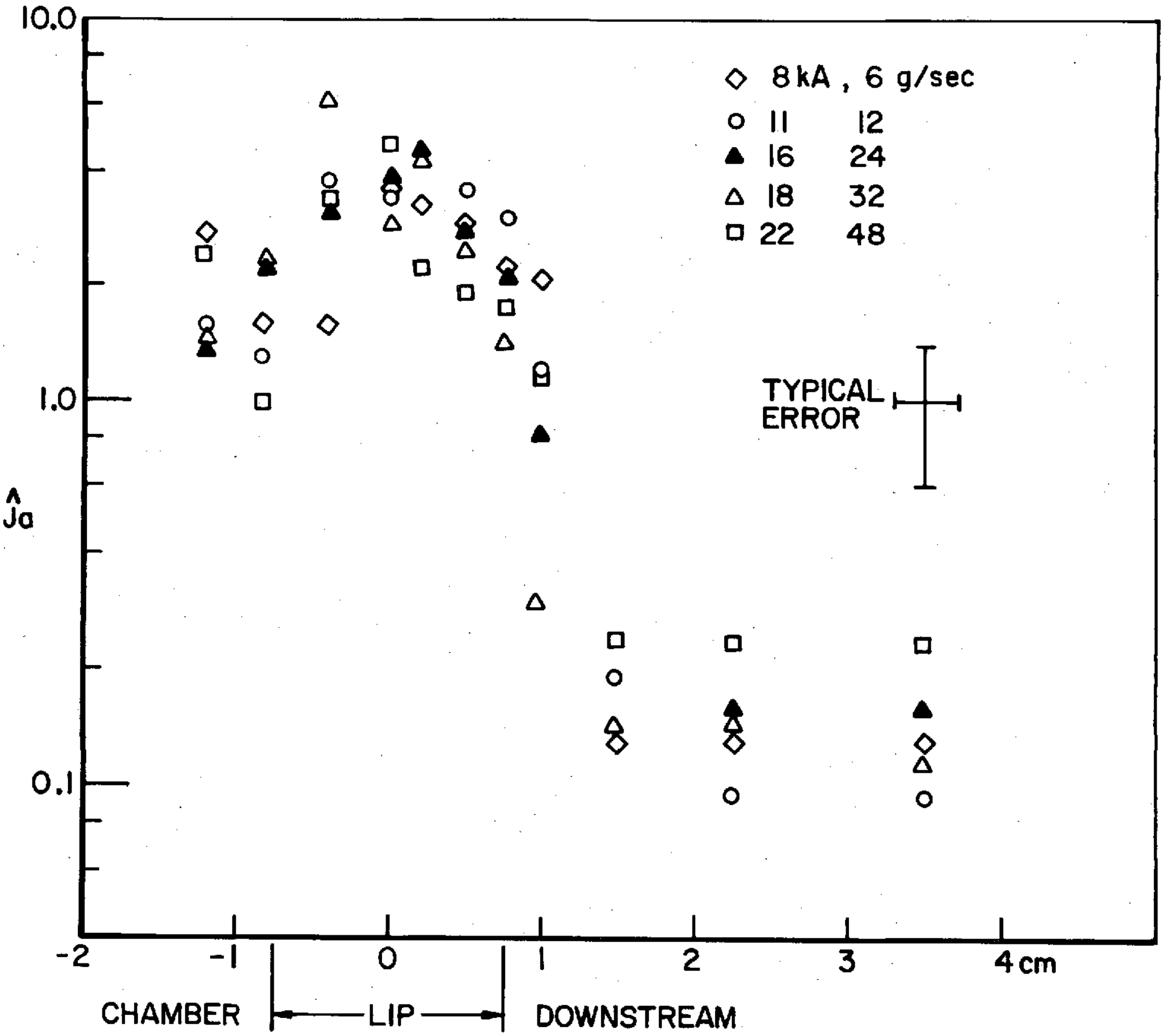

DIMENSIONLESS ANODE CURRENT DENSITY
$J^2/\dot{m} = 10\ kA^2\text{-}sec/g$

To assign a temperature to the electrons, their distribution is assumed to be Maxwellian. Therefore, from the double probe characteristic,

$$kT_e = e\frac{\hat{I}}{2(\Delta I/\Delta V)_o} \qquad (4.3)$$

where $\hat{I}$ is the saturation current to the probe extrapolated to the current axis at zero potential, and $(\Delta I/\Delta V)_o$ is the slope at the origin of the increasing portion of the characteristic.(60) Current flows between the electrodes when they are differentially biased by an electric potential. This probe current is monitored with a Tektronix P6042 current probe using a 555 oscilloscope with Type L plug-in pre-amplifier. Since the probe currents are very sensitive to the surface conditions of the electrodes, the electrodes are impact cleaned by ion bombardment after each discharge. This cleaning is performed by pre-filling the tank with argon gas to a pressure of about 100 mtorr and then biasing the probe electrodes negatively with respect to the anode. The uncertainty of the electron temperature measurement is estimated to be about 20%, since the reduction of the data suffers from small superimposed fluctuations on the probe current, which may be caused by ion density fluctuations in the plasma.

Electron temperatures measured at the anode lip are shown in Fig. 4.7. When argon mass flow $\dot{m}$ is 24 g/sec, the electron temperature increases from 0.7 to 2.0 eV, as arc current J is raised from 8 to 22 kA. There is a much weaker dependance on mass flow from 6 to 48 g/sec, when arc current is a constant 16 kA. However, for $J^2/\dot{m} \cong 10$ kA^2-sec/g, electron temperature is approximately constant at 1.2 eV, over nearly an order of magnitude of arc power from 0.55 to 3.4 MW. These observed electron temperatures can be represented by the following relations:

$$kT_e = 0.4\exp(0.066J), \qquad \dot{m} = 24 \text{ g/sec} \qquad (4.4a)$$

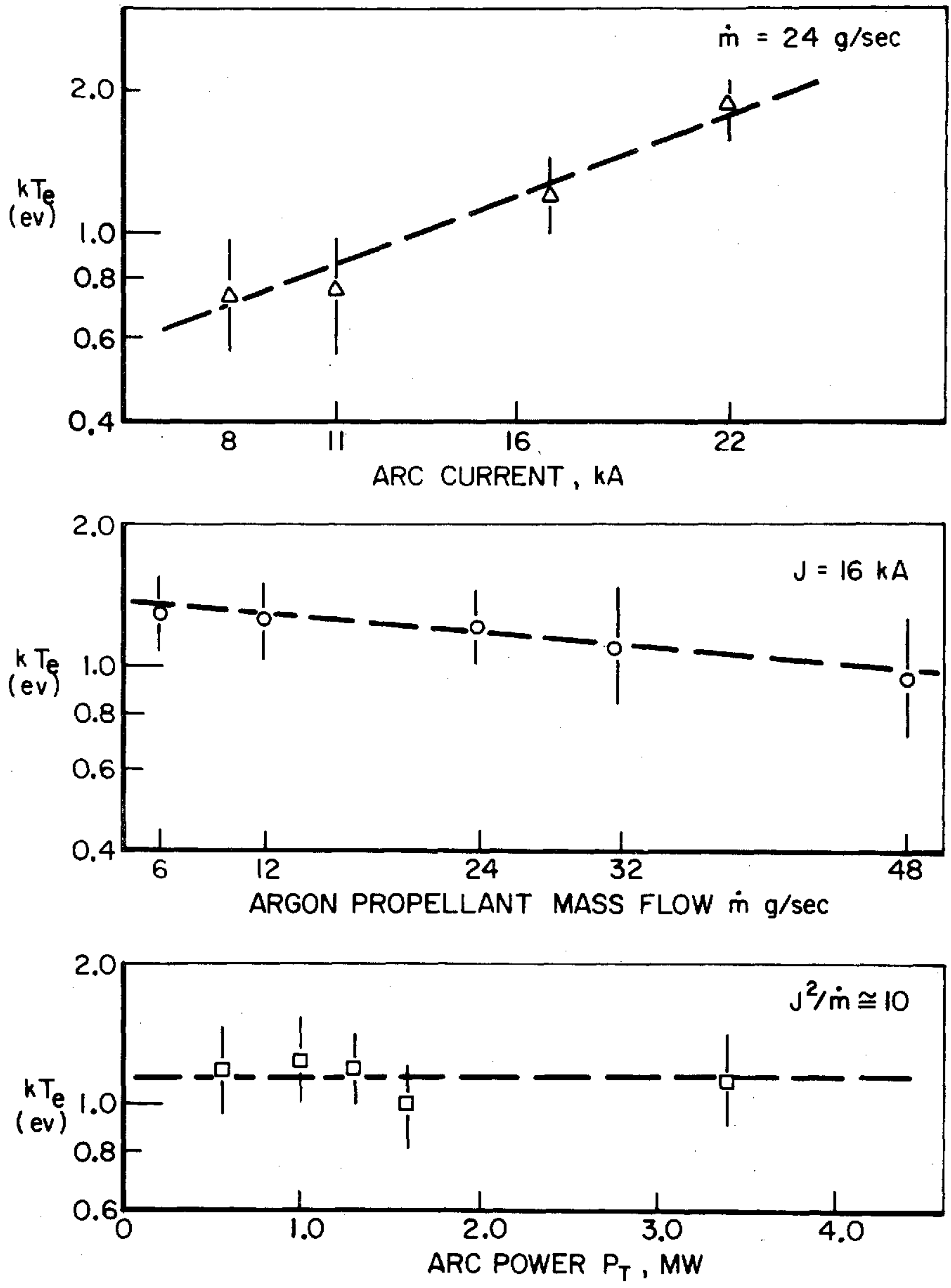

ELECTRON TEMPERATURE AT THE ANODE LIP

FIGURE 4·7
AP25-5022

$$kT_e \cong 1.4\exp[-8(10^{-3})\dot{m}], \qquad J = 16\,\mathrm{kA} \qquad (4.4b)$$

$$kT_e \cong 1.2, \qquad J^2/\dot{m} \cong 10\,\mathrm{kA}^2\text{-sec/g} \qquad (4.4c)$$

The results show that electron temperature, and hence electron enthalpy, depend on operating conditions, except for constant $J^2/\dot{m} \cong 10$ kA^2-sec/g.

For the arc currents and argon mass flows examined, the electron temperature is relatively uniform over the anode surface. The electron temperature 0.2 cm upstream of the face of the anode and 0.2 cm from the chamber insulator are approximately 20% lower than at the lip; and at a corresponding position on the downstream face it is about 10% lower than at the lip.

4.4 Anode Region Potential

Potentials in the vicinity of the anode are determined from Langmuir probe measurements of floating potential. The probe used has a single cylindrical tungsten electrode 0.1 cm long and 0.007 cm diam, radially oriented in the discharge chamber. Its construction is similar to the double probe used to measure electron temperature. To ensure that no net current is drawn, the Langmuir probe is terminated with a Tektronix P6013 voltage probe with 100 MΩ input impedance. Signals are recorded on Tektronix 555 oscilloscopes with Type G plug-in pre-amplifiers. An example of the floating potential in the anode midplane, 1 mm from the anode surface, for 16 kA x 24 g/sec arc operation, is illustrated in Fig. 4.8. Since the anode potential is ground, the probe response is negative. The signal, like the arc operating voltage included in the figure for comparison, rises in about 10 μsec and becomes quasi-steady in less than 200 μsec. Errors in the floating potential measurement are small since

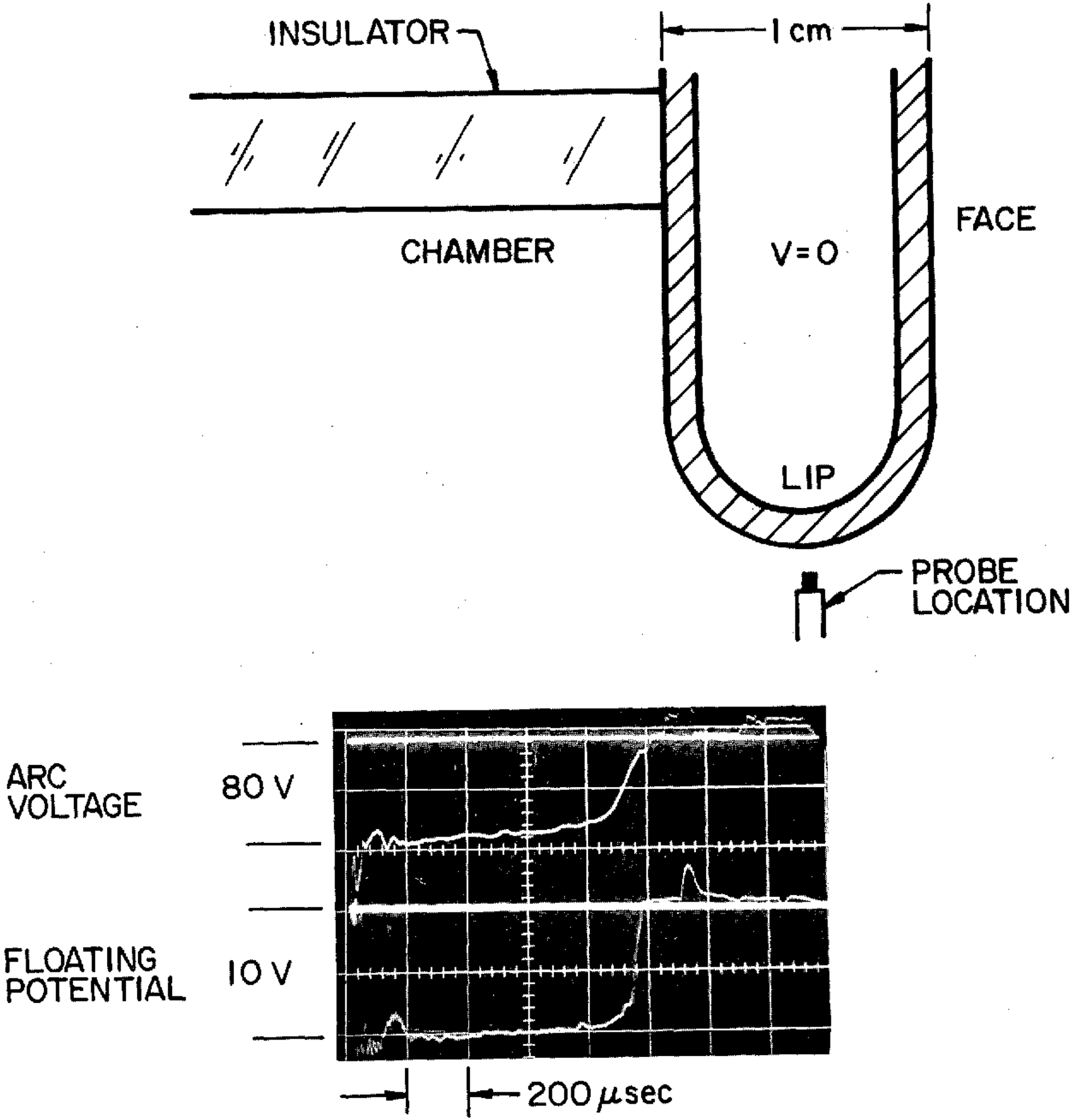

FIGURE 4.8

FLOATING POTENTIAL PROBE RESPONSE
16 kA, 24 g/sec

the data are reproducible, the probe location is well known and potential gradients are small except in the anode sheath.(61) Accuracy is further assured since the probe radius is much larger than the Debye length (which may be about $\lambda_D \cong 10^{-7}$m near the anode in the MPD discharges under study, where the electron number density is about 10^{21} m^{-3} and the electron temperature is about 1.2 eV).

The probe surveys the anode region over a 1.5 mm x 1.5 mm grid, to within 1 mm from the surface and lines of equal floating potential are mapped. An example is shown for the 16 kA x 24 g/sec case in Fig. 4.9, where the discharge chamber insulator and enclosed current contours are drawn for reference. The largest potential gradient appears at the anode surface and the floating equipotentials suggest a maximum in electric field slightly upstream of the anode midplane. The equipotentials in the lip region are almost normal to the enclosed current contours. This implies that momentum exchange collisions are more frequent than electron gyrations about magnetic field lines and therefore, current conduction near the lip is scalar.(62)

If floating potential is examined along current streamlines, as shown in Fig. 4.10 for the 16 kA x 24 g/sec discharge, and the measurements are extrapolated to the anode, the voltage intercept is approximately equal to the measured floating potential 1 mm from the surface. Therefore, anode adjacent floating potential is defined as the floating potential 1 mm from the anode. The distribution of anode adjacent floating potential over the anode surface, for 16 kA x 24 g/sec operation, is shown in Fig. 4.11. The value in the chamber is about 10 volts, dropping to nearly 8 volts in the anode midplane, and rising again to 13 volts along the downstream face.

Measured floating potentials, V_f , are not equal to the plasma potentials, V_p, at the probe location. The difference is a shift toward cathode potential because the electron

FIGURE 4·9
AP25·4960

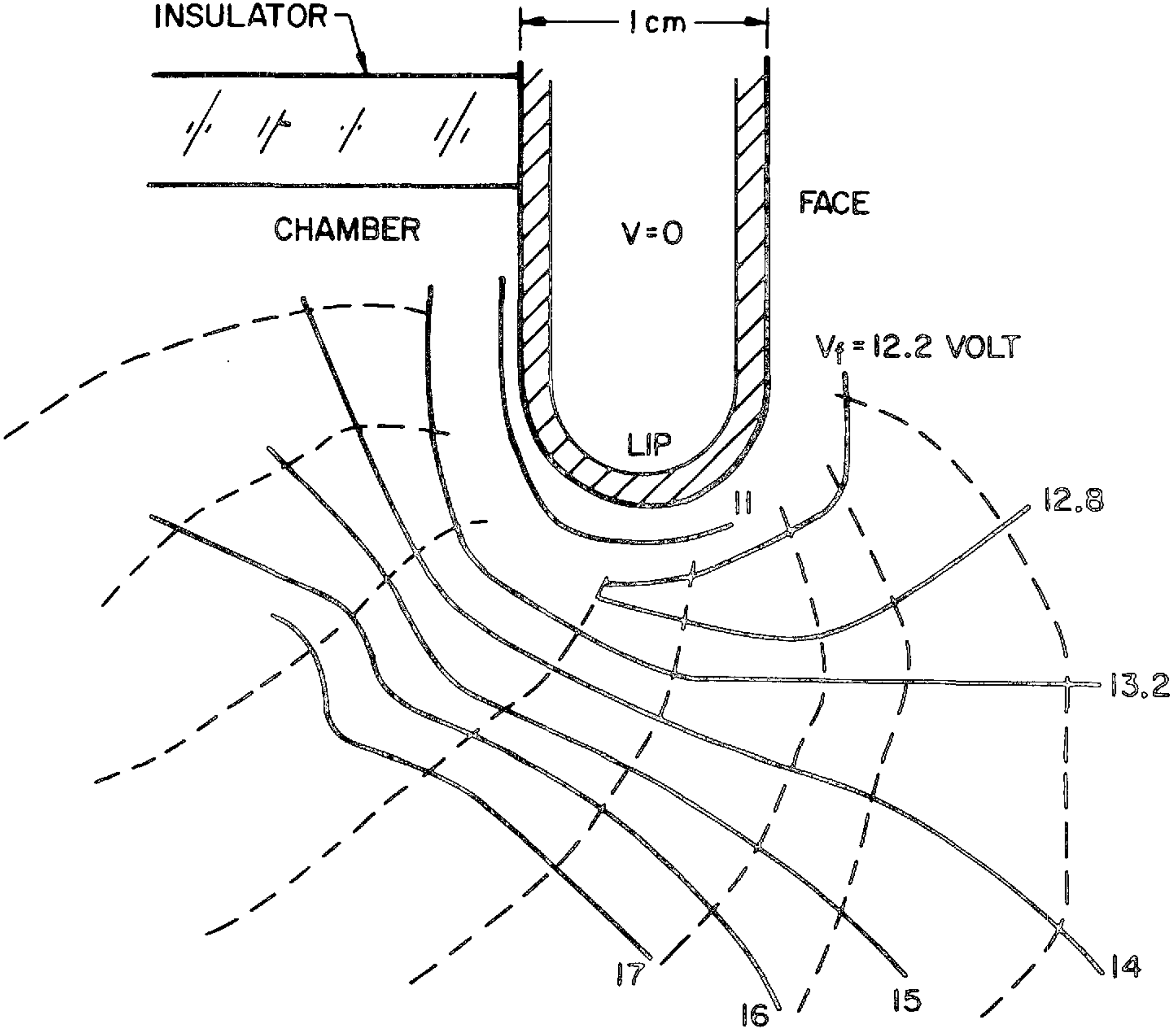

ANODE REGION FLOATING POTENTIAL
16 kA , 24 g/sec

FIGURE 4.10
AP25-5021

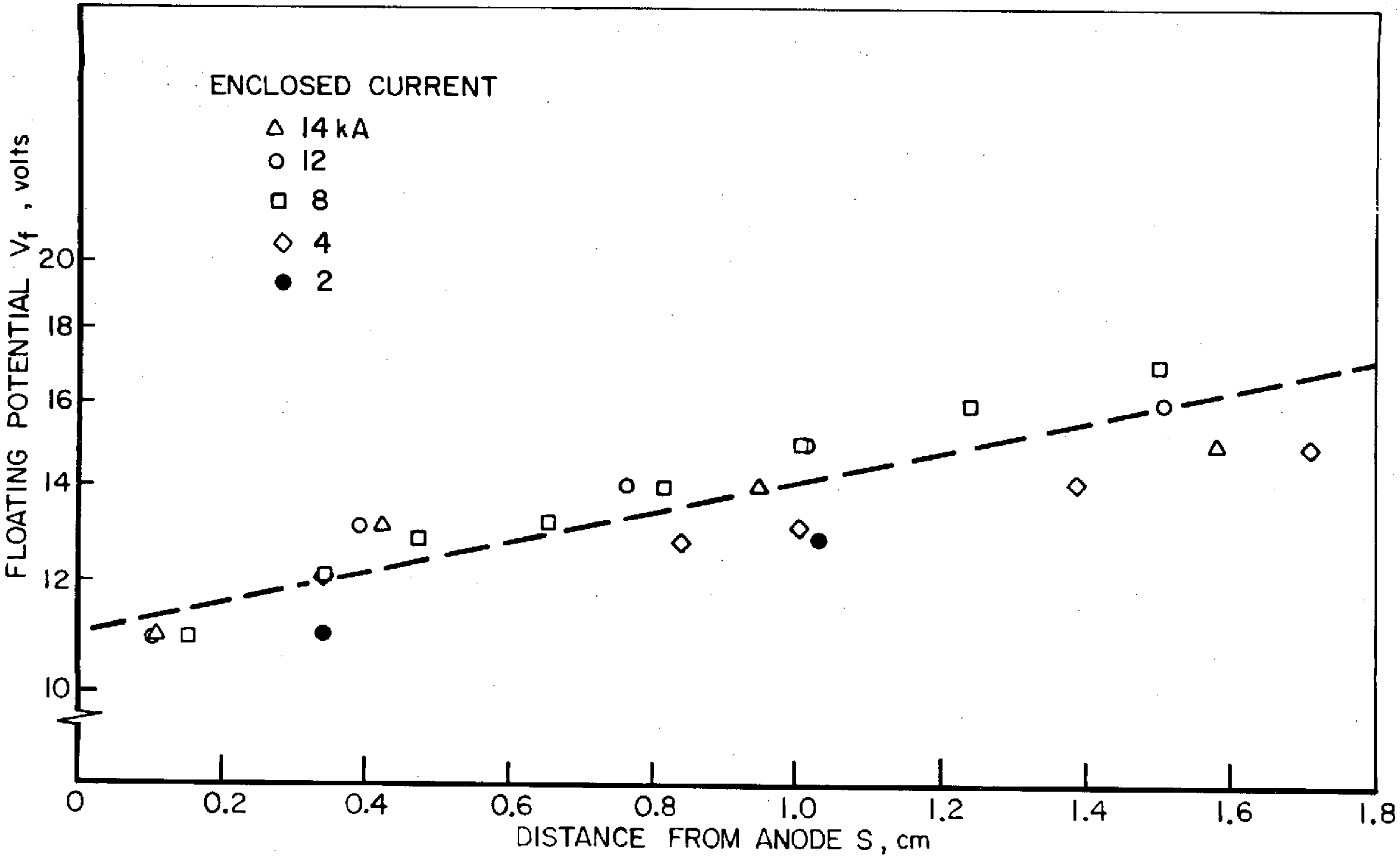

FLOATING POTENTIAL ALONG CURRENT STREAMLINES
16 kA, 24 g/sec

AP 25 4952 73

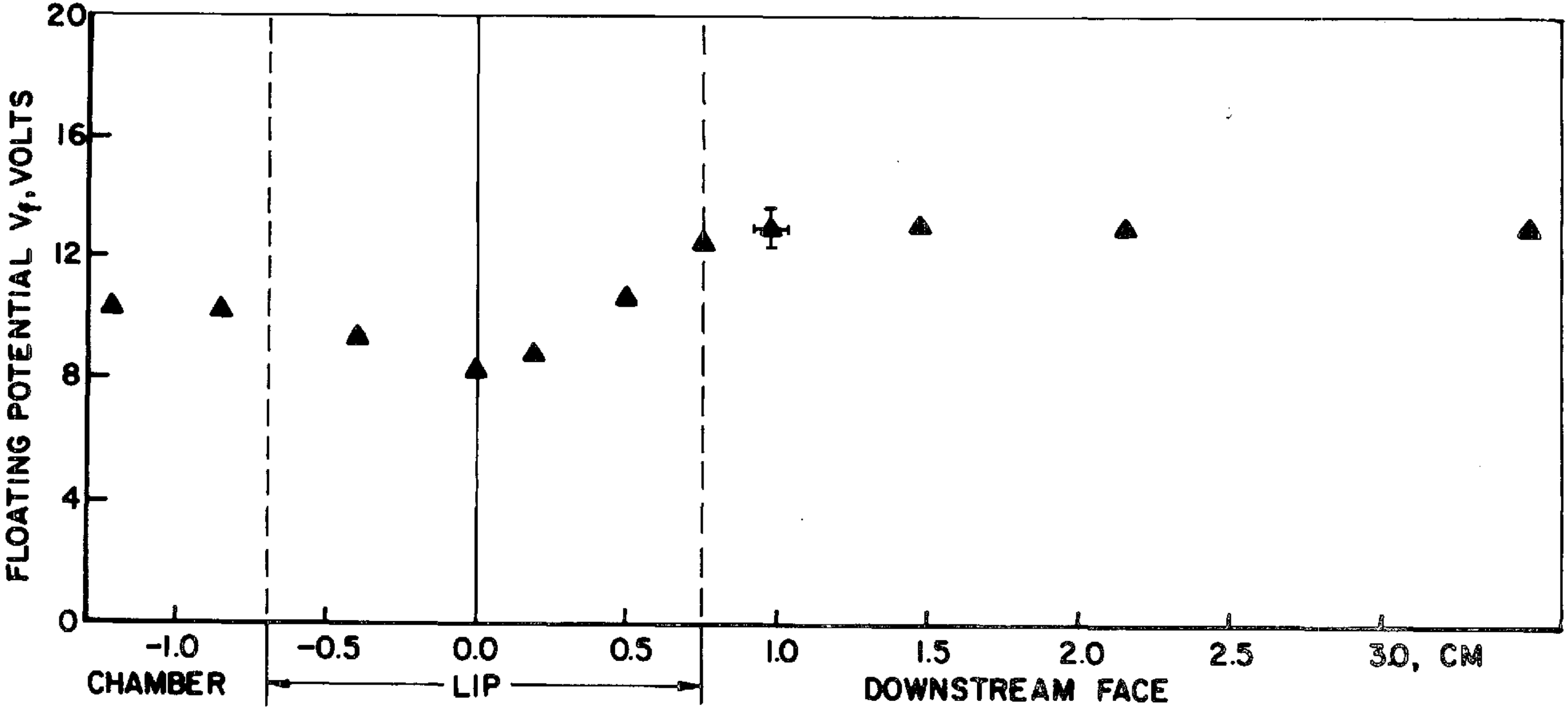

FIGURE 4·11
AP25·4952

ANODE ADJACENT FLOATING POTENTIAL
16 k A, 24 g/sec

thermal flux to the probe electrode surface is much higher than the total flux of the streaming ions. The calculation for the shift is shown in Appendix C. The correction term

$$\Delta V = V_p - V_f \tag{4.5}$$

for a plasma with a streaming ion velocity component u' normal to the probe axis, is written in dimensionless form as

$$-\frac{\Delta V}{\left(\frac{kT_e}{e}\right)} = \ln\left\{z\left(\frac{\pi m_e}{2kT_e}\right)^{1/2}\left[\sqrt{\frac{kT_e}{m_i}} + u'\right]\right\} \tag{4.6}$$

where m_i is the ion mass. The dimensionless correction $-\Delta V/(kT_e/e)$, shown in Fig. 4.12, is not a strong function of electron temperature T_e, but does vary with ion streaming velocity. The dashed line in the illustration represents the correction when ion streaming velocity is smaller than the Bohm speed.(63,64)

$$u_b = \frac{1}{2}\sqrt{kT_e/m_i} \tag{4.7}$$

The ion streaming velocity component normal to the axis of the probe electrode assumed for use in the correction is shown in Fig. 4.13. This figure is based on Doppler shift measurements of plasma velocity on the discharge centerline for a 16 kA x 6 g/sec discharge. At the anode midplane, along the axis of the accelerator, the ion streaming velocity is about 8700 m/sec downstream. However, the flow angle off-axis is 15° with respect to the center of the discharge, with a virtual origin at the cathode tip.(65) At the anode, the plasma is assumed to follow the contour of the surface, starting at nearly zero velocity but accelerating as it moves past the lip and over the anode face. Therefore, the velocity component perpendicular to the radially oriented probe electrode close to the anode starts at zero in the chamber, rises in the lip region and then drops to zero again on the face.

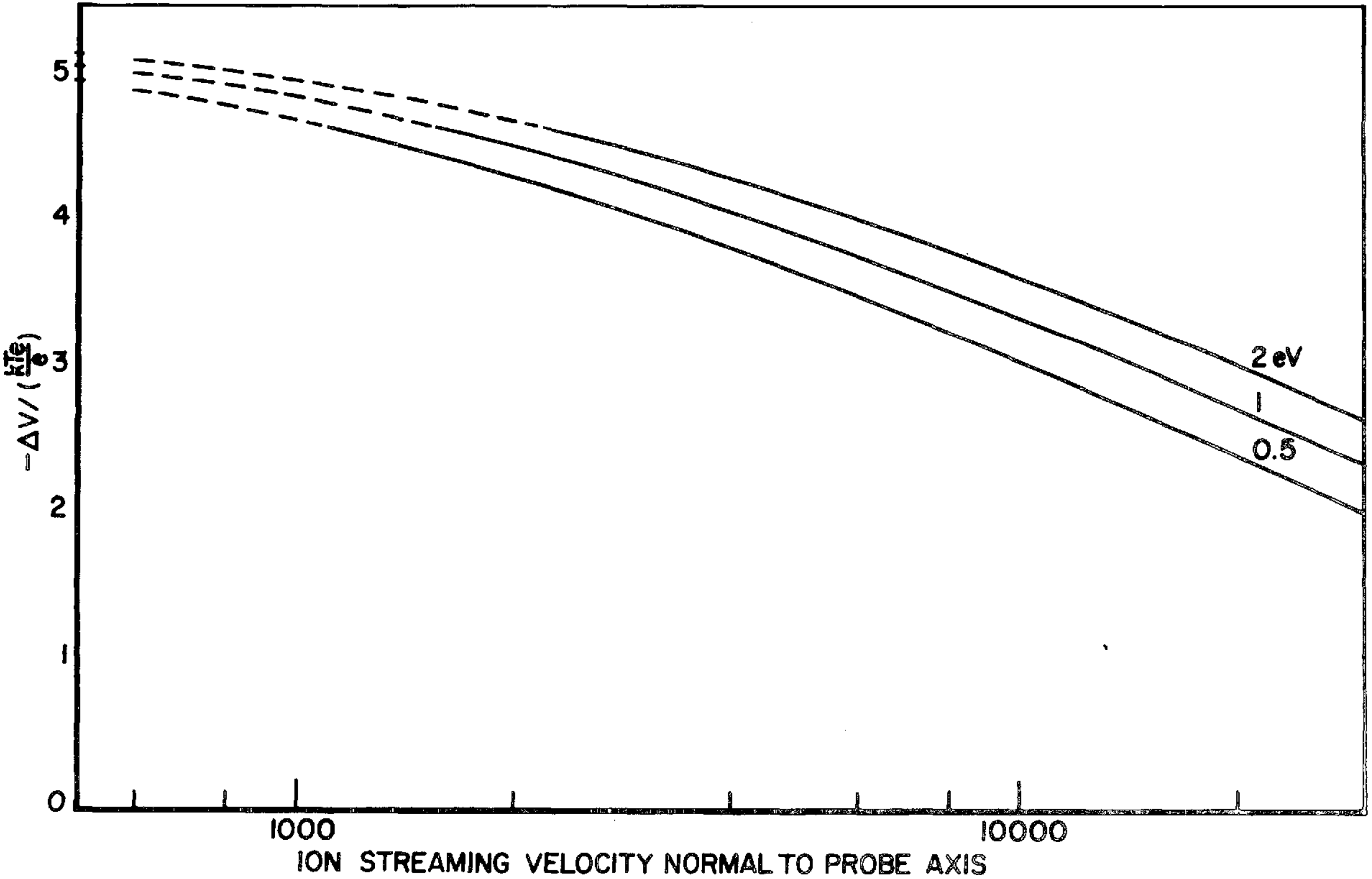

FLOATING POTENTIAL TO PLASMA POTENTIAL CORRECTION

FIGURE 4.12
AP 25-4956

Since thrust, the product of mass flow and exhaust velocity is a function of current only,(66,67) a four-fold increase in argon propellant mass flow rate, from 6 to 24 g/sec, may correspond to a four-fold decrease in ion streaming velocity, from 8700 to 2200 m/sec, at the same 16 kA current. Therefore, the dimensionless probe correction would change from about -3.5 to about -4.5 and the actual probe correction for a 1.2 eV electron temperature plasma would change from -4 to -5 volts. This compares to the 1 volt error due to electron temperature uncertainty. Similarly small changes in the correction might appear if the ion streaming velocity in the plasma were to be higher than 8700 m/sec.(25) Consequently, the velocity component normal to the probe axis, shown in Fig. 4.13, is used to calculate the floating to plasma potential correction for all operating conditions.

The anode fall voltage is derived from the measured anode-adjacent floating potential. Both profiles shown in Fig. 4.14 for 16 kA x 24 g/sec operation have the same shape along the anode. There is a dip in the lip region and the fall voltage is roughly half the floating potential. If a less peaked streaming velocity distribution had been assumed, then the depression in fall voltage at the anode midplane would be more acute. The error bar is large enough to allow the possibility that the anode fall voltage may even be uniform over the anode.

The anode fall voltages for other operating conditions are summarized in Fig. 4.15. For a low current of 8 kA and a mass flow of 24 g/sec (Fig. 4.15a), the fall voltage is nearly constant over the anode surface at 5 volts, except near the lip where it drops to 3 volts. As current is increased for the same mass flow, the voltage changes only

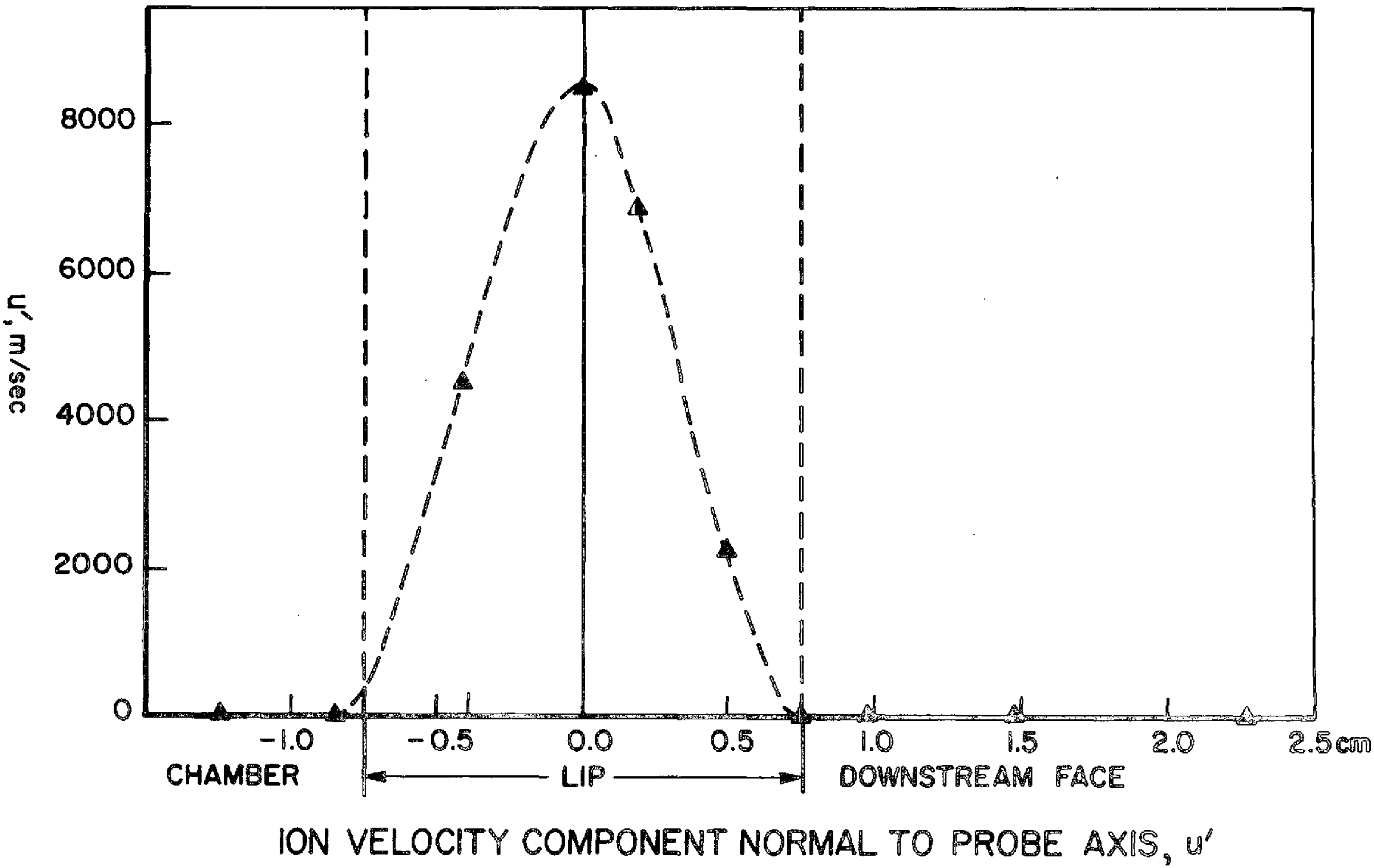

FIGURE 4.13
AP25·4956

AP 25 4953 73

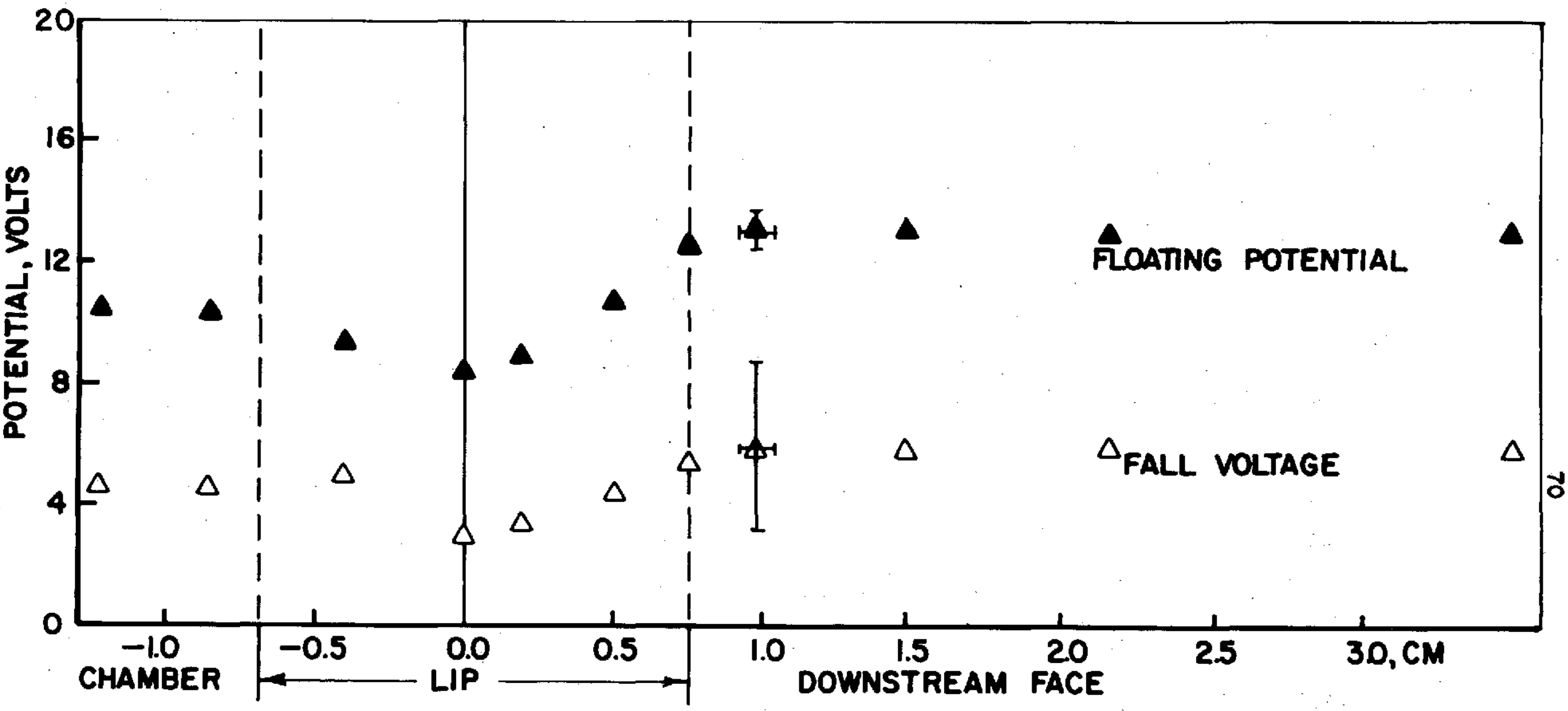

ANODE ADJACENT POTENTIALS
16 kA, 24g/sec

FIGURE 4.14
AP25-4953

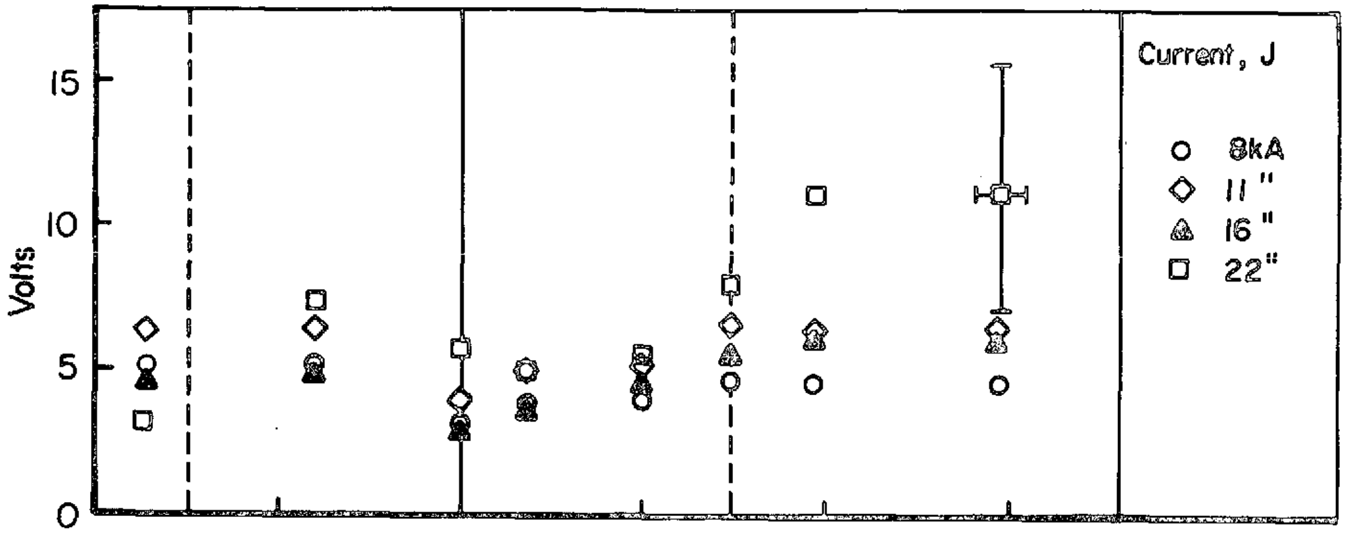

a) Mass Flow $\dot{m}$=24g/sec

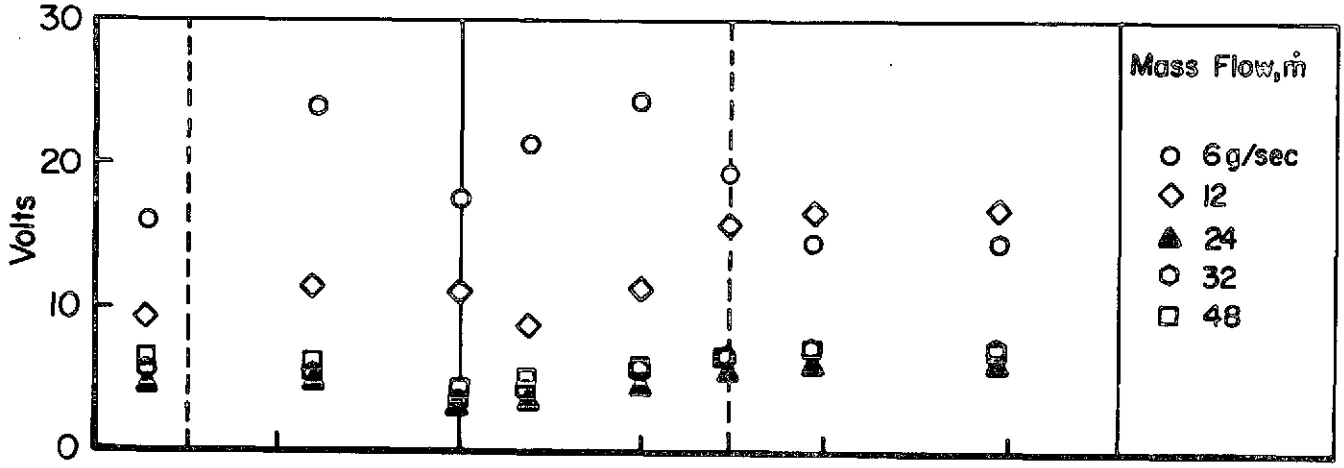

b) Arc Current J=16kA

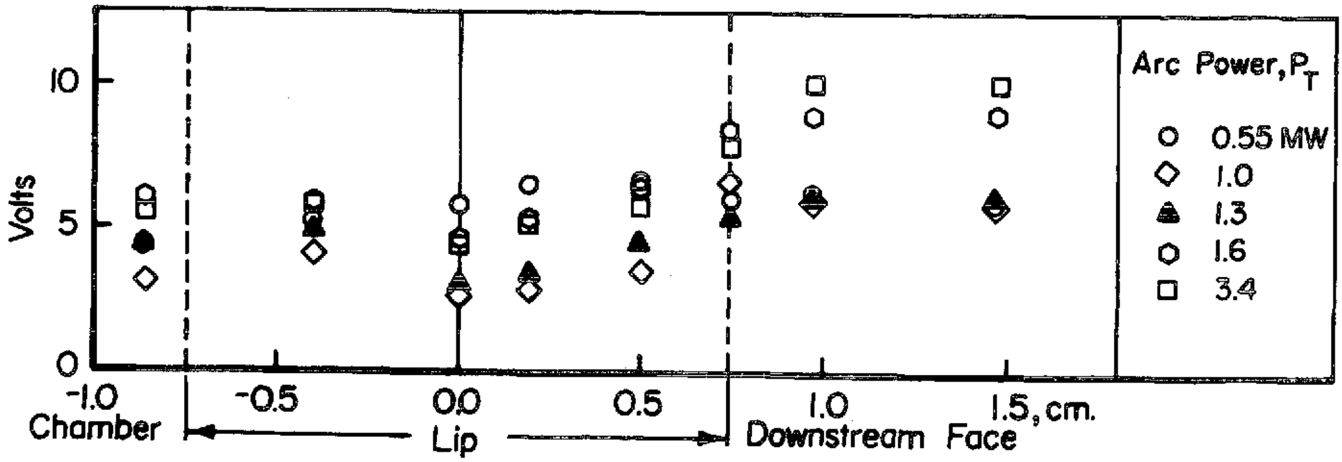

c) $J^2/\dot{m} \cong 10 kA^2$-sec/g

ANODE FALL VOLTAGE

FIGURE 4.15

AP25-5020

slightly, until the current is raised from 16 to 22 kA when the fall voltage over the anode face rises a factor of two, to 10 volts.

For constant current operation at 16 kA, Fig. 4.15b shows little difference in anode fall as mass flow changes from 48 to 24 g/sec. The anode fall voltage is about 5 volts in the chamber and on the face, but is depressed to about 3 volts on the lip. If argon mass flow is halved from 24 to 12 g/sec, the voltage doubles, while the shape of the distribution is maintained. Halving the mass flow again, to 6 g/sec, causes a maximum anode fall of about 22 volts in the vicinity of the anode midplane.

If $J^2/\dot{m}$ is held constant at about 10 kA^2-sec/g, over an order of magnitude arc power range from 0.55 to 3.4 MW (Fig. 4.15c), much less dramatic changes occur. For 0.55 MW operation (8 kA x 6 g/sec), the profile is flat at about 6 volts over the entire anode. Then, as arc power increases, a voltage dip in the anode midplane begins to develop. By 3.4 MW (22 kA x 48 g/sec), the anode fall voltage is 5 volts in the chamber, 4 volts at the lip and 10 volts on the anode face. Thus, if $J^2/\dot{m} \cong 10$ kA^2-sec/g, the anode fall voltage changes slightly in the chamber and rises less than a factor of two on the anode face, as the arc power increases.

Comparison of the anode fall voltage distribution with the current density over the anode (Fig. 4.4 to 4.6) shows anode fall minima at the highest current densities.

4.5 Convective and Radiative Heat Flux

The convective and radiative contributions to the anode heat flux, which appear in Eq. (4.1), are negligible compared to the directly measured anode heat flux. Estimates that use conservatively assumed values of the properties required are made for the 16 kA x 24 g/sec arc discharge.

The order of magnitude of the convective heat flux to the anode can be estimated if the anode is regarded as a nozzle wall. Start from a dimensionless boundary layer equation(68,69)

$$Nu = 0.026\, R_e^{0.8}\, P_r^{0.4} \tag{4.8}$$

where Nu, R_e and Pr are the Nusselt, Reynolds and Prandtl numbers respectively. This relation may be written

$$\frac{h_g D}{k_p} = 0.026 \left(\frac{D u \rho_p}{\mu}\right)^{0.8} \left(\frac{\mu C_p}{k_p}\right)^{0.4} \tag{4.9}$$

where h_g is the convective heat transfer coefficient

D is the scale length $\cong 10^{-2}$m, the anode width

u is the maximum assumed gas velocity $\cong$ 8700 m/sec

k_p is the plasma thermal conductivity $\cong$ 1.0 W/m-°K (70)

μ is the viscosity of argon $\cong 3(10^{-5})$kg/m-sec (70)

ρ_p is the plasma density $\cong n_i m_i$

c_p is the specific heat of argon at constant pressure $\cong$ 2000 J/kg-°K (71)

In the above, n_i and m_i are the argon ion number density and mass. Near the anode lip the number density is estimated as $n_i = 10^{21} m^{-3}$, so that

$$\rho_p = n_i m_i \cong 7(10^{-5})\ kg\text{-}m^{-3} \tag{4.10}$$

The fluid properties are assumed to have thermodynamic values corresponding to an argon plasma in equilibrium at the electron temperature of 1.2 eV (14,000 °K). Therefore,

$$R_e = \frac{D u \rho_p}{\mu} \cong 200 \tag{4.11a}$$

$$P_r = \frac{\mu C_p}{k_p} \cong 0.06 \qquad (4.11b)$$

and

$$N_u = 0.026(200)^{0.8}(0.06)^{0.4} \cong 0.6 \qquad (4.11c)$$

Thus,

$$h_g = \frac{k_p N_u}{D} \cong 6(10^{-3}),\ W/(cm^2 - {}^{o}K) \qquad (4.12)$$

Therefore, the estimate of convective heat flux to the anode lip is

$$q_{conv} = h_g T_e \cong 84\,W/cm^2 \qquad (4.13)$$

This is two orders-of-magnitude smaller than the directly measured heat flux to the lip and can be neglected. As a corollary, convective cooling due to pre- and post-discharge mass flow is also negligible.

Comparison of plasma radiation mechanisms (72) shows that the most intense radiative heating results from "free-free" Bremsstrahlung from the 1 cm long x 0.5 cm diameter plasma blob situated near the cathode tip. (26) Using the Spitzer formula (72)

$$\varepsilon_{ff} = 1.6(10^{-46})\, Z^3 n_i^2 T_e^{1/2},\quad W/cm^3 \qquad (4.14a)$$

For a singly ionized (Z=1) cathode plasma with an ion density of $n_i = 10^{23} m^{-3}$ and an assumed electron temperature of 2.4 eV (T_e = 28,000 ^{o}K), a factor of two larger than measured in the flow, the radiative emission is

$$\varepsilon_{ff} \cong 300\,W/cm^3 \qquad (4.14b)$$

Therefore, the radiation from the cylindrical plasma volume $V_{o\ell}$ at the cathode tip is

$$\mathcal{E} = \varepsilon_{ff} V_{o\ell} \cong 60 \text{ Watts} \tag{4.15}$$

If the radiation is assumed uniform over the 4π solid angle around the cathode tip, the radiative flux density at the anode orifice $(r = 5 \text{ cm})$ is

$$q_{radn} \cong 60/(4\pi r^2) \cong 0.2 \quad \text{W/cm}^2 \tag{4.16}$$

which is four orders-of-magnitude less than the maximum measured heat flux at the lip and two less than the lowest heat flux measured (in the discharge chamber).

Although the temperature rise of the inside surface of the shell anode has been measured, calculation of the heat the anode radiates into the plasma requires the temperature rise of the anode surface exposed to plasma. The plasma-exposed surface temperature is estimated by assuming that the anode is a slab $0 < y < \ell$ of zero initial temperature Θ, that there is a continuous uniform heat flux q over the surface at $y = \ell$ and there is no heat flow over the surface $y = 0$. This constitutes a standard heat flux problem.(73) The solution uses the dimensionless quantity

$$R = \frac{k_t \Theta}{q \ell} - \frac{\varkappa T}{\ell^2} \tag{4.17}$$

graphed in Fig. 4.16 as a function of the ratio y/ℓ, for different values of the parameter $\varkappa T/\ell^2$, where T is time.

For the aluminum anode, $\ell = 0.1$ cm is the shell thickness and the heat flux duration is $T = 1$ msec. The thermal conductivity is $k_p = 1.76$ W/cm-$^{\circ}$C and the thermal diffusivity is $\varkappa = 0.823$ cm^2/sec. Therefore,

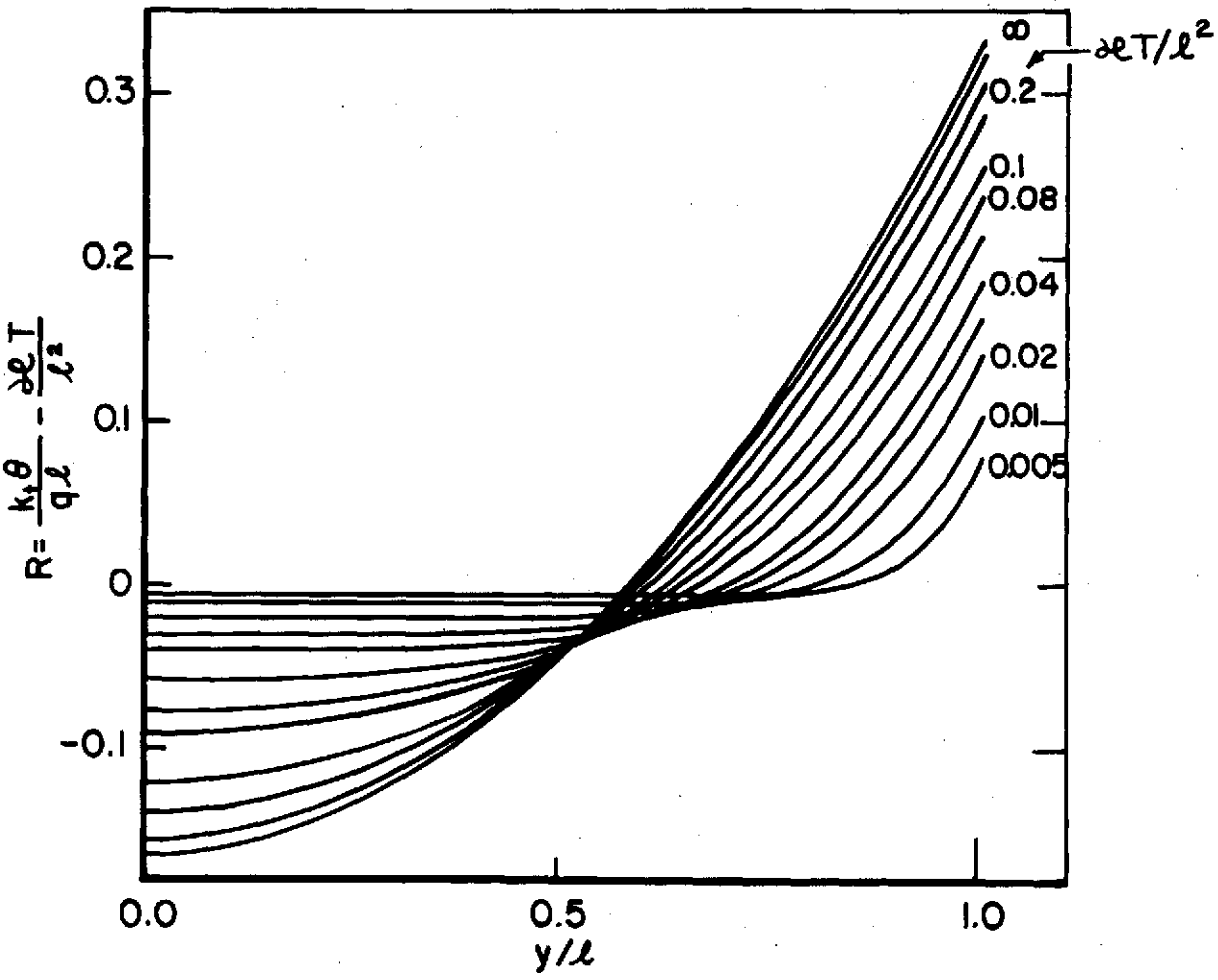

R vs y/ℓ

FIGURE 4.16
AP25·5015

$$\varkappa T/\ell^2 \cong 0.08 \qquad (4.18)$$

and the curve in Fig. 4.16, for $\varkappa T/\ell^2 = 0.08$ is selected. At $y/\ell = 1$, $R = 0.24$. Since the heat flux q_a at the anode lip is about 6000 W/cm^2, the surface temperature on the heated side of the slab at the end of the discharge period is increased by

$$\Theta = \left(R + \frac{\varkappa T}{\ell^2}\right)\frac{q_a \ell}{k_t} \cong 110\ {}^{\circ}C \qquad (4.19)$$

above ambient room temperature of about 20 °C. Thus, the maximum surface temperature of the anode at the end of the discharge is about 130 °C (which is much lower than the 660 °C melting point of aluminum(74)). Therefore, the maximum radiated heat flux from the anode surface at a temperature Θ is

$$q_{radn} = \sigma \Theta^4 \cong 0.2\ W/cm^2 \qquad (4.20)$$

where $\sigma = 5.7(10^{-12})\ W/cm^2\text{-}{}^{\circ}K$ is the Stefan-Boltzmann radiation constant. Therefore, radiation heat flux to and from the anode is negligible.

4.6 Anode Power in the MPD Arc

The local anode heat flux and power are calculated below from measured plasma properties. The calculation uses a model of the anode heat flux based on electron transport within the MPD arc.

As electrons progress through the MPD discharge, they acquire energy from the electric field. A portion of this energy is surrendered in collisions with the ions and neutrals in the plasma. Just before being absorbed by the anode, the electrons suffer a last energy exchange collision, after which any energy they gain from the electric field cannot be dissipated in the discharge. This energy is added to the electron enthalpy prevailing at the point of the last collision and is delivered to the anode as heat.

In the conventional high pressure or atmospheric arc discharges, where Eq. (4.1) applies, the distance between the position of the last energy exchange collision and the anode sheath is small enough and the prevailing electric field weak enough that the field-acquired energy electrons deliver to the anode closely corresponds to the anode fall voltage. However, in the MPD arc the distance between the anode sheath and the last energy exchange collision is sufficiently large, and the local electric field large enough that the anode fall is substantially augmented by a portion of the interelectrode field (the field between anode and cathode sheaths).

The last electron energy exchange collision before striking the anode is presumed to occur when the distance measured along current streamlines between energy exchange collisions λ equals the distance s along a current streamline to the anode surface:[1] viz.

$$\lambda = s \tag{4.21}$$

This energy exchange displacement, λ, is derived for the MPD arc in Appendix B-1. The displacement is a linear function of the electric field and the energy exchange mean free time: It increases if potential gradient increases and increases as the energy exchange cross section decreases. The influence of magnetic field appears in the Hall parameter(58): A large

---

[1] It must be acknowledged that this is an approximation to the actual energy exchange displacement which would vary along current streamlines depending on plasma properties. Therefore λ should ideally be calculated as an integral of differential energy exchange displacements along the current streamline. The data, however, does not warrant the more accurate computation.

Hall parameter indicates increased electron residence on the azimuthal magnetic field lines and therefore a decreasing net displacement. The potential difference V_s between $s = \lambda$ and the anode surface represents field energy delivered to the anode as heat. Thus, the anode heat flux model becomes

$$q_a = j_a \left(V_s + \frac{5}{2} \frac{kT_e}{e} + \varphi \right) \tag{4.22}$$

where convective and radiative contributions have been omitted. In the MPD arc, the energy exchange process is dominated by elastic energy exchange collisions between electrons and ions (Appendix B-II). The evaluation of the energy exchange displacement requires electron number densities as well as electron temperature and electric and magnetic fields determined from probing the plasma.

The radial electron density profiles used were determined previously from a reduction of the spatially unresolved profiles of the Stark-broadened H_α and H_β lines.(75) The profiles, shown in Fig. 4.17 for the 16 kA x 24 g/sec discharge, peak at about $10^{22} m^{-3}$ along the discharge chamber axis, but drop an order of magnitude at the anode orifice radius (5 cm).

The measured plasma properties are used to determine the dimensionless displacement

$$\lambda^* \equiv \frac{\lambda}{S} \tag{4.23}$$

shown in Fig. 4.18 for the 16 kA x 24 g/sec discharge, as a function of the dimensionless streamline co-ordinate

$$S^* \equiv \frac{S}{L} \tag{4.24}$$

where L is the streamline length from the anode to the cathode. The error bar in Fig. 4.18 represents uncertainties in the electron density by 100%, electron temperature by 20%, and

FIGURE 4.17
AP25-4951

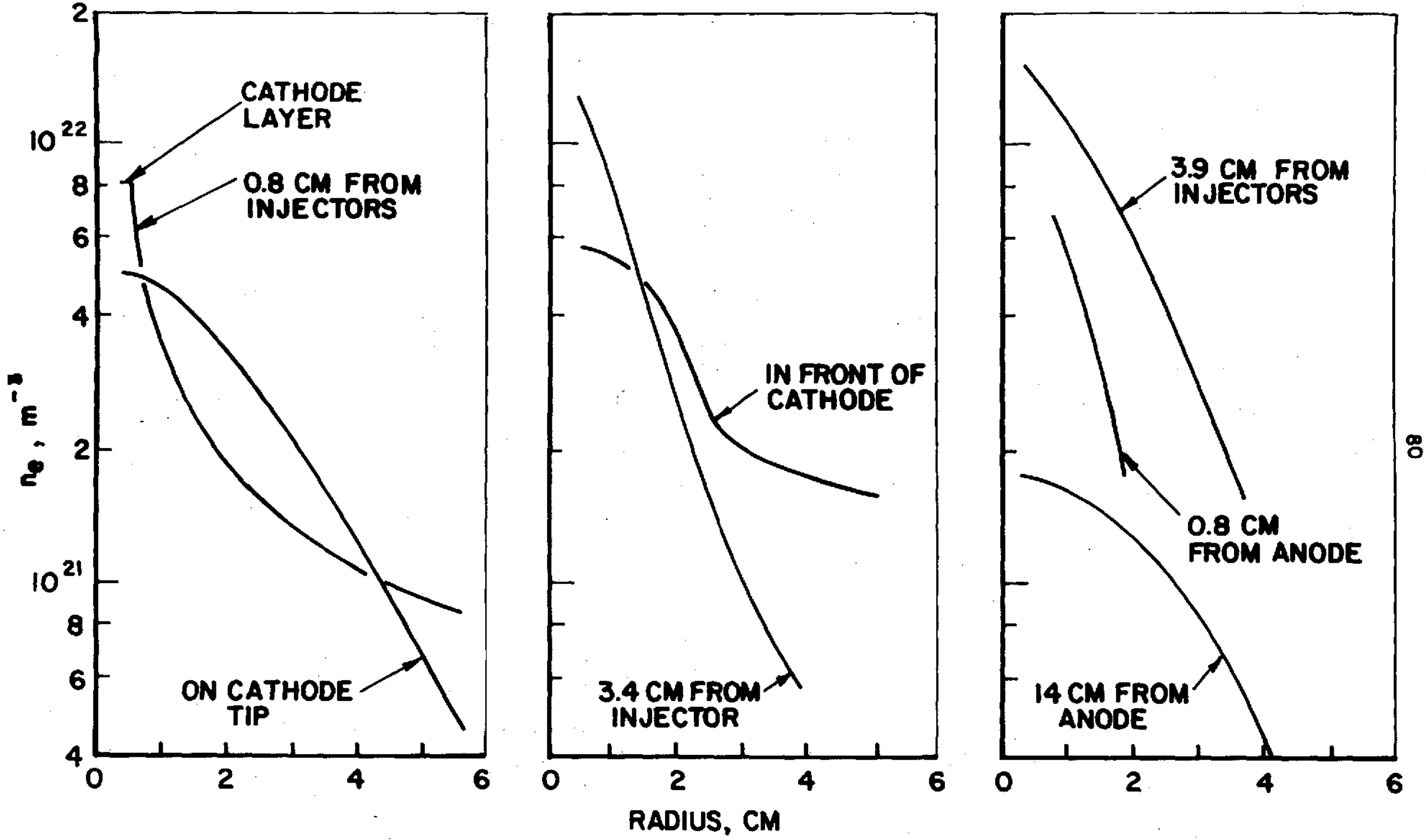

ELECTRON DENSITY PROFILES
16 kA, 24 g/sec

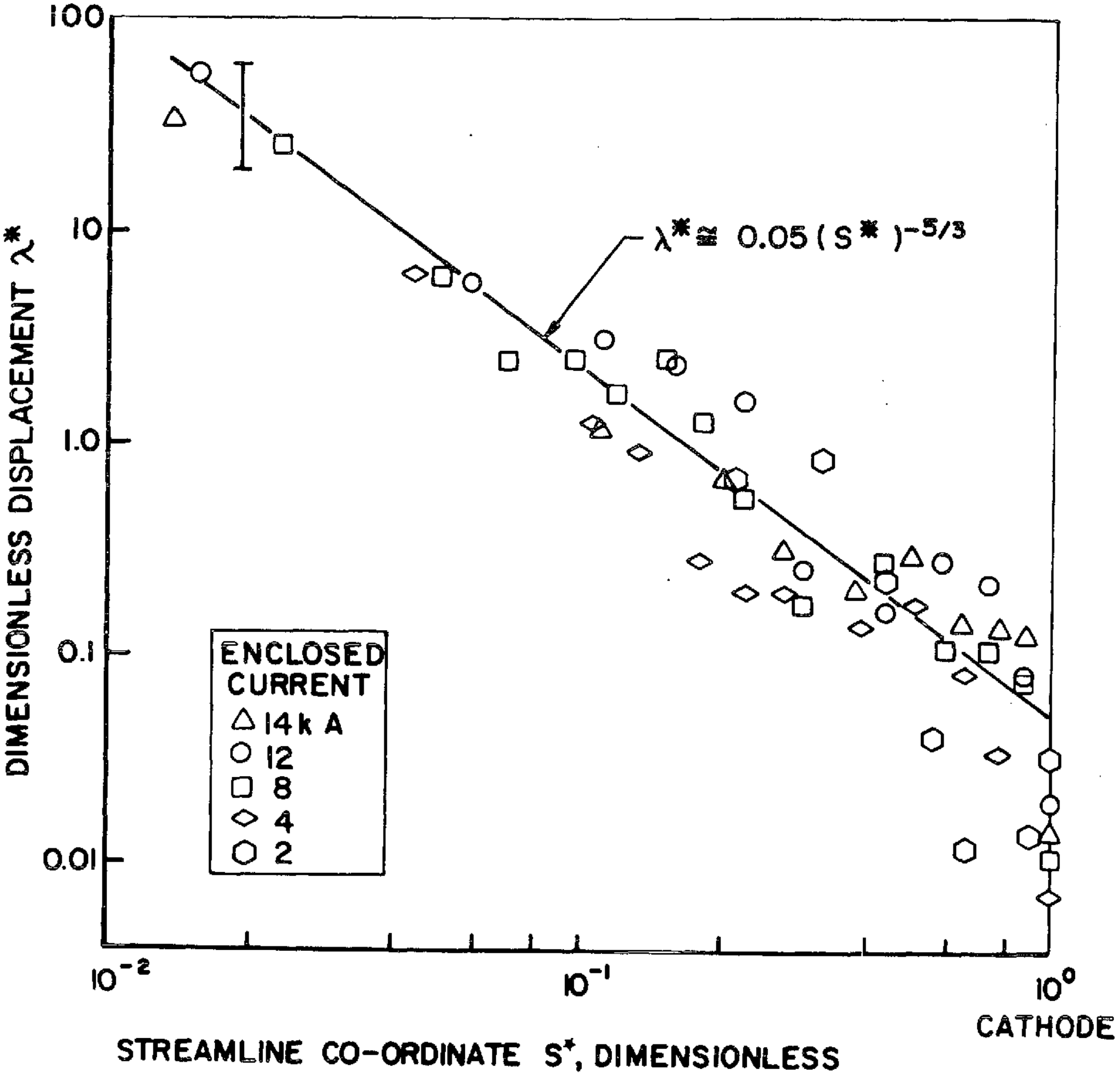

ENERGY EXCHANGE DISPLACEMENT
16 k A, 24 g/sec

FIGURE 4.18
AP25·4950

electric field by 20%: The calculation is very strongly dependent on the local plasma properties. The results for the five current contours listed in the figure fall on about the same curve

$$\lambda^* \cong 0.05(s^*)^{-5/3} \qquad (4.25)$$

The last energy exchange collision is presumed to occur at $\lambda^*=1$ or $\lambda=s$, i.e. where $s^* \cong 0.17$. Along the L=6.8 cm long 8 kA current streamline for the 16 kA x 24 g/sec discharge, s*= 0.17 represents a distance

$$s = Ls^* = 6.8(0.17) \cong 1.2\text{cm} \qquad (4.26)$$

from the anode, about one-fourth the anode orifice radius.

The locus of points where $\lambda^* = 1$ is the "anode power surface". It is shown by the circles in Fig. 4.19, where, for reference, the discharge chamber, anode, cathode, enclosed current contours and floating potentials are drawn. The voltage contribution to the anode heat flux, V_s, is the potential difference between the anode power surface and the anode. The contribution is assessed from the floating potentials along current streamlines, shown in Fig. 4.20 for the 16 kA x 24 g/sec discharge. These floating potentials are corrected to the plasma potentials illustrated in Fig. 4.21. Figure 4.21 also includes a plot of the relation $\lambda^* \cong 0.05(s^*)^{-5/3}$. For the 16 kA x 24 g/sec discharge, the voltage contribution to the anode heat flux, along the 8 kA streamline, is V_s = 11 volts. Thus, the 4 volt anode fall along the same streamline, is augmented by about 7 volts of interelectrode potential.

The anode power is calculated by integrating the results of the anode heat flux model, Eq. (4.22), over the anode surface. The calculated anode power fraction for the 16 kA x 24 g/sec discharge is 20% of the 1.3 MW arc power. This

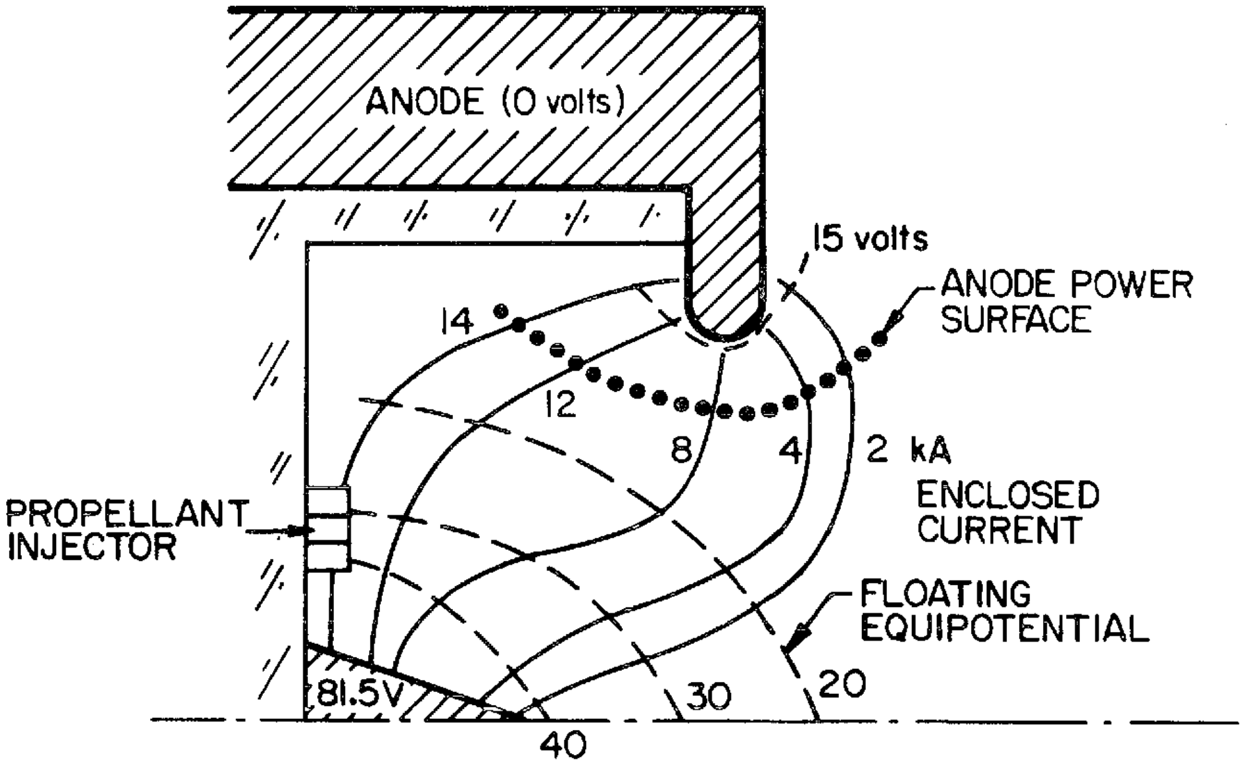

ANODE POWER SURFACE
16 kA, 24 g/sec

FIGURE 4·19
AP25·4947

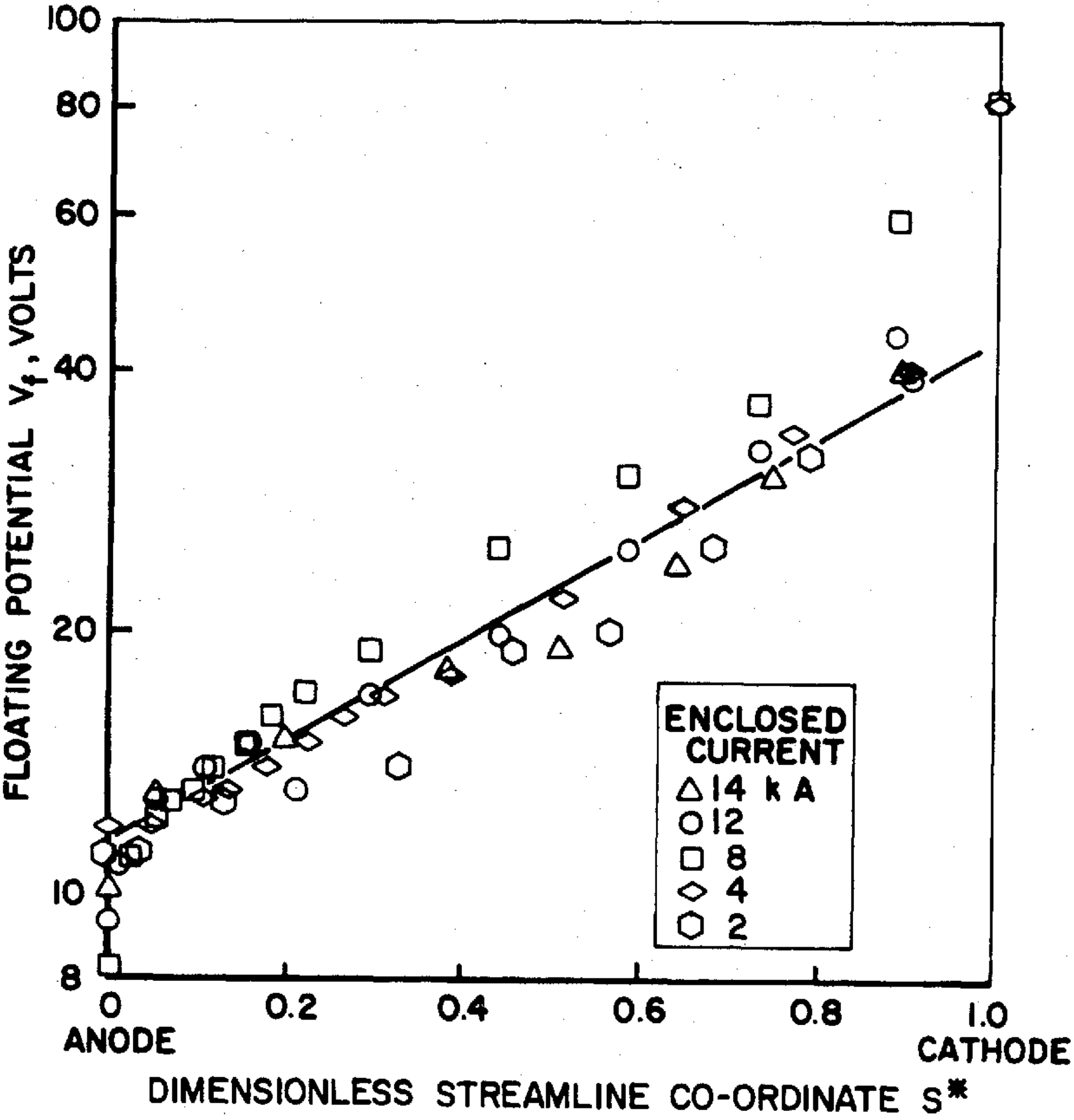

FLOATING POTENTIAL ALONG CURRENT STREAMLINES

16 kA, 24 g/sec

FIGURE 4·20
AP25·4949

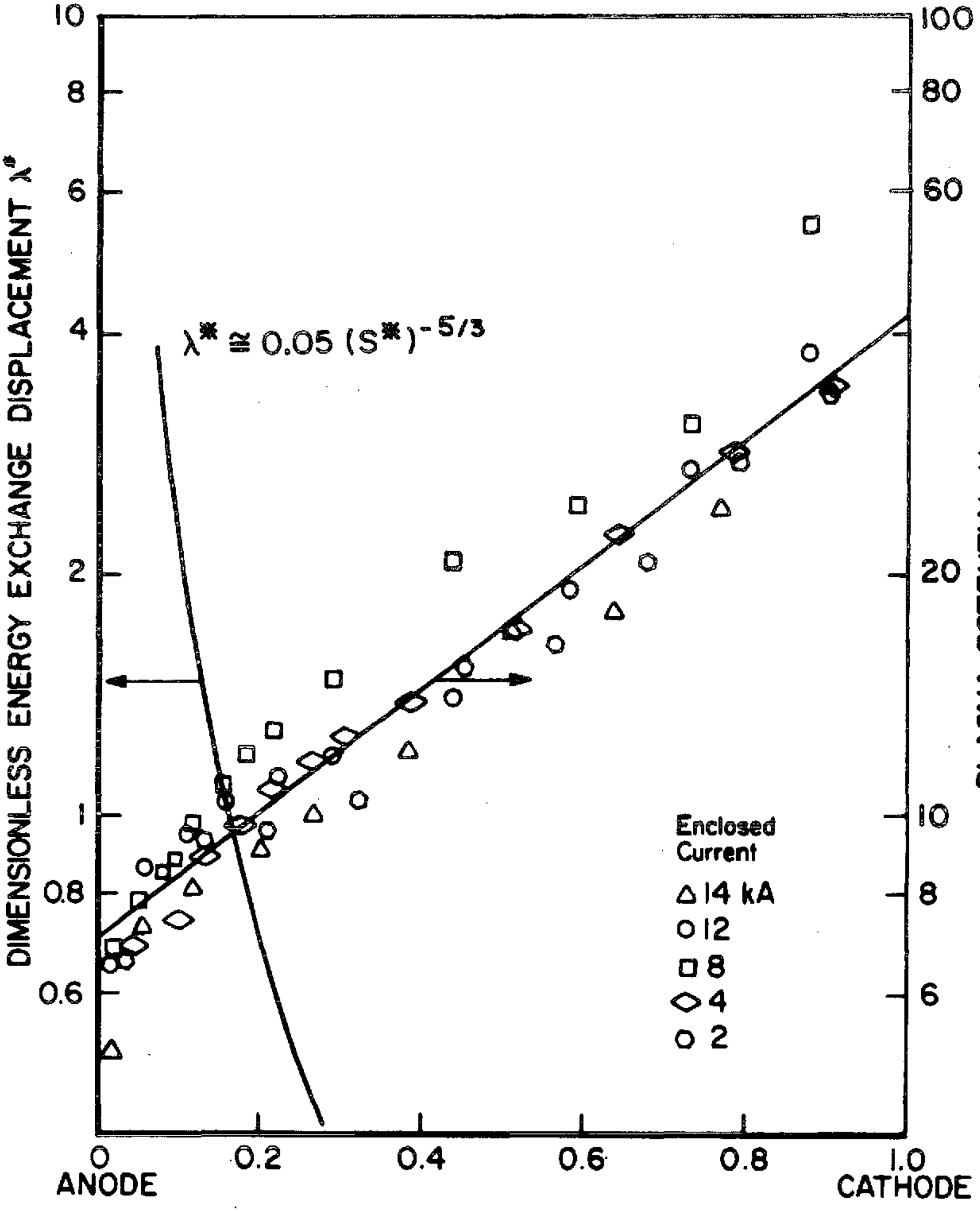

INTERELECTRODE PLASMA POTENTIAL
16kA, 24g/sec

FIGURE 4.21
AP 25-5019

agrees with the directly measured anode power fraction for the same operating condition. If the contribution from the interelectrode potential had been neglected, only half the anode power would have been accounted for.

The energy exchange displacement analysis can be applied to operation at other arc powers with the same $J^2/\dot{m} \cong 10$ kA^2-sec/g. The measured electron temperatures, current densities and anode fall voltages are used. The interelectrode potential is scaled along current streamlines for the 16 kA × 24 g/sec case and particle number densities are scaled linearly with argon mass flow (assuming equal degrees of ionization, which is reasonable since $J^2/\dot{m}$ is constant). The calculated results are shown by the circles in Fig. 4.22 where the anode power fraction is built up as the sum of the contributions[1] from electron temperature, work function, anode fall and voltage from interelectrode potential. From the figure, the voltage contributions represent more than half the anode power fraction. Figure 4.22 shows the agreement between the indirect estimates, using plasma properties, and the direct measurements of anode power (solid line) over nearly an order-of-magnitude range of arc power from 0.55 to 3.4 MW.

During multi-megawatt operation, when the number densities in the MPD discharge are high, the anode power surface is close to the anode and the commonly employed theory based on anode fall and the model presented here based on energy exchange displacement give nearly identical results. This agreement is a consequence of the decreased contribution of interelectrode potential associated with potential gradients in the discharge, which are small compared to the gradients in the anode sheath. The result suggests that for a given current and mass flow, arc geometry may be adjusted to reduce the anode power fraction to a minimum determined by the anode fall voltage required to carry the current.

---

[1] The work function for aluminum is about 4 eV. This is the same as for almost all metallic conductors.(76)

FIGURE 4.22

AP25-5016

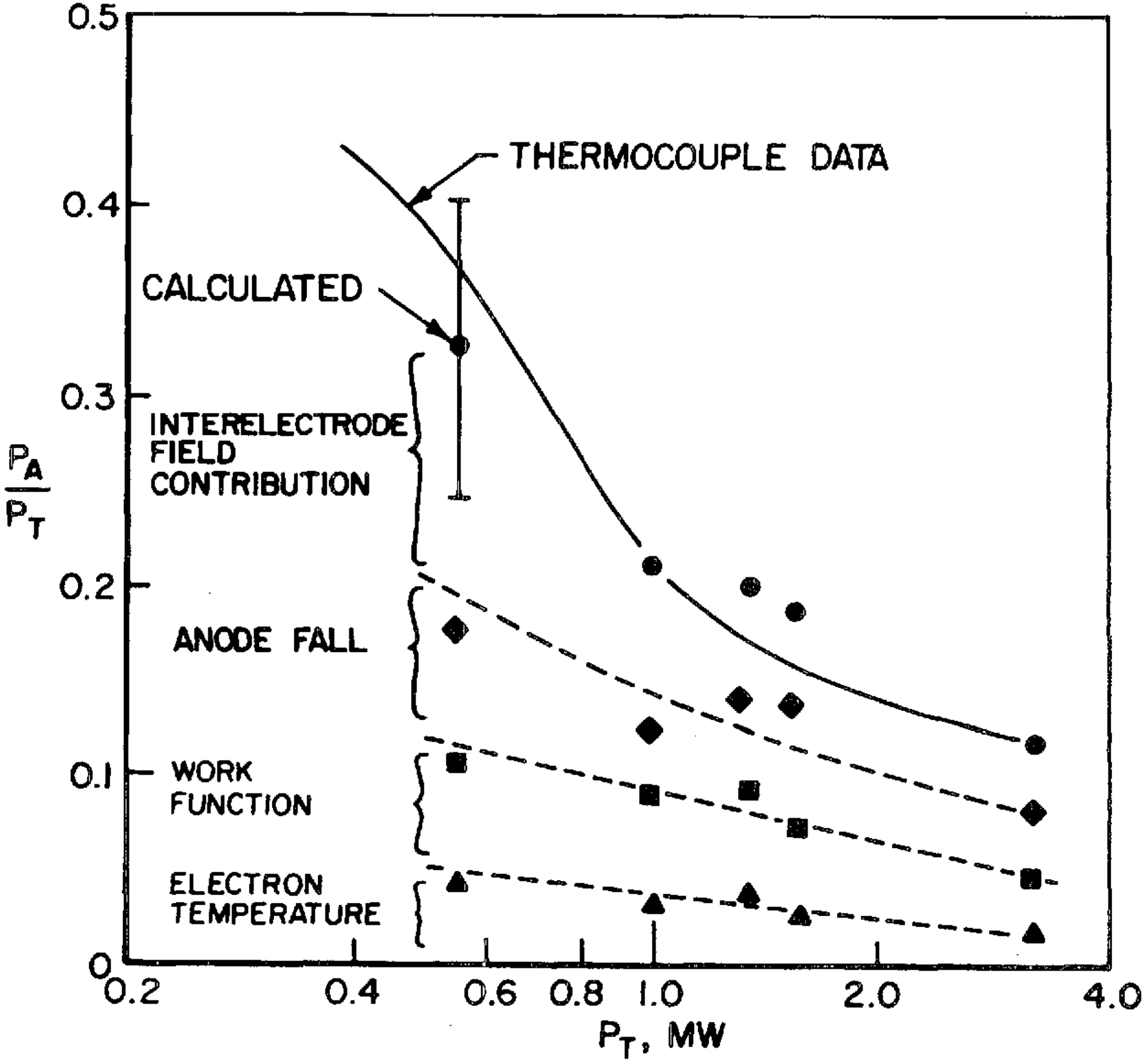

CALCULATED ANODE POWER FRACTION vs TOTAL POWER

$J^2/\dot{m} \cong 10 kA^2\text{-sec/g}$

Explanation of the decrease of anode power fraction with increasing arc power, at the same value of $J^2/\dot{m}$, now follows on the same basis. The electron temperature and work function are constant. Therefore, their contributions to the anode power fraction decrease with increasing arc voltages at elevated arc powers. In contrast, the voltage contributions from interelectrode potential and anode fall, whose sum is the largest portion of the anode power fraction, change with arc power. However, the change of their contribution can be assessed because the current distribution is constant if $J^2/\dot{m}$ remains at 10 kA^2-sec/g. The anode fall voltage portion of the anode power fraction decreases by half, from 0.08 at the low arc power of 0.55 MW to 0.04 at 3.4 MW: whereas the interelectrode potential portion, which dominates for the relatively low power arcs, decreases twice as fast from 0.15 to 0.04, as densities near the anode increase. The result is a quickly changing interelectrode potential contribution to anode power fraction, which falls from its dominating role for low arc powers to much less prominence during high-power operation. The rapid decrease of the interelectrode potential contribution, due to increased number densities in the MPD arc, causes the decrease of anode power fraction as arc power increases.

This model also deals satisfactorily with the variation of anode heat flux with mass flow at fixed arc current. An example is shown in Fig. 4.23 for 16 kA discharges with mass flows above 12 g/sec ($J^2/\dot{m} < 20$ kA^2-sec/g), where ablation and mass recirculation are negligible. In this range, anode fall voltage, electron temperature and work function are virtually independent of mass flow, while the interelectrode potential contribution to anode power decreases with mass flow in the manner calculated for the constant $J^2/\dot{m}$ case above. The total anode power fraction thus decreases with mass flow, hence increases with $J^2/\dot{m}$, as plotted. The interelectrode

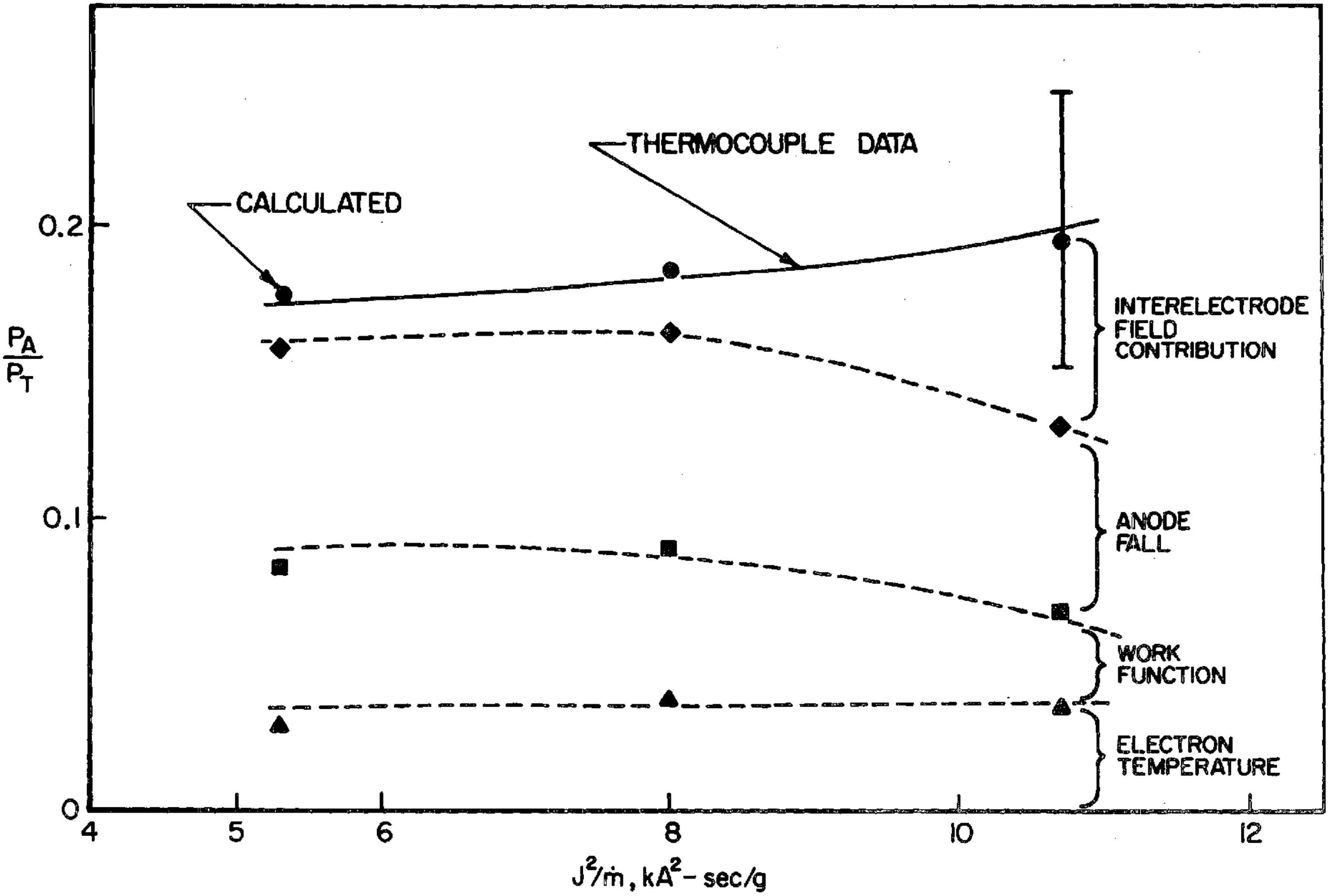

CALCULATED ANODE POWER FRACTION vs $J^2/\dot{m}$

$J = 16$ kA

FIGURE 4.23
AP25-5018

field contribution which represents over 25% of the anode power at $J^2/\dot{m} \cong 10$ kA^2-sec/g, can be neglected for lower values of $J^2/\dot{m}$. The close agreement, shown in Fig. 4.23, between the anode power results based on thermocouple data and those calculated from plasma properties supports the validity of the energy exchange model of anode heat flux in the MPD arc.

CHAPTER 5

CONCLUDING DISCUSSION

5.1 Anode Power and $J^2/\dot{m}$

The measurements of anode power in the MPD arc (Chapter 3) showed a decrease of anode power fraction, for all values of $J^2/\dot{m}$, as arc power increases; and this decrease was explained (Chapter 4), for arc operation with $J^2/\dot{m} \cong 10$ kA^2-sec/g. The explanation asserts that the decrease is due to a diminished interelectrode potential contribution to the energy electrons deliver to the anode as heat, a consequence of increased particle number densities near the anode associated with increased mass flow rates during high power operation. Now, if the anode power is expressed as the ratio of anode power to arc current P_A/J as has been done in evaluating steady arc performance,(11,32) and mass flow is expressed by the ratio $J^2/\dot{m}$ which is valid in the thruster studied if $J^2/\dot{m} < 20$ kA^2-sec/g; the result in Fig. 5.1 is derived. The figure shows a spread in the data that lies outside the representative error bars shown for 16 kA total current, but the results do cluster around a single curve. This aggregation implies that changes in the proportion of the energy electrons carry to the anode as heat depend much more strongly on mass flow than on discharge current. Furthermore, P_A/J increases when $J^2/\dot{m}$ is raised toward 20 kA^2-sec/g, i.e. when mass flow is decreased, suggesting that for all operating conditions examined, the explanation of anode power in the MPD arc is consistent with the data.

FIGURE 5-1
AP25-5017

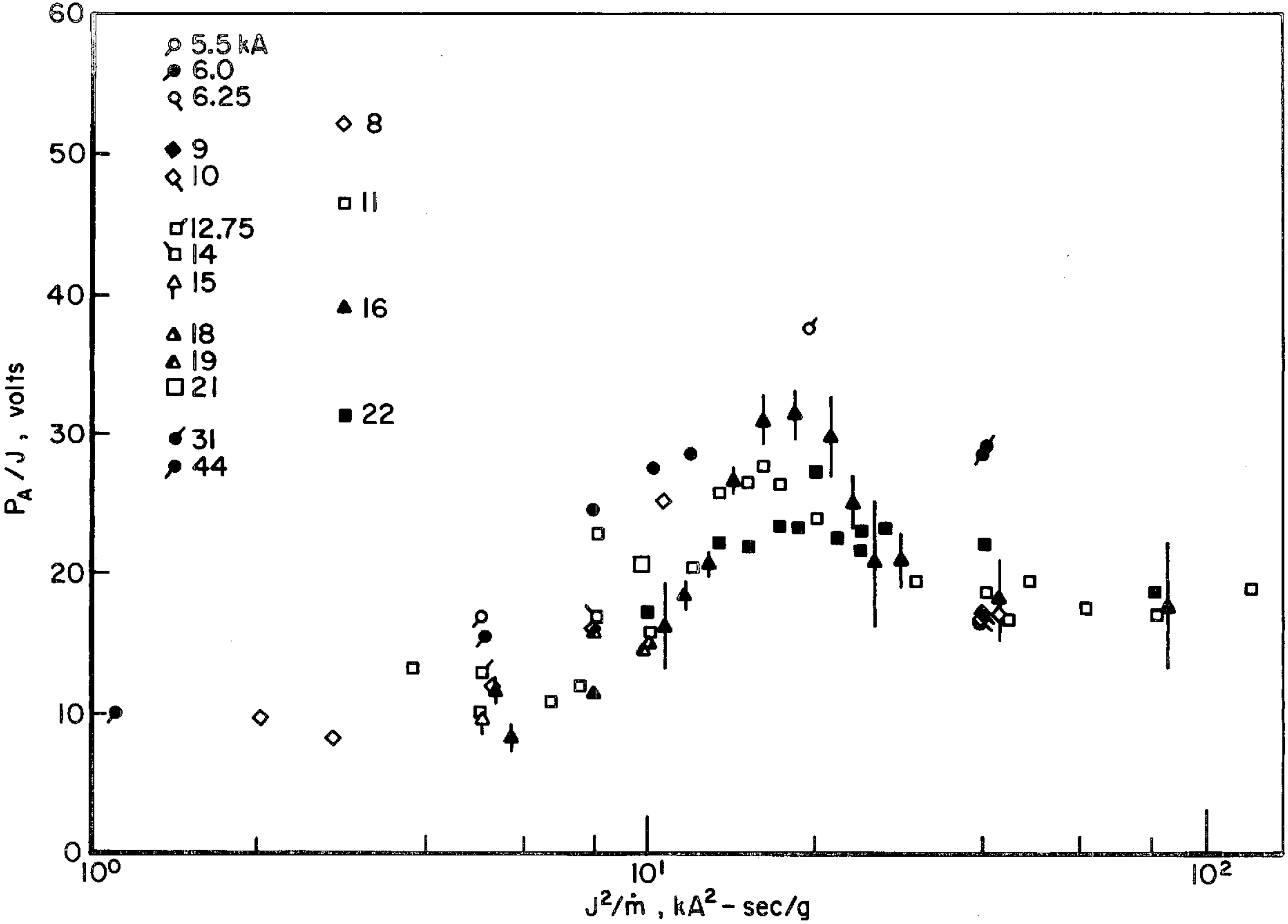

P_A/J vs $J^2/\dot{m}$

5.2 Anode Design

The measurements and the anode heat flux model that have been discussed can be used to suggest design changes for the MPD arc which may reduce anode power fraction over the entire range of arc operation. However, it must be acknowledged that any such changes in design may drastically alter other parts of the complex arc process.

Local anode heat flux may be reduced by increasing number densities near the anode which decreases the interelectrode potential contribution to the anode power. This contribution may ultimately be reduced to zero, if the anode adjacent number density is raised to that in the high pressure arcs(31,35) or greater. One possibility to increase the particle densities would be to supply a portion of the propellant mass through a porous anode. The increased heavy particle density adjacent to the anode should then permit a larger portion of the energy electrons gain in the interelectrode field to be absorbed by the heavy particles and used in the discharge. In this way otherwise "wasted" power adjacent to the anode may be usefully employed for the production of thrust. Consequently, unless the arc operating voltage increases more quickly than the interelectrode potential contribution is reduced, the anode power fraction will decrease.

Measurements in the discharge showed that the anode fall voltage is generally lowest at the lip, where current density is a maximum. The current conduction area of the anode was therefore restricted to a 1 mm wide band at the lip just upstream of the midplane. For 16 kA x 24 g/sec arc operation, the terminal voltage dropped by 25% while the anode adjacent floating potential fell by 10% compared to that of a "standard" anode. These results suggest that less power is being consumed by the anode. They also confirm the preliminary measurements of anode heat flux, on a thruster with current conduction at the anode over a 2 mm wide band at the lip, which demonstrated anode power fractions generally half those for a thruster with a fully exposed anode, at the same operating conditions.(99) On the basis of these measurements, it is suggested that current conduction at the anode be limited to a small band at the anode lip.

For a thruster with a given geometry, the choice of propellant might also reduce the anode power fraction, if it has a large electron-heavy particle energy exchange collision cross section compared to argon. The anode power surface may then move closer to the anode, thereby decreasing the anode power fraction. A suggested propellant is lithium,(77) although this major change may presage the onset of other modes of power consumption and operating difficulties. Lithium has cross sections for energy exchange at least four-orders-of magnitude larger than argon due to its low-lying excited states.(78) However, for the same reason, it is also notorious for large frozen flow losses, which may exceed any benefits to be gained. Nevertheless, although it is highly reactive, lithium is easy to store as a solid and can be liquified as it regeneratively cools the anode to regain some of the residual anode power. For those reasons, research on a multi-megawatt, lithium-fed, MPD thruster would not only be instructive but may prove beneficial to thruster improvement.

Reduction of the anode power by decreasing electron temperature and anode material work function is more difficult. The electron temperature is established by electron collision processes in the discharge and it tends to hover around 1 to 2 eV. Although propellants with higher inelastic energy exchange probabilities may be used to replace argon to decrease the electron temperature, the frozen flow losses may outstip any efficiency gains from anode power reduction. To decrease the work function contribution, different anode materials are required. Presently, the work functions for good conductors all have values of about 4 eV.(76) Improvements in them require advances in materials engineering.

5.3 Conclusions

This investigation has focused on the power consumed by the anode of the MPD arc. A series of direct thermocouple measurements of anode heat flux verify that anode power fraction decreases with increasing arc power, as suggested by previous indirect experiments.

Complementing the thermocouple measurements are probe studies of the plasma properties in the vicinity of the anode Their results are employed in an anode heat flux model modified for application to the MPD arc. In the proposed heat flux model, a key ingredient is the potential difference between the anode and the location of the last effective energy exchange collision between electrons and ions before the electrons are absorbed by the anode. For the experimental conditions examined in this study, this last energy exchange collision is located outside the anode sheath. Therefore, the energy which is added to the electron enthalpy and work function terms involves not only the anode fall, but an additional contribution from the potential fall outside the anode sheath. The difference between the commonly employed anode heat flux model and the one suggested here is simply this additional voltage contribution.

The anode power of the MPD arc, calculated on the basis of the energy-exchange model, agrees with the results of the direct measurements. It explains the decreasing fraction of input power consumed by the anode, as arc power is raised, on the basis of increased propellant mass flow, since the theoretical location of the last energy-exchange collision approaches the anode faster than the local electric field outside the anode sheath increases. Ultimately, the densities may be large enough that the relevant voltage contribution can be approximated by the anode fall, as for conventional electric arcs.

The measured decrease of anode power fraction with increasing arc power suggests that raising arc powers to multimegawatt levels makes a larger portion of the input power available to the discharge for the production of thrust, and therefore raises thrust efficiency of the accelerator.

APPENDIX A

SHELL ANODE HEAT CONDUCTION

It is desired to relate the measured temperature rise on the inside surface of the shell anode due to a quasi-steady discharge pulse to the average heat flux that produces it. The problem is solved under the assumptions that the heat flux is constant throughout the discharge period and is zero at other times, and that the anode geometry is locally flat.

Suppose that the anode can be examined locally as a slab of thickness ℓ and that the initial temperature is uniformly zero. The applicable heat conduction equation in one dimension is

$$\rho c \frac{\partial \theta}{\partial t} = k_a \frac{\partial^2 \theta}{\partial y^2} \tag{A.1}$$

where ρ , c, and k_a are the density, specific heat, and thermal conductivity of the anode material; t is time and y is distance through the slab with one face at y = o and the other at y = ℓ ; and θ is temperature.

The problem is linear and its solution is a two part sum. First the heat flux problem for a constant uniform heat flux q supplied continuously from t = o to the face at y = ℓ is solved. Then the solution is used for a constant heat flux - q of equal magnitude but opposite sign, which starts at t = T later. When these two are summed, the result applies to a rectangular heat flux q which lasts from t = o to t = T:

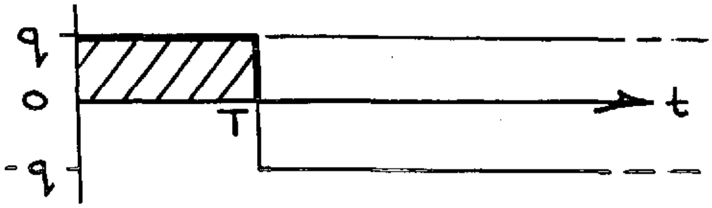

The geometry of the problem is

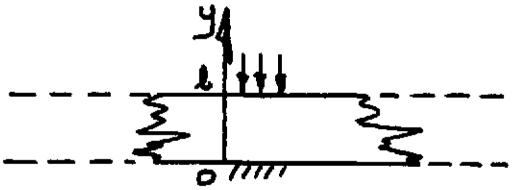

and the initial and boundary conditions are:

initial uniform zero temperature

$$\Theta(y,0) = 0 \qquad \text{(A.2)}$$

no heat flux across the boundary at $y = 0$

$$k_t \frac{\partial \Theta}{\partial y}(0,t) = 0 \qquad \text{(A.3)}$$

heat flux over the boundary at $y = \ell$ is a single, square pulse

$$k_t \frac{\partial \Theta}{\partial y}(\ell, t) = q\left\{H(t) - H(t-T)\right\} \qquad \text{(A.4)}$$

where H is the Heaviside function.

The uniform supply of heat to one side of the slab at $y = \ell$ with no loss of heat through the other side at $y = 0$ is a standard heat conduction problem and its solution appears in Carslaw and Jaeger.(73)

$$\Theta_1(y) = \frac{qt}{\rho c \ell} + \frac{q\ell}{k_t}\left\{\frac{3y^2-\ell^2}{6\ell^2} - \frac{2}{\pi^2}\sum_{n=1}^{\infty}\frac{(-1)^n}{n^2}\left[\exp\left(-\frac{\lambda\ell n^2\pi^2 t}{\ell^2}\right)\right]\cos\left(\frac{n\pi y}{\ell}\right)\right\}, t>0 \qquad \text{(A.5)}$$

where the thermal diffusivity is

$$\varkappa = \frac{k_t}{\rho c} \tag{A.6}$$

When the heat $-q$ is supplied at $t = T$,

$$\Theta_2(y) = -\frac{q(t-T)}{\rho c l} - \frac{q l}{k_t}\left\{\frac{3y^2-l^2}{6l^2} - \frac{2}{\pi^2}\sum_{n=1}^{\infty}\frac{(-1)^n}{n^2}\left[\exp\left(-\frac{\varkappa n^2\pi^2(t-T)}{l^2}\right)\right]\cos\left(\frac{n\pi y}{l}\right)\right\}, \quad t > T \tag{A.7}$$

Now, since the problem is linear, the temperature $\Theta(y)$ at times $t > T$ is found by adding $\Theta_1(y)$ and $\Theta_2(y)$, thus

$$\Theta(y) = \Theta_1(y) + \Theta_2(y) \tag{A.8a}$$

$$= \frac{qT}{\rho c l} - \frac{q l}{k_t}\left[\frac{2}{\pi^2}\left\{\sum_{n=1}^{\infty}\frac{(-1)^n}{n^2}\left[\exp\left(-\frac{\varkappa n^2\pi^2 t}{l^2}\right) - \exp\left(-\frac{\varkappa n^2\pi^2(t-T)}{l^2}\right)\right]\cos\left(\frac{n\pi y}{l}\right)\right\}\right], \quad t > T \tag{A.8b}$$

and the temperature on the unheated side $y = 0$ can be written

$$\Theta(t) = \frac{qT}{\rho c l} + \left(\frac{2}{\pi^2}\right)\frac{q l}{k_t}\left\{\sum_{n=1}^{\infty}\frac{(-1)^n}{n^2}\left[\exp\left(-\frac{\varkappa n^2\pi^2\tau}{l^2}\right)\right]\Bigg|_{\tau=t}^{\tau=t-T}\right\}, \quad t > T \tag{A.9}$$

The first term represents the final temperature of the slab while the second is the transient heating correction.

If the relation is written as

$$\Theta(t) = q\,\Phi(t) \;, \qquad t > T \tag{A.10}$$

then $\Phi(t)$ represents the temperature rise per unit heat flux and so the heat flux can be calculated from the temperature rise as

$$q = \frac{\Theta(t)}{\Phi(t)} \;, \qquad t > T \tag{A.11}$$

These computations are performed for the shell anode for temperatures measured by thermocouples mounted on the inside. The calculations are programmed for use on the IBM 360/91 computer at the Princeton University Computer Center. The series is carried to terms of relative order 10^{-7} of the preceding sum.

To establish how well the heat flux results derived from the above local, 1-dimensional formulation represent a nonuniform heat flux over the anode, it is instructive to compare Eq. (A.1) with the more general 2-dimensional heat flux equation:

$$\rho c \frac{\partial \Theta}{\partial t} = k_t \left[\frac{\partial^2 \Theta}{\partial x^2} + \frac{\partial^2 \Theta}{\partial y^2} \right] \tag{A.12}$$

where x represents a coordinate along the anode shell.

If this equation is integrated through the shell thickness ℓ

$$\int_0^{\ell} \rho c \frac{\partial \Theta}{\partial t} dy = k_t \int_0^{\ell} \frac{\partial^2 \Theta}{\partial x^2} dy + k_t \frac{\partial \Theta}{\partial y} \Big|_0^{\ell} \tag{A.13}$$

or, since no heat flows at y = o.

$$l \rho c \frac{\partial \theta}{\partial t} = k_t \int_0^l \frac{\partial^2 \theta}{\partial x^2} \, dy + q \qquad \text{(A.14)}$$

This relation can be approximated by

$$l \rho c \frac{\partial \theta}{\partial t} \cong l k_t \frac{\partial^2 \theta}{\partial x^2} + q \qquad \text{(A.15a)}$$

or

$$\rho c \frac{\partial \theta}{\partial t} \cong k_t \frac{\partial^2 \theta}{\partial x^2} + \frac{q}{l} \qquad \text{(A.15b)}$$

In this form, $k_t \partial^2 \theta / \partial x^2$ represents the correction to the one-dimensional problem.

To assess the effect of this correction, a finite difference technique is used to evaluate the ratio.$^{(81)}$

$$\delta = \frac{k_t}{\rho c} \frac{\left(\frac{\partial^2 \theta}{\partial x^2} \right)}{\left(\frac{\partial \theta}{\partial t} \right)} \qquad \text{(A.16)}$$

If $\theta_{i,j}$ represents the temperature at location i and time j , and the separation between points is Δx , while elapsed time is Δ t, the ratio becomes

$$\delta = O \left\{ \frac{k_t}{\rho c} \frac{\left[\frac{\theta_{i+1,j+1} - 2\theta_{i,j+1} + \theta_{i-1,j+1}}{(\Delta x)^2} \right]}{\left[\frac{\theta_{i,j+1} - \theta_{i,j}}{(\Delta t)} \right]} \right\}$$

$$= \frac{k_t}{\rho c} \frac{\Delta t}{\Delta x^2} \left[\frac{\theta_{i+1,j+1} - 2\theta_{i,j+1} + \theta_{i-1,j+1}}{\theta_{i,j+1} - \theta_{i,j}} \right] \qquad \text{(A.17)}$$

For arc operation at 16 kA x 24 g/sec, the most severe temperature gradients appearing on the aluminum anode are in the lip region, near the anode face. At the time the data are examined, 20 msec after the discharge,

$$\delta \cong \frac{2}{2.7(0.9)} \frac{20(10^{-3})}{(0.25)^2} \left[\frac{2 - 2(19) + 20}{19 - 0} \right] \\ \cong 0.2 \tag{A.18}$$

Thus, at the worst location, the heat flux may have an error of 20%. Elsewhere, the error is less than 10%. It is to this approximation that the one-dimensional heat flux relation, Eq. (A.11), is used everywhere on the anode.

APPENDIX B-I
THE ENERGY EXCHANGE DISPLACEMENT

The purpose of this appendix is to calculate the mean displacement along current streamlines between energy exchange collisions of the current carrying electrons and the other (heavy) species in the cylindrical MPD plasma.

Consider a "sample" electron drifting from the cathode to the anode in an axisymmetric electric field

$$\mathbb{E} = E_\xi \hat{e}_\xi + E_z \hat{e}_z \tag{B.1}$$

and an azimuthal magnetic induction field

$$\mathbb{B} = B_\theta \hat{e}_\theta \tag{B.2}$$

where e_ξ, e_θ and e_z are unit vectors in a circular cylindrical coordinate system.

The motion of the electrons is described by

$$m_e \ddot{\mathbb{r}} = e\left(\mathbb{E} + \dot{\mathbb{r}} \times \mathbb{B}\right) - \sum_j m_e \nu_{ej}^p \left(\dot{\mathbb{r}} - \dot{\mathbb{r}}_j\right) \tag{B.3a}$$

or

$$\ddot{\mathbb{r}} = \frac{e}{m_e}\left(\mathbb{E} + \dot{\mathbb{r}} \times \mathbb{B}\right) - \sum_j \nu_{ej}^p \left(\dot{\mathbb{r}} - \dot{\mathbb{r}}_j\right) \tag{B.3b}$$

where $\mathbb{r}$ is a position vector, ν_{ej}^p is the momentum-exchange collision frequency between the electron (e) and another particle (j), and e and m_e are the electronic charge and mass respectively. To simplify the formulation, the sample electron is replaced by an "average" electron, such that j=e is not considered.

To simplify Eq. (B.3b), it is assumed that particles of each species are in thermal equilibrium with one another. Therefore, they move at a mean thermal speed(82)

$$v_{th} = \sqrt{\frac{8kT}{\pi m}} \tag{B.4}$$

where m is the particle mass and k is Boltzmann's constant. Since $m_j \gg m_e$, the ratio of the mean thermal speeds of species j to the electron mean thermal speed

$$\frac{v_{th,j}}{v_{th,e}} = \sqrt{\frac{T_j}{T_e}\frac{m_e}{m_j}} << 1 \tag{B.5}$$

even if $T_j > T_e$; i.e. ions and neutrals move much more slowly than the less massive electrons. Therefore, $\dot{\mathbf{r}} \gg \dot{\mathbf{r}}_j$ and so

$$\dot{\mathbf{r}} - \dot{\mathbf{r}}_j \cong \dot{\mathbf{r}} \tag{B.6}$$

from which the equation of motion for the average electron becomes

$$\ddot{\mathbf{r}} = \frac{e}{m_e}\left(\mathbf{E} + \dot{\mathbf{r}} \times \mathbf{B}\right) - \dot{\mathbf{r}}\sum_{j \neq e} \nu_{ej}^{P} \tag{B.7}$$

The radial, azimuthal and axial components of this equation with an electromagnetic field specified by Eqs. (B.1) and (B.2) are

radial: $$\ddot{\rho}_c = \frac{e}{m_e}\left(E_\rho - B\dot{z}_c\right) - \dot{\rho}\sum_{j \neq e} \nu_{ej}^{P} \tag{B.8a}$$

azimuthal: $$\rho_c\ddot{\theta}_c + 2\dot{\rho}_c\dot{\theta}_c = -\dot{\theta}_c\rho_c\sum_{j \neq e} \nu_{ej}^{P} \tag{B.8b}$$

axial: $$\ddot{z}_c = \frac{e}{m_e}\left(E_z + B\dot{\rho}_c\right) - \dot{z}_c\sum_{j \neq e} \nu_{ej}^{P} \tag{B.8c}$$

From these equations the radial and axial motion (i.e. toward the electrodes) is independent of any azimuthal motion (although the inverse is not so). They can be written as

$$-\frac{eB}{m_e}\dot{z}_c + \frac{e}{m_e}E_\xi - \dot{\xi}_c \sum_{j\neq e} \nu_{ej}^P = 0 \qquad \text{(B.9a)}$$

$$\frac{eB}{m_e}\dot{\xi}_c + \frac{e}{m_e}E_z - \dot{z}_c \sum_{j\neq e} \nu_{ej}^P = 0 \qquad \text{(B.9b)}$$

If it is further assumed that the ionization is above a few percent, the momentum - exchange is dominated by long range Coulomb collisions between electrons and ions (i).(84) Thus,

$$\sum_j \nu_{ej}^P \cong \nu_{ei}^P \qquad \text{(B.10)}$$

and Eqs.(B.7)can be written in the form.

$$\begin{Bmatrix} \dot{\xi}_c \\ \dot{z}_c \end{Bmatrix} = \mu \begin{bmatrix} \frac{1}{1+\Omega^2} & -\frac{\Omega}{1+\Omega^2} \\ \frac{\Omega}{1+\Omega^2} & \frac{1}{1+\Omega^2} \end{bmatrix} \begin{Bmatrix} E_\xi \\ E_z \end{Bmatrix} \qquad \text{(B.11)}$$

where

$$\mu \equiv \frac{e}{m_e \nu_{ei}^P} \qquad \text{(B.12a)}$$

$$\omega_g \equiv \frac{eB}{m_e} \qquad \text{(B.12b)}$$

$$\Omega \equiv \frac{\omega_g}{\nu_{ei}^P} \qquad \text{(B.12c)}$$

are the electron mobility, Larmor radius and Hall parameter.(58,62,83)

Now, the integral of Eq. (B.9) is to be found over the mean free time between energy exchange collisions

$$\tau_e^E = \frac{1}{n_h Q_{eh}^{(\beta)} v_{th_e}} \qquad \text{(B.13)}$$

where n_h is the number density of the field particles (h) which exchange energy with the electron and $Q_{eh}^{(\beta)}$ is the collision cross section for the energy exchange mechanism β.

Thus,

$$\lambda_s^E \equiv \int_0^{\tau_e^E} \begin{Bmatrix} \dot{\varrho}_c \\ \dot{z}_c \end{Bmatrix} dt \tag{B.14a}$$

$$= \begin{Bmatrix} \varrho_c(\tau_e^E) \\ z_c(\tau_e^E) \end{Bmatrix} - \begin{Bmatrix} \varrho_c(0) \\ z_c(0) \end{Bmatrix}$$

$$= \begin{Bmatrix} \Delta\varrho_c \\ \Delta z_c \end{Bmatrix} \tag{B.14b}$$

is the change in the electrons position between energy exchange collisions. This result is valid if the electron mobility, Larmor radius, Hall parameter and electric field are constant over the distance between energy exchange collisions, because the motion is then determined independantly of energy exchange. To within the accuracy of the experimental measurements in this study, this is the case in the MPD discharges examined here.

The position change corresponds to a distance

$$|\lambda_s^E| = \left[(\Delta\varrho)^2 + (\Delta z_c)^2\right]^{1/2}$$

$$= \frac{\mu}{1+\Omega^2}\,\tau_e^E \left\{E_\varrho^2(1+\Omega^2) + E_z^2(1+\Omega^2)\right\}^{1/2} \tag{B.15}$$

which follows a current streamline since electrons carry the current. Hence, the energy exchange displacement along a current streamline is

$$|\lambda_s^E| = \frac{\mu}{\sqrt{1+\Omega^2}}\,\tau_e^E\,|E| = \lambda \tag{B.16}$$

The displacement λ is a linear function of the electric field and the energy exchange mean free time: It increases if potential gradient increases and increases as the energy exchange cross section decreases. The Hall parameter represents the influence of magnetic field: A large Hall parameter indicates increased electron residence on the azimuthal magnetic field lines and therefore a decreasing net displacement.

APPENDIX B-II

ENERGY EXCHANGE COLLISIONS IN THE MPD ARC

The event which dominates the energy exchange in the MPD arc is the one with the largest collision frequency

$$\nu_{eh}^{E} = n_h Q_{eh}^{(\beta)} v_{th,e} \tag{B.17}$$

where n_h, the heavy particle number density, may represent ions and atoms.

The energy exchange processes occurring between the electrons and the heavy particles are neutral and ion excitation, neutral and ion ionization, and elastic energy exchange. The energy exchange process which dominates in the anode region of the MPD discharge is assessed using energy averaged cross sections representing collision frequencies ÷ nv. These energy-averaged cross sections are estimated below for an argon plasma with a 1.2 eV electron temperature:

$Q_{ea}^{E,ion}$: Ionization of neutral argon atoms by electron collision.

The threshold for this event is 15.75 eV, the ionization potential of argon, which is well above the mean electron energy in the plasma. From Appendix D-I, the effective inelastic cross section between electrons with a Maxwellian distribution whose mean energy is below threshold, and heavy particles which are not moving is

$$< Q_{eh}^{(\beta)} > \cong q_{0eh}^{(\beta)} \frac{kT_e}{E_1 - E_0}\left(\frac{E_0}{kT_e} + 2\right)\exp\left(-\frac{E_0}{kT_o}\right) \tag{B.18}$$

where E_o is the threshold for the event and E_1 is the energy where a linear approximation to the increasing part of the actual cross section is assumed to have a value equal to the maximum cross section $q_{eh}^{(\beta)}$. For the ionization of the neutral argon atom, the maximum cross section, $4(10^{-20})\ m^2$, occurs at about 16 eV.(85)

Therefore,

$$Q_{ea}^{E,ion} \cong 4(10^{-20}) \frac{1.2}{45-16} \left(\frac{16}{1.2} + 2 \right) \exp\left(- \frac{16}{1.2} \right) \tag{B.19a}$$

$$\cong 8(10^{-26})\ m^2 \tag{B.19b}$$

$Q_{ei}^{E,ex}$: Excitation of argon ions by electron collision.

Excitation events which populate excited states of the argon ion from the ground state have thresholds about 17 eV. The maximum cross section is on the order of $1.2(10^{-20})\ m^2$ for 21 eV electrons.(86–89) Therefore, the effective cross section in the 1.2 eV electron temperature plasma is about $Q_{ei}^{E,ex} = (10^{-27})\ m^2$.

$Q_{ei}^{E,ion}$: Second ionization by electron collision.

This event has threshold at 24 eV and a maximum cross section of $1.2(10^{-20})\ m^2$ for 79.4 eV electrons.(85) Its effective cross section is about $Q_{ei}^{E,ion} = 9(10^{-30}) m^2$.

$Q_{ea}^{E,ex}$: Excitation of neutral argon atoms by electron collision.

Although the energies of threshold and maximum are well documented and resonance energy levels are available, the absolute magnitudes of the cross section are not well known and can only be roughly estimated.(89) The cross section assumed here is conservatively large. It rises from an 11 eV threshold to a maximum at 22 eV. At the peak it is assumed to be $4(10^{-22})\ m^2$, two orders-of-magnitude smaller than the maximum cross section for ionization of the atom.(90) Equation (B.17) gives $Q_{ea}^{E,ex} = 3(10^{-26})\ m^2$.

$Q_{ei}^{E,p}$: Translational energy lost in elastic, Coulomb momentum-exchange collisions between ions and electrons.

This event does not populate ion excited states but it is and provides a mechanism way for electrons to share energy with ions. The fraction of the incident energy lost by electrons in these elastic encounters is $2(m_e/m_i)$ of the incident energy.(91,92) Therefore, the energy the electrons have is effectively exchanged in about 35,000 encounters. For the electron temperature of 1.2 eV and an electron number density of $10^{21} m^{-3}$ in the anode region (see Fig. 4.17), the Coulomb momentum-exchange cross section, from Eq. (4.36), is about $1(10^{-17})\ m^2$. Therefore, the energy exchange cross section is about $4(10^{-22})\ m^2$. This is larger than the other cross sections for energy exchange, but the magnitude decreases by about 25% with each 10% increase in electron temperature.

The cross sections above are now used along with the estimates of the heavy particle number densities to calculate the energy exchange collision frequencies. First the heavy particle number densities are related to the electron density in the discharge. For the quasi-neutral plasma, the ion and electron number densities are equal

$$n_e = n_i \qquad \text{(B.20)}$$

and if the ionization fraction, the ratio of ion to ion-plus-neutral number density, is α; the neutral argon number density is

$$n_a = \left(\frac{1-\alpha}{\alpha}\right) n_e \qquad \text{(B.21)}$$

Thus, the collision frequency for electron-ion energy exchange is

$$\nu_{ei}^{(\beta)} = n_e Q_{ei}^{(\beta)} v_{th,e} \tag{B.22}$$

whereas for electron-atom collisions it is

$$\nu_{ea}^{(\beta)} = n_e \left(\frac{1-\alpha}{\alpha}\right) Q_{ea}^{(\beta)} v_{th,e} \tag{B.23}$$

where (β) is the type of event. For the 16 kA x 24 g/sec discharge, whose electron temperature is about 1.2 eV, in an estimated ionization fraction $\alpha = 0.9$.(98) Therefore, the ratio $(1-\alpha)/\alpha \cong 0.11$. The collision cross sections above, used in the collision frequencies $\nu_{ei}^{(\beta)}$ and $\nu_{ea}^{(\beta)}$ from Eqs. (B.22) and (B.23), then show that multiple elastic Coulomb momentum-exchange collisions $Q_{ei}^{E,p}$ dominate the energy exchange process in the MPD arc. The multiple elastic collisions would still exceed the other events if the ionization fraction were 0.01, two orders-of-magnitude smaller. However, if the electron temperature increases to the neighborhood of 5 eV, the inelastic exchange mechanisms will dominate the energy exchange process.

APPENDIX C

REDUCTION OF FLOATING POTENTIAL TO PLASMA POTENTIAL

Although floating potential measurement is straightforward, the magnitude of floating potential does not equal the plasma potential at the probe location. The difference is a shift toward cathode potential because the electron arrival rate to the probe electrode surface, due to their random thermal flux, is much higher than that of the ions. The shift is calculated by assuming that the probe is immersed in a streaming plasma. Since the probe radius is less than the Larmor radius,[1] magnetic field effects are neglected.(93)

An electron current toward the probe exists in the plasma because electron mobility is much higher than that of the ions. The result is a negative sheath which repels electrons and attracts ions. However, to attract sufficient ion current to maintain the no net current condition, a "pre-sheath" is created between the plasma and the actual probe sheath.(94) The pre-sheath is quasi-neutral, but has an electric field which accelerates ions. In a quiescent plasma with a Maxwellian electron distribution, Bohm has shown that the pre-sheath accelerates ions to the speed(63)

$$u_b = \frac{1}{2}\sqrt{\frac{kT_e}{m_i}} \qquad (C.2)$$

where m_i is the ion mass, T_e is the electron temperature and k is Boltzmann's constant. Thus, the ion current to

---

[1] The Larmor radius due to a magnetic field B is

$$\lambda_g \cong \frac{m_e v_{th,e}}{eB} = \frac{1}{eB}\left(\frac{8kT_e m_e}{\pi}\right)^{1/2} \qquad (C.1)$$

where m_e is the electron mass and the electron thermal speed $v_{th,e} = \sqrt{8kT_e/\pi m_e}$. For a 1.2 eV electron temperature and a magnetic field of 10^{-2} Webers/m, the Larmor radius is about $4(10^{-4})$m which is greater than the probe radius of about 10^{-4}m.

the probe is

$$I_i = eZn_iu_bA \tag{C.3a}$$

$$= eZn_i\frac{1}{2}\sqrt{\frac{kT_e}{m_i}}\;A \tag{C.3b}$$

where Z is the ion charge number, n_i is the ion number density and A is sheath area. If the probe has a characteristic dimension much less than any macroscopic dimension associated with the plasma and much larger than the Debye length,(61) then A equals the probe conduction area.

The electron velocity toward the probe is

$$u_e = \sqrt{\frac{kT_e}{2\pi m_e}} \tag{C.4}$$

where m_e is the electron mass. Thus, the electron current to a probe with a voltage bias $\Delta V = V_p - V_f$ with respect to the plasma is

$$I_e = en_e\exp\left[-\frac{e(V_p-V_f)}{kT_e}\right]\sqrt{\frac{kT_e}{2\pi m_e}}\;A \tag{C.5}$$

The pre-sheath will adjust its voltage and thickness to maintain the zero net probe current at floating potential

$$I_i = I_e \tag{C.6}$$

Since the plasma is quasi-neutral at the "boundary" between the sheath and the pre-sheath,

$$n_i = n_e \tag{C.7}$$

and so

$$Z\frac{1}{2}\sqrt{\frac{1}{m_i}} = \exp\left[-\frac{e(V_p-V_f)}{kT_e}\right]\sqrt{\frac{1}{2\pi m_e}} \tag{C.8}$$

Thus, the correction from floating to plasma potential is

$$\Delta V = V_p - V_f = -\frac{kT_e}{e}\ln\left(Z\sqrt{\frac{\pi}{2}\frac{m_e}{m_i}}\right) \tag{C.9a}$$

For a singly ionized argon plasma,

$$\Delta V \cong -5.4\,\frac{kT_e}{e} \tag{C.9b}$$

However, in a streaming plasma, the ions may have a velocity u which exceeds the Bohm speed $\frac{1}{2}\sqrt{kT_e/m_i}$ and a smaller pre-sheath voltage is required to balance ion and electron currents.(95)

Suppose the ion streaming current is

$$I_{is} = eZu'n_iA_s \tag{C.10}$$

where u' is the component of streaming velocity normal to the probe and A_s is an appropriate ion collection area of the probe. If ion current is assumed to be the sum of Bohm speed and streaming velocity contribution, the current balance becomes

$$I_i + I_{is} = I_e \tag{C.11a}$$

$$eZ\frac{1}{2}\sqrt{\frac{kT_e}{m_i}}\,n_iA + eZu'n_iA_s = e\sqrt{\frac{kT_e}{2\pi m_e}}\left[n_e\exp\left(-\frac{e(V_p-V_f)}{kT_e}\right)\right]A \tag{C.11b}$$

Therefore,

$$\Delta V = V_p - V_f = -\frac{kT_e}{e}\ln\left\{\frac{Z}{A}\sqrt{\frac{2\pi m_e}{kT_e}}\left[\frac{A}{2}\sqrt{\frac{kT_e}{m_i}} + A_su'\right]\right\} \tag{C.12}$$

In Eq. (C.12), ion current is expressed as the sum of a "Bohm" current $I_i \propto u_b$ and an "ion streaming component" current $I_{is} \propto u'$. When $0 \leq u' < u_b$, the Bohm current dominates the logarithm. Ion streaming becomes important when $u' \gg u_b$, i.e. when the ion velocity component normal to the probe exceed the Bohm speed.

The area for streaming ion current is probably larger than the projected probe area normal to the ion stream since the probe potential bias will bend the ion trajectories to draw current. However, it is unlikely that ions are collected over the entire probe area. Therefore, half the probe area is selected as a compromise for streaming ion collection.

$$A' = \frac{A}{2} \qquad \text{(C.13)}$$

Also, since A' appears in the logarithm argument, its value may change by a factor of two without significantly affecting ΔV.

The probe correction for ions streaming toward the probe, becomes

$$\Delta V = V_p - V_f = -\frac{kT_e}{e}\ln\left\{2\sqrt{\frac{\pi m}{2kT_e}}\left[\sqrt{\frac{kT_e}{m_i}} + u'\right]\right\} \qquad \text{(C.14)}$$

and for a singly ionized argon plasma with electron temperatures in the range from 0.6 to 2 eV (T_e = 7000 to 23,000 °K) and ions streaming at about 10^4 m/sec, the correction is

$$\Delta V \cong -3.5\,\frac{kT_e}{e} \qquad \text{(C.15)}$$

APPENDIX D

FOLDING OF INELASTIC CROSS-SECTIONS WITH ELECTRON DISTRIBUTION

The electron distribution $n_e(E)$ and the collision cross section $Q_{eh}^{(\beta)}(E)$ for an inelastic event (β) between the electron and a heavy particle (h) are functions of energy E. Schematically they might look like the sketch below:(96)

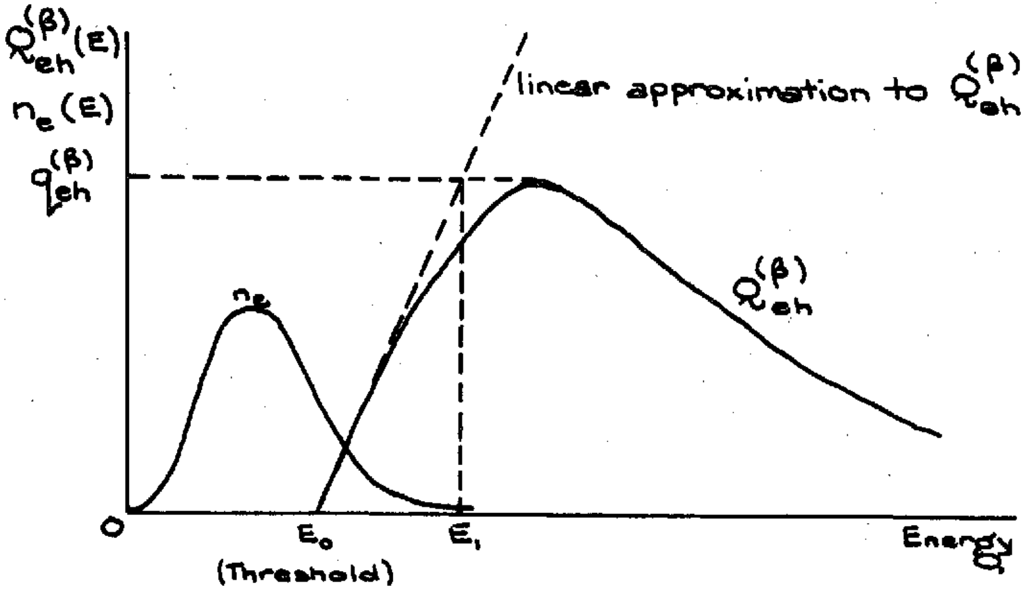

The electron temperature for the distribution shown represents a lower average energy than the threshold for the energy exchange process, but there is a portion of the population that is energetic enough to accomplish the inelastic event. If the actual energy exchange cross section $Q_{eh}^{(\beta)}(E)$ is folded into the electron distribution, an "effective" collision frequency and a mean cross section for the event can be computed.

Suppose energy is written in the form

$$E = \frac{1}{2} m v^2 \tag{D.1}$$

where m is mass and v is velocity and energy distributions are replaced by distributions in velocity. The mean collision frequency $\langle \nu_{eh}^{(\beta)} \rangle$ for an inelastic event may then be calculated from

$$n_{eo} \langle \nu_{eh}^{(\beta)} \rangle = \iint n_e(v_e)\, n_h(v_h)\, Q_{eh}^{(\beta)} \left[\frac{m_e (v_e)^2 - m_h (v_h)^2}{2} \right] \times$$

$$|(v_e - v_h)|\, dv_e\, dv_h \tag{D.2}$$

where $[\quad]$ indicates "function of" and where $n_e(v_e)$ and $n_h(v_h)$ are electron and heavy particle distributions in velocity space, n_{eo} is the integral of the electron distribution over velocity space and m_e and m_h are the electron and heavy particle masses. If the heavy particles are not moving:

$$v_h^2 = 0 \tag{D.3}$$

Eq. (D.2) becomes

$$n_{eo} \langle \nu_{eh}^{(\beta)} \rangle = \iint n_e(v_e)\, n_h(v_h)\, Q_{eh}^{(\beta)} \left[\frac{m_e v_e^2}{2} \right] |v_e|\, dv_e\, dv_h$$

$$= n_h \int n_e(v_e)\, Q_{eh}^{(\beta)} \left[\frac{m_e v_e^2}{2} \right] |v_e|\, dv_e \tag{D.4}$$

For a Maxwell-Boltzmann electron distribution about temperature T_e

$$n_e(v_e) = n_{eo} \left(\frac{m}{2\pi k T_e} \right)^{3/2} \exp\left(- \frac{m_e v_e^2}{2kT_e} \right) \tag{D.5}$$

the integral becomes,

$$n_{eo}\langle \nu_{eh}^{(\beta)}\rangle = n_h \int n_{eo}\left(\frac{m_e}{2\pi k T_e}\right)^{3/2} \exp\left(-\frac{m_e V_e^2}{2kT_e}\right)\times Q_{eh}^{(\beta)}\left[\frac{m_e V_e^2}{2}\right]|V_e|\,dV_e \tag{D.6}$$

Let $Q_{eh}^{(\beta)}$ be approximated by a cross section that zero at threshold and rises linearly with energy with a slope equal to that at threshold:

$$Q_{eh}^{(\beta)} \sim q_{eh}^{(\beta)}\left(\frac{E-E_o}{E_1-E_o}\right) \tag{D.7}$$

where $q_{eh}^{(\beta)}$ represents the maximum cross section for the event, E_o is the threshold energy, and E_1 is the energy where the maximum cross sectioned is assumed to occur. Using the definition of Eq. (D.1), the cross section can also be represented as

$$Q_{eh}^{(\beta)} \sim q_{eh}^{(\beta)}\left(\frac{V_e^2 - V_{eo}^2}{V_{e1}^2 - V_{eo}^2}\right) \tag{D.8}$$

This formula is substituted into Eq. (D.6) to form

$$n_{eo}\langle \nu_{eh}^{(\beta)}\rangle \approx n_h \int_{V_{eo}}^{\infty}\left(\frac{m_e}{2\pi k T_e}\right)^{3/2} \exp\left(-\frac{m_e V_o^2}{2kT_e}\right)\times q_{eh}^{(\beta)}\left(\frac{V_e^2 - V_{eo}^2}{V_{e1}^2 - V_{eo}^2}\right)|V_e|\,d V_e \tag{D.9}$$

Since the integral is zero for electron velocities from 0 to V_{eo}, the limits of integration over all velocity space are replaced by integration from threshold velocity V_{eo}. Infinity is retained as the upper limit, since the integrand decays exponentially as the square of velocity, the independant variable. This use of infinity simplifies the computation without seriously effecting the result.

The integral is then written as

$$n_{eo}\langle \nu_{eh}^{(\beta)}\rangle \approx n_h n_{eo} \frac{q_{eh}^{(\beta)}}{V_{e1}^2-V_{eo}^2}\left(\frac{m_e}{2\pi kT_e}\right)^{3/2}\int_{V_{eo}}^{\infty}\left\{V_e^2|V_e| - V_{eo}^2|V_e|\right\}\times$$
$$\exp\left(-\frac{m_e V_e^2}{2kT_e}\right)dV_e \qquad \text{(D.10)}$$

To integrate the spherical coordinate system shown below is used

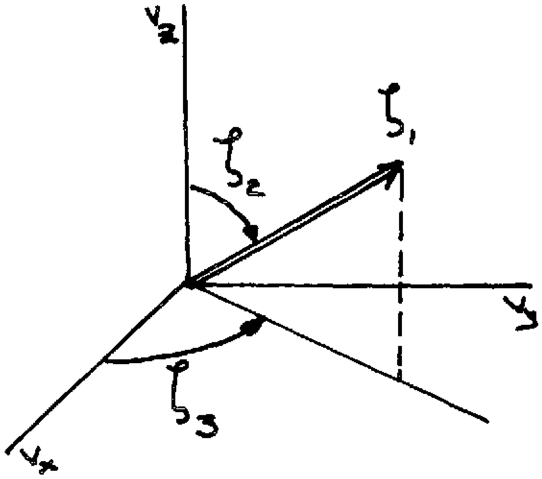

$$V_x = \zeta_1 \sin(\zeta_2)\cos(\zeta_3) \qquad \text{(D.11a)}$$
$$V_y = \zeta_2 \sin(\zeta_2)\sin(\zeta_3) \qquad \text{(D.11b)}$$
$$V_z = \zeta_3 \cos(\zeta_3) \qquad \text{(D.11c)}$$

Thus

$$|V_e| = \zeta_1 \qquad \text{(D.12)}$$

$$dV_e = \zeta_1^2 \sin(\zeta_2)\, d\zeta_1 d\zeta_2 d\zeta_3 \qquad \text{(D.13)}$$

and

$$n_{eo}\langle \nu_{eh}^{(\beta)}\rangle \approx n_h n_{eo} \frac{q_{eh}^{(\beta)}}{V_{e1}^2-V_{eo}^2}\left(\frac{m_e}{2\pi kT_e}\right)^{3/2}\times \qquad \text{(D.14)}$$
$$\int_{V_{eo}}^{\infty}\int_{0}^{\pi}\int_{0}^{2\pi}\left\{\zeta_1^5 - V_{eo}^2\zeta_1^3\right\}\exp\left(-\frac{m_e\zeta_1^2}{2kT_e}\right)\sin(\zeta_2)\,d\zeta_1 d\zeta_2 d\zeta_3$$

After integration and simplification, Eq. (D.13) becomes

$$n_{eo}\langle \nu_{eh}^{(\beta)}\rangle \approx \sqrt{\frac{32}{\pi}}\, n_h n_{eo} \frac{q_{eh}^{(\beta)}}{V_{e1}^2 - V_{eo}^2}\left(\frac{kT_e}{m_e}\right)^{3/2} \times \left(\frac{m_e V_{eo}^2}{2kT_e} + 2\right)\exp\left(-\frac{m_e V_{eo}^2}{2kT_e}\right) \qquad \text{(D.15)}$$

The velocity squared V^2 can be replaced by $\sqrt{2E/m}$ from Eq. (D.1). Therefore, Eq. (D.14) becomes

$$n_{eo}\langle \nu_{eh}^{(\beta)}\rangle \approx \sqrt{\frac{8}{\pi}}\, n_h n_{eo} \frac{q_{eh}^{(\beta)} m_e}{(E_1 - E_0)}\left(\frac{kT_e}{m_e}\right)^{3/2} \times \left(\frac{E_0}{kT_e} + 2\right)\exp\left(-\frac{E_0}{kT_e}\right) \qquad \text{(D.16)}$$

Next, let

$$\langle \nu_{eh}^{(\beta)}\rangle \equiv n_h \langle Q_{eh}^{(\beta)}\rangle V_{th,e} \qquad \text{(D.17)}$$

and since the electron mean thermal speed is

$$V_{th,e} = \sqrt{\frac{8kT_e}{\pi m_e}} \qquad \text{(D.18)}$$

Therefore,

$$\langle Q_{eh}^{(\beta)}\rangle \approx q_{eh}^{(\beta)}\left(\frac{kT_e}{E_1 - E_0}\right)\left(\frac{E_0}{kT_e} + 2\right)\exp\left(-\frac{E_0}{kT_e}\right) \qquad \text{(D.19)}$$

Thus, the energy dependent inelastic cross-section is replaced by a mean value which depends on the threshold energy E_0, the cross-section maximum $q_{eh}^{(\beta)}$, the slope of the cross section at threshold and the electron temperature.

APPENDIX E

ANODE HEAT FLUX AND POWER: COMPENDIUM OF RESULTS

ARC OPERATING CONDITIONS					LOCAL ANODE HEAT FLUX (q_a) W/cm²												
Cur-rent	Mass Flow	$\frac{J^2}{\dot{m}}$	Volt-age	Power	CHAMBER			LIP				DOWNSTREAM FACE				Anode Power	Anode Power Fraction
					Thermocouple												
(J)	($\dot{m}$)	($J^2/\dot{m}$)	(V)	(P_T)	A	B	C	D	E	F	G	H	K	L	M	(P_A)	(P_A/P_T)
kA	$\frac{g}{sec}$	$\frac{kA^2\text{-}sec}{g}$	v	MW	Location (cm) -1.2	-0.8	-0.4	0.0	0.2	0.5	0.8	1.0	1.5	2.3	3.5	kW	
5.5	6.0	5	46	0.26	10	50	670	2020	2550	1980	2070	170	30	20	10	92	0.36
6.0	3.0	12	67	0.40	20	80	1600	4270	4650	3660	2650	220	40	20	30	171	0.43
6.0	3.5	10	64	0.39	10	70	1530	4050	4540	3640	2700	220	30	20	20	165	0.43
6.0	4.5	8	54	0.32	10	60	1120	3410	4010	3320	2980	220	30	20	20	147	0.45
6.0	7.0	5	46	0.27	10	60	580	1930	2680	1950	2330	200	30	20	10	93	0.34
6.0	32.0	1	44	0.27	0	80	770	1640	1170	1210	620	90	30	20	30	60	0.23
6.3	1.0	40	98	0.62	40	70	570	2330	2630	1780	1020	120	90	110	140	104	0.17
6.3	2.0	20	85	0.54	20	130	600	4830	5090	8710	5110	140	40	30	30	233	0.49
8.0	1.5	43	127	1.01	40	250	2720	2950	3330	1920	1310	70	50	50	50	138	0.14
8.0	6.0	11	69	0.55	20	120	1210	4730	5580	4810	4240	280	40	30	30	203	0.37
8.0	8.0	8	55	0.44	10	80	730	2670	3590	2640	3350	300	40	30	30	130	0.29
8.0	12.0	5	56	0.45	10	60	500	1420	2340	2310	2180	630	50	30	30	95	0.21
8.0	24.0	3	51	0.40	10	400	810	1490	1450	950	600	120	40	30	30	65	0.16
8.0	32.0	2	51	0.41	0	240	830	1950	1600	1480	860	170	50	30	30	77	0.19
9.0	2.0	41	137	1.23	50	290	2070	3430	3200	2200	1410	130	120	110	130	154	0.13
10.0	2.5	40	144	1.44	60	340	1660	3500	3880	2600	1710	140	150	150	180	171	0.12
11.0	1.0	121	187	2.06	70	390	2680	4740	4610	3210	1850	200	150	120	130	206	0.10
11.0	1.5	81	179	1.96	50	370	2170	4380	4110	2750	1650	190	140	110	110	188	0.10
11.0	2.0	61	169	1.86	60	380	2080	4410	4510	2910	1800	170	140	130	150	192	0.10
11.0	2.5	48	162	1.78	60	380	2010	5520	5490	3350	2320	230	130	90	100	213	0.12
11.0	2.8	43	159	1.75	50	350	1360	4540	4580	3010	1770	180	120	110	120	183	0.11
11.0	3.0	40	154	1.69	50	370	1570	4520	5570	4340	2790	230	120	90	110	206	0.12
11.0	4.0	30	143	1.57	60	350	1550	5080	5890	3770	2180	140	110	110	120	212	0.14
11.0	5.0	24	137	1.51	50	350	1660	5470	7230	4490	2530	120	120	110	180	256	0.17
11.0	6.0	20	128	1.41	40	330	1540	6170	7560	4590	2490	130	120	100	140	261	0.18
					Heat Flux Area (cm²)												
					19	15	14	11	8.0	9.2	8.3	13	26	45	90		
					Thermocouple												
					A	B	C	D	E	F	G	H	K	L	M		

ARC OPERATING CONDITIONS					LOCAL ANODE HEAT FLUX (q_a) W/cm²												
					CHAMBER			LIP				DOWNSTREAM FACE					
Current (J) kA	Mass Flow ($\dot{m}$) g/sec	$\frac{J^2}{\dot{m}}$ ($J^2/\dot{m}$) kA²-sec/g	Voltage (V) v	Power (P_T) MW	Thermocouple A Location (cm) -1.2	B -0.8	C -0.4	D 0.0	E 0.2	F 0.5	G 0.8	H 1.0	K 1.5	L 2.3	M 3.5	Anode Power (P_A) kW	Anode Power Fraction (P_A/P_T)
11.0	7.0	17	120	1.32	40	270	1420	6680	8830	7500	4020	250	90	70	70	290	0.22
11.0	7.5	16	119	1.30	40	270	1440	7460	9190	7440	4610	280	90	60	60	302	0.23
11.0	8.0	15	117	1.28	40	280	1360	6930	8570	7500	4470	270	90	60	60	299	0.23
11.0	9.0	13	108	1.19	30	250	1140	6550	7790	8000	4820	310	90	60	60	281	0.24
11.0	10.0	12	105	1.15	40	220	860	4620	6250	6510	4240	230	70	60	60	224	0.20
11.0	12.0	10	93	1.02	30	170	730	3480	4920	4280	3750	190	70	60	50	172	0.17
11.0	15.0	8	87	0.96	20	150	1030	8020	5990	4540	4800	570	80	50	50	250	0.26
11.0	16.0	8	65	0.72	20	120	540	2530	3680	3490	2810	160	60	50	40	132	0.18
11.0	18.0	7	64	0.70	30	100	600	2420	3430	2480	2500	160	60	50	50	119	0.17
11.0	24.0	5	63	0.69	20	110	600	2120	3030	2880	1860	140	50	50	50	109	0.16
11.0	32.0	4	63	0.69	20	360	1110	4190	3680	1860	2060	420	70	50	50	144	0.21
12.8	32.0	5	69	0.89	0	500	990	4450	4320	2200	2960	440	80	60	60	164	0.19
14.0	24.0	8	78	1.10	0	200	940	7170	6090	3700	4900	530	110	80	80	236	0.22
15.0	45.0	5	77	1.16	30	400	800	3310	3750	3300	2230	260	90	60	60	146	0.13
16.0	3.0	85	213	3.41	50	460	2010	5250	7440	5420	4180	580	220	170	210	284	0.08
16.0	6.0	43	188	3.00	90	570	2330	5280	6950	5800	3870	380	230	210	270	291	0.10
16.0	9.0	28	173	2.77	40	510	1900	7580	9000	7170	5150	330	230	180	200	336	0.12
16.0	10.0	26	170	2.73	50	510	1990	5880	8180	7700	4920	360	210	180	230	332	0.12
16.0	11.0	23	159	2.55	20	460	1850	9030	10800	9660	6020	330	210	180	240	400	0.16
16.0	12.0	21	150	2.40	30	460	1660	10400	15700	11000	8410	410	210	160	190	476	0.20
16.0	14.0	18	146	2.33	40	440	1600	11400	12900	14700	8960	440	180	150	180	502	0.22
16.0	16.0	16	133	2.13	40	360	1540	10700	12100	15300	8710	770	200	140	150	494	0.23
16.0	18.0	14	131	2.09	40	360	1300	8050	12100	11800	9050	870	190	120	140	426	0.20
16.0	20.0	13	125	2.00	40	320	1110	5430	7290	9170	9170	910	180	120	110	331	0.17
16.0	22.0	12	121	1.94	30	280	1040	5050	6460	7920	8150	860	140	90	100	294	0.15

Heat Flux Area (cm²)										
19	15	14	11	8.0	9.2	8.3	13	26	45	90
Thermocouple A	B	C	D	E	F	G	H	K	L	M

LOCAL ANODE HEAT FLUX

(q_a)

W/cm^2

ARC OPERATING CONDITIONS					CHAMBER			LIP					DOWNSTREAM FACE				
Cur-rent (J) kA	Mass Flow ($\dot{m}$) $\frac{g}{sec}$	$\frac{J^2}{\dot{m}}$ ($J^2/\dot{m}$) $\frac{kA^2\text{-sec}}{g}$	Volt-age (V) v	Power (P_T) MW	Thermocouple A	B	C	D	E	F	G	H	K	L	M	Anode Power (P_A) kW	Anode Power Fraction (P_A/P_T)
					Location (cm) -1.2	-0.8	-0.4	0.0	0.2	0.5	0.8	1.0	1.5	2.3	3.5		
16.0	24.0	11	82	1.30	30	270	1140	4000	6360	5960	5880	710	600	120	110	260	0.20
16.0	32.0	8	87	1.39	10	160	1260	2690	4460	4500	4200	470	130	90	90	184	0.13
16.0	45.0	6	78	1.25	0	400	1620	3130	2280	2880	1090	340	90	70	70	132	0.11
16.0	48.0	5	80	1.28	20	170	720	4030	4490	3850	4590	680	110	90	70	188	0.15
18.0	32.0	10	89	1.61	0	810	1890	4620	5900	7180	4870	740	170	140	120	274	0.17
19.0	36.0	10	132	2.51	20	810	2220	4070	5580	7660	4780	840	210	170	170	283	0.11
19.0	45.0	8	140	2.66	70	640	1160	6170	6710	8720	5210	610	180	140	140	303	0.11
21.0	45.0	10	154	3.23	90	1110	2200	8060	9900	12400	6790	850	240	180	180	429	0.13
22.0	6.0	81	249	5.48	70	840	2920	6600	9450	8530	5600	640	370	320	340	408	0.07
22.0	12.0	40	230	5.05	40	730	2910	7530	11900	10700	9350	1020	350	280	300	481	0.10
22.0	18.0	27	199	4.38	80	730	2900	6840	13000	13500	7630	380	360	350	420	509	0.12
22.0	20.0	24	198	4.36	180	790	3070	7870	12200	9980	4700	430	370	380	480	478	0.11
22.0	22.0	22	187	4.11	40	740	3040	9570	13300	9820	5070	430	400	400	460	489	0.12
22.0	24.0	20	179	3.93	70	740	3110	8960	14500	18100	7940	320	330	320	380	595	0.15
22.0	26.0	19	172	3.78	40	710	2680	9550	12200	14900	5360	460	400	370	430	511	0.14
22.0	28.0	17	169	3.73	40	680	2730	8690	12000	16900	6010	490	360	320	360	514	0.14
22.0	32.0	15	165	3.63	50	650	2700	6910	11800	16000	7040	450	360	290	290	482	0.13
22.0	36.0	13	164	3.61	60	710	2730	6710	10600	14400	10600	770	360	270	250	493	0.14
22.0	48.0	10	155	3.40	60	490	2620	4750	9900	9030	8670	890	310	230	220	384	0.11
31.0	24.0	40	293	9.08	130	1200	4880	14500	31400	18300	16400	1120	610	470	500	906	0.10
44.0	48.0	40	376	16.55	140	1900	8010	14500	25100	30700	20700	1340	1670	1360	1480	1258	0.08
					Heat Flux Area (cm^2) 19	15	14	11	8.0	9.2	8.3	13	26	45	90		
					Thermocouple A	B	C	D	E	F	G	H	K	L	M		

REFERENCES

1. Jahn, R. G., Physics of Electric Propulsion, McGraw-Hill Book Co., New York, 1968, p. 6.

2. Ibid., Chapter 1.

3. Sutton, G. W., Rocket Propulsion Elements, Third Ed., John Wiley and Sons, Inc., New York, 1963.

4. Jahn, R. G., op cit, Chapter 6.

5. Poeschel, R. L., King, R. J. and Schnelker, D. E., "An Engineering Model 30-cm Ion Thruster," AIAA Tenth Electric Propulsion Conference, Lake Tahoe, Nevada, Nov. 1, 1973, Paper No. 73-1084.

6. Stuhlinger, E., Ion Propulsion for Space Flight, McGraw-Hill Book Co., New York, 1964.

7. Jahn, R. G., op cit, Chapter 7.

8. John, R. R., Bennett, S. and Connors, J. F., "Arcjet Engine Performance: Experiment and Theory," AIAA J. Vol. 1, No. 11, November 1963, pp. 2517-2525.

9. Ducati, A. C., Giannini, G. M. and Muehlberger, E., "Recent Progress in High Specific Impulse Thermo-Ionic Acceleration," AIAA Second Aerospace Sciences Meeting, New York, January 25-27, 1965, Paper No. 65-96.

10. Cann, G. L. and Marlotte, G. L., "Hall Current Plasma Accelerator," AIAA J., Vol. 2, No. 7, July 1964, pp. 1234-1241.

11. Cann, G. L., Harder, R. L. and Nelson, S. T., "Experimental Performance of the Alpha Thrustor," AIAA Electric Propulsion and Plasmadynamics Conference, Colorado Springs, Colorado, Sept. 11-13, 1967, Paper No. 67-687.

12. Grossman Jr., W. and Hess, R. V., "Experiments with a Coaxial Hall Current Plasma Accelerator," AIAA J., Vol. 3, No. 6, June 1965, pp. 1034-1039.

13. Brockman, P., Hess, R., Bowen, F. and Jarrett, O., "Diagnostic Studies in a Hall Accelerator at Low Exhaust Pressure," AIAA Second Annual Meeting, San Francisco, California, July 26-29, 1965, Paper No. 65-297.

14. Hugel, H., "Self-Magnetic Effects in Arcjet Engines," AIAA J., Vol. 6, No. 8, August 1968, pp. 1573-1575.

15. Stratton, T. F., "High Current Steady State Coaxial Plasma Accelerators," AIAA J., Vol. 3, No. 10, October 1965, pp. 1961-1963.

16. Schneiderman, A. and Patrick, R. M., "Optimization of the Thermal Efficiency of the Magnetic Annual Arc," AIAA Third Aerospace Sciences Meeting, New York, January 24-26, 1966, Paper No. 66-115.

17. Ducati, A. C., Giannini, G. M. and Muehlberger, E., "Experimental Results in High-Specific-Impulse Thermo-Ionic Acceleration," AIAA J., Vol. 2, No. 8, August 1964, pp. 1452-1544.

18. Jahn, R. G. and Clark, K. E., "The Magnetoplasmadynamic Arcjet," Astronautica Acta, Vol. 13, 1967, pp. 315-325.

19. Nerheim, N. M. and Kelly, A. J., "A Critical Review of the Magnetoplasmadynamic (MPD) Thruster for Space Applications," Jet Propulsion Laboratory Report 32-1196, California Institute of Technology, Pasadena, California, February 18, 1968.

20. Cory, J. S., "Mass, Momentum and Energy Flow from an MPD Accelerator," Ph.D. Thesis, Aerospace and Mechanical Sciences Report No. 999, Princeton University, Princeton, New Jersey, 08540, Sept. 1971.

21. Jahn, R. G., op cit, Chapter 8.

22. Clark, K. E., "Quasi-Steady Plasma Acceleration," Ph.D. Thesis, Aerospace and Mechanical Sciences Report No. 859, Princeton University, Princeton, New Jersey 08540, May 1969.

23. Clark, K. E. and Jahn, R. G., "Quasi-Steady Plasma Acceleration," AIAA J., Vol. 8, No. 2, February 1970, pp. 216-220.

24. Bruckner, A. P., "Spectroscopic Studies of the Exhaust Plume of a Quasi-Steady MPD Accelerator," Ph.D. Thesis, Aerospace and Mechanical Sciences Report No. 1041, Princeton University, Princeton, New Jersey 08540, May 1972.

25. Boyle, M. J. and Jahn, R. G., "Effects of Insulator Ablation on the Operation of a Quasi-Steady MPD Arc," AIAA Tenth Electric Propulsion Conference, Lake Tahoe, Nevada, Nov. 1, 1973, Paper No. 73-1090.

26. Turchi, P. J. and Jahn, R. G., "Cathode Region of a Quasi-Steady MPD Arcjet," AIAA J., Vol. 9, No. 7, July 1971, pp. 1372-1379.

27. Oberth, R. C. and Jahn, R. G., "Anode Phenomena in High-Current Accelerators," AIAA J., Vol. 10, No. 1, January 1972, pp. 86-91.

28. Connolly, D. J., Sovie, R. J. and Seikel, G. R., "Performance and Diagnostics of a Water-Cooled Magnetoplasmadynamic Arc Thruster," NASA Technical Note, NASA TN D-5836, Lewis Research Center, Cleveland, Ohio, 44135, May, 1970.

29. Bennett, S., Enos, G., John, R. R. and Powers, W., "Magnetoplasmadynamic Thrustor Research," AVSSD-0272-67-RR (NASA CR-72345), Avco Missiles, Space and Electronics Group, Space Systems Division, Lowell Industrial Park, Lowell, Massachusetts 01852, May 21, 1967.

30. John, R. R., Bennett, S. and Connors, J. F., "Experimental Performance of a High Specific Impulse Arc Jet Enginer," AIAA Fourth Electric Propulsion Conference, Philadelphia, Penn., August 31 - Sept. 2, 1964, Paper No. 64-669.

31. Shih, K. E., et al, "Experimental Anode Heat-Transfer Studies in a Coaxial Arc Configuration," AIAA J., Vol. 6, No. 8, August 1968, pp. 1482-1487.

32. Hugel, H., "Flow Rate Limitations in the Self-Field Accelerator," AIAA Tenth Electric Propulsion Conference, Lake Tahoe, Nevada, November 1, 1973, Paper No. 73-1094.

33. Von Engel, A., and Steenbeck, M., Electrische Gasentladungen, Springer-Verlag, Berlin, 1932.

34. Bose, T. K., "Anode Heat Transfer for a Flowing Argon Plasma at Elevated Electron Temperature," J. Heat and Mass Transfer, Vol. 15, 1972, pp. 1745-1763.

35. Schoeck, P. A., Eckert, E. R. G. and Wutzke, S. A., "An Investigation of the Anode Losses in Argon Arcs and Their Reduction by Transpiration Cooling," University of Minneapolis, Minneapolis, Minnesota, ARL 62-341 (AD 278-570), April 1962.

36. Eckert, E. R. G. and Pfender, E., "Advances in Plasma Heat Transfer," in Advances in Heat Transfer, Vol. 2, Ed. Harnett, J. P. and Irvine, Jr., T. F., Academic Press, New York, 1967, pp. 229-316.

37. Bez, W. and Hocker, K.-H., "Theorie des Anodenfalls," Z fur Naturforschg, Vol. 9a, 1954, pp. 72-81.

38. Hocker, K.-H. and Bez, W., "Theorie des Anodenfalls II," Z fur Naturforschg, Vol. 10a, 1955, pp. 706-714.

39. Bez, W. and Hocker, K.-H., "Theorie des Anodenfalls," Z fur Naturforschg, Vol. 10a, 1955, pp. 714-717

40. Bez, W., Hocker, K.-H., "Theorie des Anodenfalls, IV. Der Anodenfall des Homogenkohle-Hochstrombogens in Luft," Z fur Naturforschg, Vol. 11a, 1956, pp. 118-123.

41. Bez, W. and Hocker, K.-H., "Theorie des Anodenfalls, V. Das Zischen des Homogenkohle-Hochstrombogens in Luft," Z fur Naturforschg, Vol. 11a, 1956, pp 192-196.

42. Jahn, R. G. et al, "Pulsed Electromagnetic Gas Acceleration," NASA NGL 31-001-005 Semi-annual Report for period 1 July 1970 to 31 December 1970, Aerospace and Mechanical Sciences Report No. 634p, January 1971, Princeton University, Princeton, N. J., pp. 64-69.

43. Jahn, R. G. et al, "Pulsed Electromagnetic Gas Acceleration," NASA NGL 31-001-005 Semi-annual Report for period 1 July 1971 to 31 December 1971, Aerospace and Mechanical Sciences Report No. 634r, January 1972, Princeton University, Princeton, N. J., pp. 97-102.

44. Di Capua, M. S., "Energy Deposition in Parellel-Plate Plasma Accelerators," Ph.D. Thesis, Aerospace and Mechanical Sciences Report No. 1015, December 1971, Princeton University, Princeton, N. J., Ch. 3.

45. Gardner, J. A., "Effects of a Dynamic Gas on Breakdown Potential," AIAA J., Vol. 8, No. 2, February 1970, pp. 1414-5.

46. Littauer, R., Pulse Electronics, McGraw-Hill, New York, 1965, pp. 53-56.

47. Leonard, S. L., "Basic Macroscopic Measurements," in Plasma Diagnostic Techniques Ed. R. H. Huddlestone and S. L. Leonard, Academic Press, New York, 1965, pp. 8-13.

48. Omega Engineering, Inc., The Omega Temperature Measurement Handbook, Springdale Station, Stamford, Conn., 1973, Sec. A and Sec. D.

49. Miller, I. and Freund, J. E., Probability and Statistics for Engineers, Prentice-Hall, Englewood Cliffs, N. J., (1965), pp. 117-123.

50. Clark, J. B., New Physical and Mathematical Tables, Oliver and Boyd, Edinburgh, 1969, p. 56.

51. Malliaris, A. C. et al, "Quasi-Steady MPD Propulsion at High Power," Final Technical Report AVSD-0146-71-RR, AVCO Corporation, Feb. 1971.

52. Jahn, R. G., et al., "Acceleration Patterns in Quasi-Steady MPD Arcs," AIAA J., Vol. 9, No. 1, Jan. 1971, pp. 167-172.

53. Vondra, R. J. et al., "Analysis of Solid Teflon Pulsed Plasma Thruster," J. Spacecraft and Rockets, Vol. 7, No. 12, Dec. 1970, p. 1402.

54. Guman, W. J. and Williams, T. E., "Pulsed Plasma Microthruster for Synchronous Meteorological Satellite (SMS)," AIAA 10th Electric Propulsion Conference, Lake Tahoe, Nev., Oct. 31, 1973, Paper No. 1066.

55. Bose, T. K., "Laminar Flow Heat Transfer from a Gaseous Plasma at Elevated Electron Temperature in the Presence of Electromagnetic Fields," Technical Report 32-1447, Jet Propulsion Laboratory, California Institute of Technology, Pasadena, California 91103, March 1, 1970, p. 3.

56. Lovberg, R. H., "Magnetic Probes," in Plasma Diagnostic Techniques, ed. Huddlestone, R. H. and Leonard, S. L., Academic Press, New York, 1965, pp. 69-112.

57. Jackson, J. D., Classical Electrodynamics, John Wiley and Sons, New York, 1962, pp. 137-139.

58. Jahn, R. G., *Physics of Electric Propulsion*, McGraw-Hill Book Co., 1968, pp. 74-79.

59. Oberth, R. C., "Anode Phenomena in High-Current Discharges," Ph.D. Thesis, Aerospace and Mechanical Sciences Report No. 961, Princeton University, Princeton, N. J. 08540, December 1970, Appendix.

60. Schott, L., "Electrical Probes," Chap. 11 in *Plasma Diagnostics*, W. Lochte-Holdgreven, Ed., North Holland, 1968.

61. Lam, S. H., "Unified Theory for the Langmuir Probe in a Collisionless Plasma," *Physics of Fluids*, Vol. 8, No. 1, January 1965, pp. 73-87.

62. Sutton, G. W. and Sherman, A., *Engineering Magnetohydrodynamics*, McGraw-Hill Book Co., New York, 1965, pp. 48-9.

63. Bohm, D., "Minimum Ionic Kinetic Energy for a Stable Sheath," Chapter 3 in *The Characteristics of Electrical Discharges in Magnetic Fields*, Ed. Guthrie, A. and Wakerling, R. K., McGraw-Hill Book Co., New York, 1949, pp. 77-86.

64. Lam, S.-H., personal communication.

65. Bruckner, A. P., op. cit., pp. 73-88.

66. Jahn, R. G., *Physics of Electric Propulsion*, op. cit., pp. 240-246

67. Cory, J. S., op. cit., pp. 54-59.

68. Bartz, D. R., "Survey of the Relationship Between Theory and Experiment for Convective Heat Transfer from Rocket Combustion Gases," Jet Propulsion Laboratory, California Institute of Technology, Pasadena, California, March 1, 1965.

69. Schlichting, H., *Boundary Layer Theory*, 4th Ed., McGraw-Hill Book Co., Toronto, Canada, 1960, Chapter 14.

70. Eckert, E. R. G. and Pfender, E., op. cit., p. 266.

71. Brahinsky, H. S. and Neel, C. A., "Tables of Equilibrium Thermodynamic Properties of Argon," Vol. I-IV, Arnold Engineering Development Center, AEDC-TR-69-19, March 1969.

72. Spitzer, Jr., L., Physics of Fully Ionized Gases, 2nd Edition, Interscience, New York, 1967, pp. 148-153.

73. Carslaw, H. S. and Jaeger, J. C., Conduction of Heat in Solids, 2nd Ed., Oxford, Clarendon Press, 1959, pp. 112-114.

74. Handbook of Chemistry and Physics, 52nd Ed., Chemical Rubber Co., Cleveland, Ohio, 44128, p. D-142.

75. Jahn, R. G. et al., "Pulsed Electromagnetic Gas Acceleration," NASA NGL 31-001-005, progress report for the period 1 January 1970 to 30 June 1970, Aerospace and Mechanical Sciences Report No. 634o, Princeton University, Princeton, N. J. 08540, July 1970, pp. 27-29.

76. Handbook of Chemistry and Physics, 52nd Ed., op. cit., pp. E69-70.

77. Fradkin, D. B., "Analysis of Acceleration Mechanisms and Performance of an Applied Field MPD Arcjet," Ph.D. Thesis, Aerospace and Mechanical Sciences Department, Princeton University, Princeton, N. J. 08540.

78. Lotz, W., "Electron-Impact Ionization Cross-Sections and Ionization Rate Coefficients for Atoms and Ions," The Astrophysical Journal, Supplement Series, Supplement Number 128, Vol. 14, May 1967, pp. 207-238.

79. Jahn, R. G., Physics of Electric Propulsion, op. cit., pp. 93-103.

80. Lam, S.-H., personal communication.

81. Ames, W. F., Numerical Methods for Partial Differential Equations, Barnes and Noble, Inc., New York, 1969, Chapter 2.

82. Vincenti, W. G. and Kruger, Jr., C. H., Introduction to Physical Gas Dynamics, John Wiley and Sons, New York, 1965, pp. 42-48.

83. Boyd, T. J. M., and Sanderson, J. J., Plasma Dynamics, Barnes and Noble, New York, 1969, p. 294.

84. Spitzer Jr., L., op. cit., pp. 127-131.

85. Kieffer, L. J. and Dunn, G. W., "Electron Impact Ionization Cross-Section Data for Atoms, Atomic Ions, and Diatomic Molecules: I. Experimental Data," Reviews of Modern Physics, Vol. 38, No. 1, January 1966, pp. 1-35.

86. Handbook of Lasers, Pressley, R. J. ed., Chemical Rubber Co., Cleveland, Ohio 44128, p. 263.

87. Imre, A. I., et al., "Cross-Sections for the Excitation of AII Laser Lines in Electron-Ion Collisions," Zh. Exp. and Tech. Phys., Vol. 15, No. 12, 20 June 1972, pp. 712-715.

88. Beigman, I. L., and Vainshtein, L. A., "Effective Excitation and Ionization Cross Sections of Ions," in Physics of Atomic Collisions, ed. D. V. Skobel'tsyn, Proceedings (Trudy) of P. N. Lebdev Physics Institute, Vol. 51, Translation by P. Robeson, Jr., Consultants Bureau, New York, 1971, p. 10.

89. Thomas, E. W., Excitation in Heavy Particle Collisions, Wiley-Interscience, New York, 1972, pp. 188-196.

90. Campbell, E. L., personal communication.

91. Petschek, H. and Byron, S., "Approach to Equilibrium Ionization behind Shock Waves in Argon," Annals of Physics, Vol. 1, 1957, pp. 270-315.

92. Aleksandrov, V. Ya., et al., "Exchange of Kinetic Energy in a Dense, Weakly Ionized Argon Plasma," Teplofizika Vysokikh Temperatur, Vol. 5, No. 5, Sept.-Oct. 1967, pp. 751-755.

93. Brown, I. G., Compher, A. B. and Kunkel, W. B., "Response of a Langmuir Probe in a Strong Magnetic Field," Physics of Fluids, Vol. 14, No. 7, July 1971, pp. 1377-1383.

94. Chen, F. F., "Electric Probes," in Plasma Diagnostic Techniques, Huddlestone, R. H. and Leonard, S. L., Eds., Academic Press, New York, 1965, pp. 113-200.

95. Kanal, M., "Theory of Current Collection of Moving Cylindrical Probes," J. Applied Physics, Vol. 35, No. 6, June 1964, pp. 1697-1703.

96. Jahn, R. G., *Physics of Electric Propulsion*, op. cit., pp. 50-55.

97. Moelwyn-Hughes, E. A., *Physical Chemistry*, 2nd Ed., Pergamon Press, 1965, Chapter 20.

98. Jahn, R. G. et al., "Pulsed Electromagnetic Gas Acceleration," NASA NGL 31-001-005, progress report for the period 1 January 1972 to 30 June 1972, Aerospace and Mechanical Sciences Report No. 634s, Princeton University, Princeton, N. J. 08540, July 1972, pp. 69-81.

99. Jahn, R. G. et al., "Pulsed Electromagnetic Gas Acceleration," NASA NGL 31-001-005, progress report for the period 1 July 1971 to 31 December 1971, Aerospace and Mechanical Sciences Report No. 634r, Princeton University, Princeton, N. J. 08540, Jan. 1972, pp. 52-63.

100. Shapiro, A. H., *The Dynamics and Thermodynamics of Compressible Fluid Flow*, Vol. 1, Ronald Press, New York, 1953, Ch. 4.